OPTICAL CHARACTERIZATION OF NI USING SPECTROSCOPIC ELLIPSOMETRY AT TEMPERATURES FROM 80 K TO 780 K

BY

FARZIN ABADIZAMAN, B.S., M.S.

A dissertation submitted to the Graduate School

in partial fulfillment of the requirements

for the degree

Doctor of Philosophy

Major Subject: Physics

New Mexico State University

Las Cruces, New Mexico

December 2020

Farzin Abadizaman

Candidate

Physics

Major

This dissertation is approved on behalf of the faculty of New Mexico State University, and it is acceptable in quality and form for publication:

Approved by the Dissertation Committee

Dr. Stefan Zollner

Chairperson

Dr. Michael Engelhardt

Committee Member

Dr. Heinz Nakotte

Committee Member

Dr. Jason Jackiewicz

Committee Member

DEDICATION

I dedicate this work to my beloved mother.

ACKNOWLEDGMENTS

I would like to express my deepest gratitude to my adviser Prof. Stefan Zollner for his continuous support throughout my work and studies at NMSU. I find myself indebted to the faculty members of the Department of Physics and would like thank all of them, in particular Prof. Michael Engelhardt, Prof. Igor Vasiliev, Prof. Heinrich Nakotte, and my committee member Prof. Jason Jackiewicz.

My graduate studies would not be possible without the endless support of my family. Therefore, I wish to express my appreciation and thank my brother and my wife for their ceaseless encouragement and support.

My sincere thanks to the Woollam company and its members, especially Gerry Cooney, Tom Tiwald, and James Hilfiker for their technical support and offline discussions. I am grateful to Prof. Schubert and his group for their collaboration. I would like to thank the Society of Vacuum Coaters (SVC) for awarding me a scholarship, which encouraged me to do my best in my studies. Many thanks to my colleagues Nuwanjula Samarasingha, Carola Emminger, Rigo Carrasco, and Galen Helms, as well as to the staff of the Physics Department, Rosa Urioste, Francisco Carreto-Parra, and Marisela Chavez.

VITA

2005-2009	B.S. in Physics, Shahrood University of Technology, Semnan, Iran
2009-2012	M.S. in Physics, Tehran University, Tehran, Iran
2015-2018	M.S. in Physics, New Mexico State University, NM, USA
2020	Ph.D. in Physics, New Mexico State University, NM, USA

Publications

- **F. Abadizaman** and S. Zollner, *Optical constants of single-crystalline Ni from 77 K to 770 K from ellipsometry measurements*, (In preparation for publication).
- **F. Abadizaman** and S. Zollner, *Optical constants of polycrystalline Ni from 0.06 to 6.0 eV at 300 K*, J. Vac. Sci. Technol. B **37**, 062920 (2019).
- C. Emminger, **F. Abadizaman**, N. S. Samarasingha, T. E. Tiwald, and S. Zollner *Temperature dependent dielectric function and direct bandgap of Ge*, J. Vac. Sci. Technol. B **38**, 012202 (2020)
- S. Zollner, P. Paradis, **F. Abadizaman**, and N. S. Samarasingha, *Drude and Kukharskii mobility of doped semiconductors extracted from Fourier-transform infrared ellipsometry spectra*, J. Vac. Sci. Technol. B **37**, 012904 (2019).

Presentations and posters

- **F. Abadizaman** and S. Zollner, *Temperature dependent optical properties of single-crystalline Ni (100)*, ELI Beamlines User Conference, Prague, Czech Republic, October 2020. (Talk)
- **F. Abadizaman**, C. Emminger, S. Knight, M. Schubert, and S. Zollner, *Optical Hall Effect in the Multi-valley Semiconductor Te-doped GaSb*, AVS 66$^{\text{th}}$ International Symposium & Exhibition, Columbus, Ohio, USA, October 2019. (Talk)
- **F. Abadizaman** and S. Zollner, *Optical constants of polycrystalline Ni from 0.06 to 6.0 eV at 300 K*, AVS 66$^{\text{th}}$ International Symposium & Exhibition, Columbus, Ohio, USA, October 2019. (Talk)
- **F. Abadizaman** and S. Zollner, *Temperature Dependence of Critical points of Ni 77-800 K*, AVS 65$^{\text{th}}$ International Symposium & Exhibition, Long Beach, California, USA, October 2018. (Talk)

- **F. Abadizaman** and S. Zollner, *Anomaly in optical constants of Ni near the Curie temperature*, NMAVS Symposium, Albuquerque, New Mexico, USA, May 2018. (Talk)
- **F. Abadizaman** and S. Zollner, *Temperature dependent Mueller matrix measurements of magnetized Ni near the Curie temperature*, APS March Meeting, Los Angeles, California, USA, March 2018. (Talk)
- **F. Abadizaman**, P. Paradis, and S. Zollner, *Temperature Dependent Mueller Matrix Measurements of Magnetized Ni near the Curie Temperature*, AVS 64$^{\text{th}}$ International Symposium & Exhibition, Tampa, Florida, USA, October 2017. (Talk)
- **F. Abadizaman** and S. Zollner, *Temperature Dependent Mueller Matrix Measurements of Magnetized Ni near the Curie Temperature*, NMAVS Symposium, Albuquerque, New Mexico, USA, May 2017. (Talk)
- R. A. Carrasco, C. Emminger, N. Samarasingha, **F. Abadizaman**, and S. Zollner, *Dielectric function and critical points of α-Sn and Ge*, AVS 65$^{\text{th}}$ International Symposium & Exhibition, Long Beach, California, USA, October 2018. (Talk)
- C. Emminger, R. Carrasco, N. Samarasingha, **F. Abadizaman**, and S. Zollner, *Temperature Dependent Dielectric Function and Critical Points of Bulk Ge compared to α-Sn on InSb*, 2018 IEEE Photonics Society Summer Topicals Meeting Series, Waikoloa, Hawaii, USA, July 2018. (Talk)
- **F. Abadizaman**, C. Emminger, S. Knight, M. Schubert, and S. Zollner, *Optical Hall Effect in Te-doped GaSb and undoped InAs*, 8$^{\text{th}}$ International Conference on Spectroscopy Ellipsometry, Barcelona, Spain, May 2019. (Poster)
- **F. Abadizaman** and S. Zollner, *Temperature Dependent Optical and Magneto-Optical Properties and Critical Points of Nickel*, 8$^{\text{th}}$ International Conference on Spectroscopy Ellipsometry, Barcelona, Spain, May 2019. (Poster)
- S. Zollner, P. Paradis, **F. Abadizaman**, and N. Samarasingha, *Factorized Broad-Band Description of the Dielectric Function Using a Modified Kukharskii Model*, 8th International Conference on Spectroscopy Ellipsometry, Barcelona, Spain, May 2019. (Poster)
- C. M. Zamarripa, N. Samarasingha, R. A. Carrasco, **F. Abadizaman**, and S. Zollner, *Temperature-dependent Ellipsometry and Thermal Stability of $Ge_2Sb_2Te_5$:C Phase Change Memory Alloys*, AVS 65$^{\text{th}}$ International Symposium & Exhibition, Long Beach, California, USA, October 2018. (Poster)
- **F. Abadizaman** and S. Zollner, *Mueller Matrix anomaly near the Curie temperature of Ni*, 10$^{\text{th}}$ Workshop Ellipsometry, Chemnitz, Germany, March 2018. (Poster)
- **F. Abadizaman**, J. M. Moya, and S. Zollner, *Experimental Errors in Mueller Matrix Elements of Isotropic Samples*, APS Four Corners Section Meeting, Las Cruces, New Mexico, USA, October 2016. (Poster)

ABSTRACT

OPTICAL CHARACTERIZATION OF NI USING SPECTROSCOPIC ELLIPSOMETRY AT TEMPERATURES FROM 80 K TO 780 K

BY

FARZIN ABADIZAMAN, B.S., M.S.

Doctor of Philosophy

New Mexico State University

Las Cruces, New Mexico, 2020

Dr. Stefan Zollner, Chair

In this work we present the optical properties of poly-crystalline and single-crystalline Ni at various temperatures from 80 K to 780 K. The measurements were taken using an FTIR-VASE ellipsometer from 1.5 μm to 40 μm and a VASE ellipsometer from 190 nm to 2.5 μm at angles of incidence of 65° to 75° in air and 70° in a UHV cryostat. For measurements in the cryostat, all samples were heat treated in UHV at 770 K for at least six hours. The optical constants of Ni are modeled using four Lorentzian oscillators representing the interband transitions and two Drude oscillators representing s- and d-electron conduction bands. The DC conductivity of Ni is extracted from the Drude parameters and compared with electrical measurements and a good agreement is observed. Two main absorption peaks near 1.5 eV and 4.8 eV in the optical conductivity of Ni are seen. The temperature dependence of the

main absorption peak at 4.8 eV shows that this interband transition is affected by scattering with phonons or magnons with an effective energy of 77 meV. We interpret the reduction of the broadening of this peak as the ferromagnetic exchange energy, which is in good agreement with literature. The energy and the broadening of the absorption peak near 1.5 eV are found to be constant over the temperature range. Its amplitude decreases with temperature up to the Curie temperature (T_c = 627 K) and stays constant above this temperature. This behavior is explained by assigning the peak to $L_{3\downarrow} \rightarrow L_{3\downarrow}$ transitions.

CONTENTS

LIST OF TABLES

LIST OF FIGURES

1 INTRODUCTION

Nickel is a transition metal with the atomic number 28 belonging to the group XI of the periodic table. It is one of the only four transition metals that is ferromagnetic at around room temperature along with Fe, Co and Gd. The transition from the ferromagnetic to the paramagnetic phase of Ni, Fe, Co, and Gd occurs at the Curie temperatures (T_c) of 627 K, 1043 K, 1400 K, and 292 K, respectively [1]. The Debye temperature of Ni θ_D = 345 K at T = 293 K and θ_D = 477 K at T = 0 K [2, 3]. Nickel has an FCC crystal structure with a lattice constant of 3.499 Å and the symmetry group of Fm$\bar{3}$m in the ferromagnetic phase and R$\bar{3}$m' in the paramagnetic phase with the preferred moment direction of ferromagnetic single crystalline Ni along the [111] direction [4]. The electronic configuration of Ni has been a subject of debate as two electronic configurations have been suggested. The configuration [Ag]$3d^9 4s^1$ has been theoretically reported to have a lower ground state energy than [Ag]$3d^8 4s^2$ [5]. In reality, experiments show that the electronic configuration of Ni is [Ag]$3d^{9.4} 4s^{0.6}$ which means that the 3d up state is full with five electrons. There are 4.4 electrons (0.6 hole) in the 3d down state and 0.6 electrons in the 4s state [6]. This makes optical transitions from 4s to 3d possible due to the cubic crystal field. Electrons can also scatter between s and d bands under assistance of phonons and magnons.

Owing to its ferromagnetic properties, Ni has been the subject of numerous electrical and optical studies [5, 7]. In complementary metal-oxide semiconductor (CMOS) transistors, metal silicides like Ni, Co, Ti, etc. are used to form low resistance contacts to source, drain and gate regions [8, 9]. NiSi is in particular important due to its narrow line sheet resistance and ease of fabrication. Ni is also coated as a thin film on patterned CMOS devices to form

monosilicide in the source, drain and gate areas [9]. Therefore, studying optical properties of Ni is crucial as the optical properties are used to find the thickness of the coated thin films, especially in the optical metrology of transistors. Due to the importance of the optical properties of Ni in the semiconductor industry, in this work we performed ellipsometry measurements to find and model the dielectric constants of Ni at various temperatures and in a wide energy range that allows us to characterize the free carriers, optical conductivity, and interband transitions of Ni.

2 THEORY

This chapter is dedicated to the theoretical background of ellsipometry, polarization of light, and optical properties of materials. The following topics are visited subsequently. We will start with the mathematical description of propagation and polarization of light. We then explain the optical elements and their representative Jones matrices and finally the interaction of light and matter is studied in the framework of the optical properties of crystals.

2.1 Propagation and Polarization of Light

The magnitude of the electric field of an electromagnetic beam traveling in the z-direction with an angular frequency of $\omega = 2\pi f$ and a wave vector of $\vec{K} = K\hat{z}$ can be written as a one dimensional generalized plane wave [10]

$$\begin{aligned} E &= E_0 \exp[i(\vec{K} \cdot \vec{r} - \omega t + \delta)] \\ &= E_0 \exp[i(Kz - \omega t + \delta)], \end{aligned} \tag{1}$$

with

$$K = \frac{\omega n}{c} = \frac{2\pi n}{\lambda}, \tag{2}$$

where E_0 is the maximum amplitude of the electric field, n is the refractive index of the medium, λ is the wavelength of the light and c is the speed of light in vacuum. If the medium is absorptive, i.e. the medium absorbs the energy of light, then the refractive index may be written as a complex number $n + ik$, where k is the extinction coefficient (not to be confused with the wave vector $\vec{K}$ and its magnitude K). Then the electric field of an electromagnetic wave is written as

$$E = E_0 \exp\left(-\frac{2\pi k}{\lambda} z\right) \exp[i(Kz - \omega t + \delta)], \tag{3}$$

which shows that in an absorptive medium, the magnitude of the electric field decreases exponentially with distance.

The intensity of light is defined as

$$I = |E|^2 = EE^*. \tag{4}$$

Using this definition, Eq. (3) becomes

$$I = |E_0|^2 \exp\left(-\frac{4\pi k}{\lambda} z\right). \tag{5}$$

Rewriting this equation yields Beer's law

$$I = I_0 \exp(-\alpha z), \tag{6}$$

where $\alpha = 4\pi k/\lambda$ is called absorption coefficient and defines the penetration depth $\delta_p = 1/\alpha = \lambda/4\pi k$, over which the intensity of the incident beam decreases by a factor of $1/e$ (i.e. $I = 37\% I_0$).

Polarization of light refers to the time dependence of the direction of the electric field of light. The electric field of linearly polarized light does not change its direction over time and it only oscillates in magnitude. Other types of polarizations depend on the phase difference between the perpendicular components of the electric field. In optics, the electric field of light is decomposed into a component parallel to the plane of incidence (p-component) and a component perpendicular to the plane of incidence (s-component). Therefore, a beam of light propagating in the z-direction may be written as

$$\begin{aligned} \mathbf{E(z,t)} &= E_p(z,t)\hat{p} + E_s(z,t)\hat{s} \\ &= E_{p0}\exp[i(Kz - \omega t + \delta_p)]\hat{p} + E_{s0}\exp[i(Kz - \omega t + \delta_s)]\hat{s} \end{aligned} \tag{7}$$

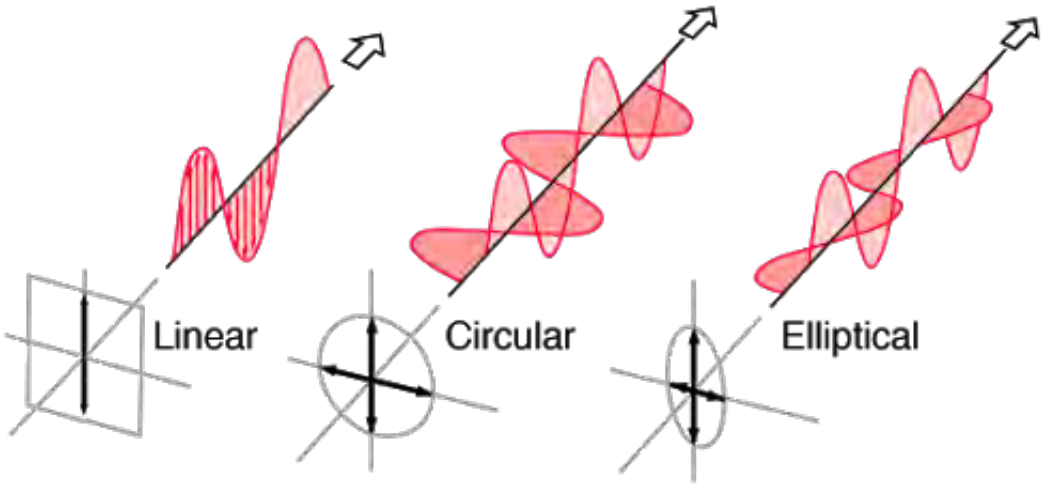

Figure 2.1: Different polarization states of light. (Retrieved from http://hyperphysics.phy-astr.gsu.edu/hbase/phyopt/polclas.html on October 9, 2020. Copyright Rod Nave, Georgia State University, reprinted with permission.)

Here, we assume that the media is isotropic, otherwise the wave vector depends on the directions of propagation. Using Eq. (7) one can define a linearly polarized light as the case where $\delta_s - \delta_p = 0$ and circularly polarized light as $\delta_s - \delta_p = \pi/2$. Other values of $\delta_s - \delta_p$ define elliptically polarized light. Different polarization states of light are illustrated in Fig. 2.1.

2.1.1 Jones Formalism

An elegant and convenient way of mathematical representation of light was proposed by R. C. Jones [11]. In this method, the electric field of light is described by a 2×1 matrix (Jones vector) and optical elements are described by 2×2 matrices (Jones matrices)

$$\mathbf{E}(z,t) = \begin{bmatrix} E_p \\ E_s \end{bmatrix}, \tag{8}$$

where

$$E_p = E_{p0} e^{i\delta_p}$$
$$E_s = E_{s0} e^{i\delta_s}. \tag{9}$$

In this form, the time dependence of the components of the electric field is omitted. Therefore, one can write the linear and circularly polarized light as follows

$$\mathbf{E}_{linear,p} = \begin{bmatrix} 1 \\ 0 \end{bmatrix}, \mathbf{E}_{linear,s} = \begin{bmatrix} 0 \\ 1 \end{bmatrix}, \tag{10}$$

and

$$\mathbf{E}_{linear,45} = \frac{1}{\sqrt{2}} \begin{bmatrix} 1 \\ 1 \end{bmatrix}, \mathbf{E}_R = \frac{1}{\sqrt{2}} \begin{bmatrix} 1 \\ i \end{bmatrix}, \mathbf{E}_L = \frac{1}{\sqrt{2}} \begin{bmatrix} 1 \\ -i \end{bmatrix}. \tag{11}$$

The intensity of light in each direction will be equal to the square of the magnitude of the element. One can write a general Jones vector for elliptically polarized light as follows [12,13]

$$\mathbf{E}_{elliptical} = \begin{bmatrix} \sin\psi \exp(i\Delta) \\ \cos\Delta \end{bmatrix}, \tag{12}$$

where ψ is defined in Fig. 2.2 and $\Delta = \delta_p - \delta_s$. These angles are called ellipsometric angles.

2.1.2 Depolarization

Depolarization is a phenomenon in which polarized light becomes unpolarized or partially polarized upon reflection by or transmission through a sample or/and optical element. A depolarizer is used in ellipsometry to remove the source polarization and it is made of a birefringent crystal [14]. An important point is that non-polarized light cannot be described by Jones vectors. Non-polarized light is studied utilizing Mueller Matrix (MM) formalism [12], which is not discussed in this dissertation. As long as the sample is concerned, depolarization

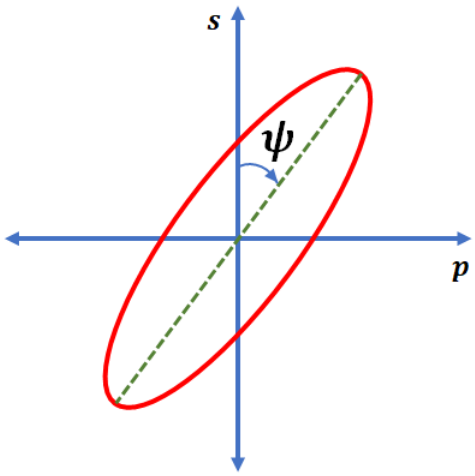

Figure 2.2: Definition of the ellipsometric angle ψ.

effects of the sample causes errors in ellipsometry measurements. There are different sources of depolarization in ellipsometry such as non-uniform thickness, large surface roughness, finite band width of the monochromator, angular spread, backside reflections, and patterning. Backside reflection occurs for transparent substrates ($k \sim 0$) where light can reach the back side of the sample and get reflected by the back side. This kind of depolarization can be greatly reduced by roughening the back side of the sample. This can be done by sand blasting or putting a scotch tape on the back side of the sample. Moderate depolarization effects can be taken into account to some extent when modeling the optical constants of the sample.

2.2 Optical Elements

Any element that is in the path of the light beam is called an optical element and is required to be represented by a Jones' matrix. Optical elements can either change the state of the polarization of light or the direction of propagation. In this section different optical elements

that are used in ellipsometry are studied.

2.2.1 Polarizer

A polarizer is an optical element that is utilized to change an arbitrary polarization state of light to linear polarization. It is made out of birefringent materials like calcite or MgF_2 [14]. A polarizer with a polarization axis positioned at an angle of θ counterclockwise with respect to the plane of incidence is represented as [12, 15]:

$$P(\theta) = \begin{bmatrix} \cos^2\theta & \sin\theta\cos\theta \\ \sin\theta\cos\theta & \sin^2\theta \end{bmatrix}. \tag{13}$$

Equation (13) can be derived by rotating a linear polarizer along the p-axis with a counter-clockwise rotation of an angle θ as follows:

$$\begin{bmatrix} \cos^2\theta & \sin\theta\cos\theta \\ \sin\theta\cos\theta & \sin^2\theta \end{bmatrix} = \begin{bmatrix} \cos\theta & -\sin\theta \\ \sin\theta & \cos\theta \end{bmatrix} \begin{bmatrix} 1 & 0 \\ 0 & 0 \end{bmatrix} \begin{bmatrix} \cos\theta & \sin\theta \\ -\sin\theta & \cos\theta \end{bmatrix}. \tag{14}$$

A clockwise rotation would give the same result with a minus sign in the off-diagonal elements.

2.2.2 Retarder

A retarder is an optical element made of a birefringent material that is used to change the polarization state of light from linearly polarized to elliptically polarized or vice versa. Common examples of retarders are a half-wave plate and a quarter-wave plate. A half-wave plate polarization rotator changes horizontal linearly polarized light to vertical linearly polarized light, or linearly polarized light at 45° to linearly polarized light at 135°. A quarter-wave plate is used to change linearly polarized light to circularly polarized light or vice versa. A retarder works based on the fact that the refractive indexes along the ordinary

and extraordinary axis of the material are different. Therefore, the components of light that travel along the ordinary and extraordinary directions will have different speed inside the material. Hence, there will be a phase difference δ between the two components of light. This phase difference depends on the difference of the refractive indexes, wavelength of light, and the thickness of the retarder

$$\delta = \frac{2\pi|n_o - n_e|L}{\lambda_0}. \tag{15}$$

By changing the thickness of the retarder, one can make the desired wave-plate. For example $\delta = \pi$ for a half-wave plate and $\delta = \pi/2$ for a quarter wave plate. The Jones matrix of a retarder with the retardance of δ and the fast axis along the p-axis is given as [14]

$$R = \begin{bmatrix} 1 & 0 \\ 0 & e^{-i\delta} \end{bmatrix}. \tag{16}$$

Counterclockwise rotation of R through an angle θ yields the general Jones matrix of a retarder with the retardance of δ and a fast axis that makes an angle of θ counterclockwise with the p-axis

$$R(\delta, \theta) = \begin{bmatrix} \cos\theta & -\sin\theta \\ \sin\theta & \cos\theta \end{bmatrix} \begin{bmatrix} 1 & 0 \\ 0 & e^{-i\delta} \end{bmatrix} \begin{bmatrix} \cos\theta & \sin\theta \\ -\sin\theta & \cos\theta \end{bmatrix}, \tag{17}$$

which becomes

$$R(\delta, \theta) = \begin{bmatrix} \cos^2\theta + e^{-i\delta}\sin^2\theta & \sin\theta\cos\theta - e^{-i\delta}\sin\theta\cos\theta \\ \sin\theta\cos\theta - e^{-i\delta}\sin\theta\cos\theta & e^{-i\delta}\cos^2\theta + \sin^2\theta \end{bmatrix}. \tag{18}$$

A clockwise rotation of Eq. (16) can be found by substituting (θ) with $(-\theta)$.

Using Eq. (18), the Jones matrix of a quarter-wave plate with a horizontal fast axis is

$$R_{qwp} = R(\pi/2, 0) = \begin{bmatrix} 1 & 0 \\ 0 & -i \end{bmatrix}, \tag{19}$$

and a half-wave plate with a fast axis along the horizontal is represented by

$$R_{hwp} = R(\pi, 0) = \begin{bmatrix} 1 & 0 \\ 0 & -1 \end{bmatrix}. \tag{20}$$

Contemporary materials that are used to make retarders are quartz, MgF_2, mica, and polymer. However, MgF_2 is more common because of its transparency over a wide wavelength range [14].

2.2.3 Windows

Viewports in ellipsometry are the entrance and exit windows of the cryostat. The viewports of the VASE (near-infrared to near-UV spectral range) are made out of fused silica and the viewports of the FTIR-VASE (mid-infrared spectral range) are made out of Zinc Selenide (ZnSe). Neither of the materials is birefringent but they show a small birefringence under the strain caused by the flanges used to secure the windows on the cryostat. This birefringence alters the polarization state of the incident and exit light. Therefore, the viewports are treated as retarders with a small retardance and the ellipsometry data has to be corrected for the window effects. Due to their importance in fabrication of thin films, the window effects have been extensively studie [12,16–38]. Generally, there are two methods for window effects corrections. First, finding the optical parameters of each window and applying them to the measured data. Second, introducing a term that contains a combined effect of both windows and applying that term to the measured data. The first method would be the ideal method but it usually requires the removal of the viewports, unless the sample is isotropic and the ellipsometer can measure all 16 Mueller Matrix (MM) elements [35,37]. The second method is used as a built-in program in WVASE and can effectively correct the windows effects [13].

However, it works only for regular ellipsometry measurements (ψ and Δ measurements), not for MM measurements, and it also does not provide information about the birefringence of each window.

The retardance of the windows is usually assumed to be very small ($\delta < 1$) and contrary to the ideal retarders, it demonstrates a dispersion relation. The built-in program in WVASE can correct for the window effects by assuming that the windows affect the s- and p-components (referred to as out-of-plane and in-plane, respectively) of the incident and exit beam differently. This approach does not define a specific azimuth angle for the fast axis of the retardation of the windows. It assumes that the azimuth angle of both windows' retardation is 45° for the s-component of the light and 0° for the p-component. It also assumes that both in-plane and out-of-plane retardances has the same dispersion formula

$$\delta(\lambda) = \frac{a_1}{\lambda}\left(1 + \frac{a_2}{\lambda^2} + \frac{a_3}{\lambda^4}\right). \tag{21}$$

As the polarizer in the FTIR-VASE is fixed at 45°, the out-of-plane component of the incident beam does not experience any retardation, but the exit beam does. Therefore, only the out-of-plane retardation of the exit window needs to be determined and the entrance window is left at 0°. Furthermore, both entrance and exit windows have a common dispersion equation as in Eq. (21) with common a_2 and a_3 parameters. The in-plane retardation is simply added to the ellipsometric angle Δ of the sample as a Delta offset with the dispersion relation of Eq. (21). As the viewports of the VASE and FTIR-VASE are made of different materials, there is always a mismatch when merging the data taken from both instruments inside the cryostats. This mismatch affects the modeled optical constant. Therefore, to obtain the best model for the optical constants of the sample, one needs to eliminate the

mismatch. The merging procedure and more about the windows is discussed in appendix A.

2.3 Interaction of Light with Matter

When light travels from one medium to another, some part of it gets reflected at the interface and the rest goes through the other medium. Reflection at the interface and the propagation of light through the medium are governed by the complex refractive index of the medium $\tilde{n} = n + ik$, where n is the refractive index and k is the extinction coefficient. When the incident angle with respect to the normal of the interface plane is zero, the reflection at the interface and the transmission are given by [12]

$$R = \frac{(n_1 - n_0)^2 + (k_1 - k_0)^2}{(n_1 + n_0)^2 + (k_1 + k_0)^2}, \tag{22}$$

$$T = (1 - R)^2 e^{-\alpha d}, \tag{23}$$

where d is the thickness of the sample. If the first medium is air ($\tilde{n}_0 = 1$), R becomes the familiar formula [39]

$$R = \left|\frac{\tilde{n} - 1}{\tilde{n} + 1}\right|^2 = \frac{(n-1)^2 + k^2}{(n+1)^2 + k^2}. \tag{24}$$

The part of light that goes through the medium loses its intensity according to the Beer's law expressed in Eq.(6). As light travels through the medium, its velocity is reduced as

$$v = \frac{c}{n}, \tag{25}$$

where c is the speed of light in vacuum and v is the speed of light in the new medium. The refractive index also defines the change in the direction of propagation upon entering the new medium through Snell's law. In almost all media, the refractive index depends on

the wavelength of light. This phenomenon is called dispersion and the medium is called dispersive. Examples of such media are glass and water.

When light travels from a medium of refractive index $\tilde{n}_0$ to a medium of a refractvie index $\tilde{n}_1$, the reflectivity and transmission depend on the angle of incidence and the refractive indexes which are given by Fresnel coefficients [10]

$$r_{pp} = \frac{\tilde{n}_0 \cos\theta_1 - \tilde{n}_1 \cos\theta_0}{\tilde{n}_0 \cos\theta_1 + \tilde{n}_1 \cos\theta_0}, \quad r_{ss} = \frac{\tilde{n}_0 \cos\theta_0 - \tilde{n}_1 \cos\theta_1}{\tilde{n}_0 \cos\theta_0 + \tilde{n}_1 \cos\theta_1}, \tag{26}$$

$$t_{pp} = \frac{2\tilde{n}_0 \cos\theta_0}{\tilde{n}_1 \cos\theta_0 + \tilde{n}_0 \cos\theta_1}, \quad t_{ss} = \frac{2\tilde{n}_0 \cos\theta_0}{\tilde{n}_0 \cos\theta_0 + \tilde{n}_0 1 cos\theta_1}, \tag{27}$$

where θ_0 and θ_1 are the angles of incidence and the angle of refraction, which are related to each other through Snell's law

$$\tilde{n}_0 \sin\theta_0 = \tilde{n}_1 \sin\theta_1. \tag{28}$$

The reflectivity R and reflection coefficient r are related to each other through the following equation

$$R = |r|^2, \tag{29}$$

and the same relation holds for transmission. One should note that the reflectivity R is a real number between 0 and 1, but the reflection coefficient is a complex number. The Jones matrix for the reflection of the sample is defined as [12]

$$J = \begin{bmatrix} r_{pp} & r_{ps} \\ r_{sp} & r_{ss} \end{bmatrix} = \begin{bmatrix} \vec{E}_p^o/\vec{E}_p^i & \vec{E}_s^o/\vec{E}_p^i \\ \vec{E}_p^o/\vec{E}_s^i & \vec{E}_s^o/\vec{E}_s^i \end{bmatrix}, \tag{30}$$

where i stands for "incident" and o stands for "outgoing". $R_{ps} = |r_{ps}|^2$ is the probability of cross polarization of s-polarized light coming in and p-polarized light going out. The off-diagonal elements are zero for isotropic surfaces and non-zero for anisotropic ones. In the case of anisotropic samples, the Fresnel coefficients cannot be written for the cross-polarization

effects (r_{sp} and r_{ps}) because s- and p-components are not eigen-states of reflection [12] and one has to use the 4×4 formalism to treat the anisotropic Jones or Mueller matrices. Chapter 9 of Ref. 12 explains this formalism in great detail.

Ellipsometry measures the ratio of the p- and s-reflection coefficients. Therefore, the Jones matrix of the sample that is measured in ellipsometry is given as [14]

$$J = r_{ss} \begin{bmatrix} r_{pp}/r_{ss} & r_{ps}/r_{ss} \\ r_{sp}/r_{ss} & 1 \end{bmatrix} = r_{ss} \begin{bmatrix} \rho & \rho_{ps} \\ \rho_{ss} & 1 \end{bmatrix} = \begin{bmatrix} \tan\psi e^{i\Delta} & \tan\psi_{ps} e^{i\Delta_{ps}} \\ \tan\psi_{sp} e^{i\Delta_{sp}} & 1 \end{bmatrix}. \tag{31}$$

The relation between measured ellipsometric angles ψ and Δ, and the refractive index of the sample is not generally a simple equation. However, if the medium 1 is air with the refractive index of $n = 1$ and the medium 2 is an infinite isotropic medium with a refractive index of $n = \sqrt{\epsilon}$, where ϵ is the dielectric constant of the medium, then one can write [12]

$$\epsilon = \epsilon_1 + i\epsilon_2 = \sin^2\theta \left(1 + \left[\frac{1-\rho}{1+\rho} \right]^2 \tan^2\theta \right), \tag{32}$$

where θ is the incident angle. One can also use this equation to extract the dielectric constant of a sample consisting of different layers. In that case, ϵ is called the pseudo-dielectric function shown as $< \epsilon >$, which assumes the entire sample as one sample with an infinite length. The pseudo-dielectric function does not consider an overlayer (surface roughness or oxide layer).

2.3.1 Absorption Edge

As was mentioned earlier, the amount of light that gets reflected and/or goes through the medium (sample) is governed by the refractive index of the medium. This section explores the physical meaning of the refractive index and its relation to the atomic and crystal structure of the sample.

In general, the refractive index is related to the dielectric function of an isotropic material as follows

$$\epsilon = n^2, \tag{33}$$

where

$$\epsilon = \epsilon_1 + i\epsilon_2 \quad \text{and} \quad n = n + ik. \tag{34}$$

Therefore

$$\epsilon_1 = n^2 - k^2 \quad \text{and} \quad \epsilon_2 = 2nk. \tag{35}$$

The inverse relations are also useful to find n and k from ϵ

$$n = \sqrt{\frac{|\epsilon| + \epsilon_1}{2}}, \quad k = \sqrt{\frac{|\epsilon| - \epsilon_1}{2}}, \tag{36}$$

where $|\epsilon| = \sqrt{\epsilon_1^2 + \epsilon_2^2}$.

If the material is anisotropic, then the refractive index and dielectric function depend on the direction of propagation of light

$$\begin{bmatrix} \epsilon_{xx} & \epsilon_{xy} & \epsilon_{xz} \\ \epsilon_{yx} & \epsilon_{yy} & \epsilon_{yz} \\ \epsilon_{zx} & \epsilon_{zy} & \epsilon_{zz} \end{bmatrix} = \begin{bmatrix} n_{xx}^2 & n_{xy}^2 & n_{xz}^2 \\ n_{yx}^2 & n_{yy}^2 & n_{yz}^2 \\ n_{zx}^2 & n_{zy}^2 & n_{zz}^2 \end{bmatrix}. \tag{37}$$

In this case, the material is called birefringent and can be uniaxial or biaxial, meaning it has one or two optical axes, respectively. Isotropic materials can also become birefringent upon applying an external magnetic field [40].

When light is irradiated on a material and the frequency of light is increased from zero to higher values, lights gets absorbed at specific frequencies. Optical characterization of materials is the study of these characteristic frequencies. As the frequency of light increases, absorption is caused by free carriers, lattice absorption, and interband electronic absorption. The onset of interband electronic absorption is called the absorption edge and defines the

band gap of the crystal. The free carrier and interband absorption can occur in IR or UV region, while lattice absorption happens in the IR region. All absorption frequencies can be recognized in the reflectivity or transmission spectra of the material through Eq. (24). Since ellipsometry measures the reflection coefficient, which is a function of the refraction index, one needs to model the experimental data in terms of the refraction index. This in turn becomes a task of studying and modeling the dielectric constant of the material because the refractive index and the dielectric constant are related to each other through Eq. (33). Therefore, in the following sections we will study the dielectric function due to different absorption mechanisms.

2.3.2 Free Carrier Absorption

The free carrier absorption is the response of the free electrons or holes to the incident electromagnetic beam. This type of absorption occurs for materials that contain free electrons or holes, such as metals or doped semiconductors. The equation of motion of a free electron with an effective mass m^*, a damping coefficient γ, and an electric charge e is

$$m^* \frac{d^2x}{dt^2} + m^* \gamma \frac{dx}{dt} = -eE(t), \tag{38}$$

where E is the electric field of the incident beam.

Assuming the electric field of $E(t) = E\Re e^{-i\omega t}$, Eq. (38) has the solution

$$x(t) = x_0 \Re(e^{-i\omega t}), \tag{39}$$

where

$$x_0 = \frac{eE/m^*}{\omega^2 + i\omega} \tag{40}$$

and $\Re$ means the real part. The factor γ is called the scattering rate and $\tau = 1/\gamma$ is the scattering time. As the displacement of the electron results in a dipole moment $\vec{p}$ with the magnitude of $-e\vec{x}_0$, one can define the polarization $\vec{P}$ as the sum of the polarization of all electrons per unit volume

$$\begin{aligned} \vec{P} &= n\vec{p} = -ne\vec{x_0} \\ &= -\frac{ne^2}{m^*}\frac{1}{\omega^2 + i\gamma\omega}\vec{E}, \end{aligned} \tag{41}$$

where n is the number of electrons per unit volume. Equation (41) shows that the resultant dipole moment is in the opposite direction of the electric field, regardless of the sign of the charge. One can define the polarization of the holes by simply changing the sign of the electric charge and using the effective mass of the hole. The susceptibility of the free carriers is then defined as $\chi = P/\epsilon_0 E$ and the dielectric constant is [10]

$$\epsilon(\omega) = 1 + \chi = 1 - \frac{\omega_p^2}{\omega^2 + i\gamma\omega}, \tag{42}$$

where

$$\omega_p^2 = \frac{ne^2}{\epsilon_0 m^*} \tag{43}$$

is called the plasma frequency. In ellipsometry Eq. (42) is called the Drude term and is used to model the behavior of the free electrons in metals or doped semiconductors. Equation (42) is usually written in the following form in ellipsometry modelings in terms of energy

$$\epsilon(E) = 1 - \frac{A}{E^2 + i\Gamma E}, \tag{44}$$

where

$$E = \hbar\omega, \quad \Gamma = \hbar\gamma, \quad A = \hbar^2\omega_p^2 = \frac{\hbar^2 ne^2}{\epsilon_0 m^*}. \tag{45}$$

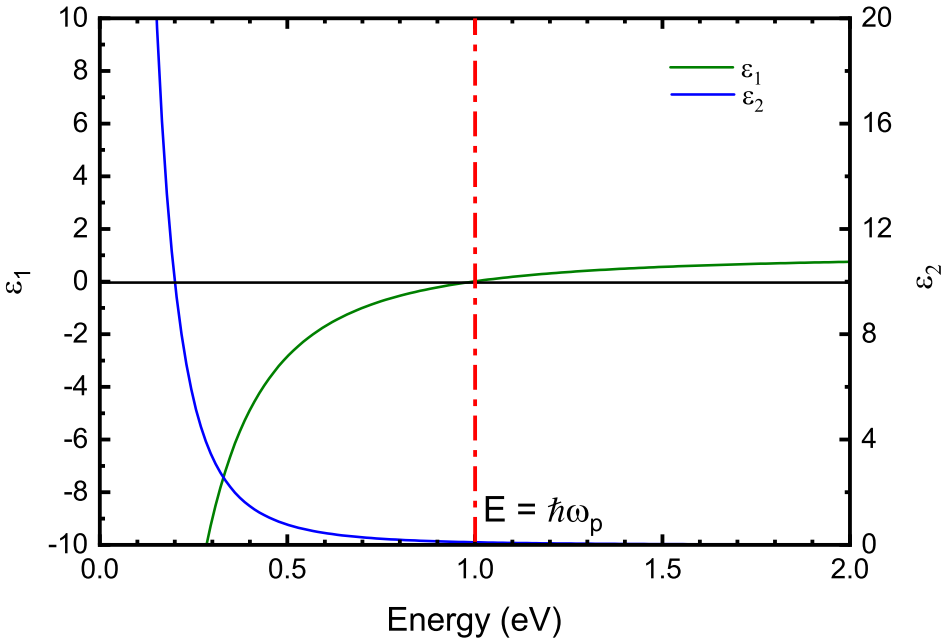

Figure 2.3: Real and imaginary part of the dielectric constant for a Drude term simulated for $\hbar\omega_p = 1$ eV and $\hbar\gamma = 0.1$ eV. The real part of the dielectric function changes from negative to positive at $\omega = \sqrt{\omega_p^2 - \gamma^2}$, which is $\approx \omega_p$ for very small scattering rates.

Equation (42) can be written in terms of its real and imaginary part as $\epsilon = \epsilon_1 + i\epsilon_2$, where

$$\begin{aligned} \epsilon_1 &= 1 - \frac{\omega_p^2}{\omega^2 + \gamma^2} \\ \epsilon_2 &= \frac{\omega_p^2 \gamma}{\omega(\omega^2 + \gamma^2)}. \end{aligned} \tag{46}$$

The dielectric function of a Drude term in Eq. (46) is demonstrated in Fig. 2.3 for $\hbar\omega_p = 1$ eV and $\hbar\gamma = 0.1$ eV. The refractive index and the extinction coefficient of the Drude term can be found using Eq. (46) and Eq. (36)

$$n = \left(\frac{1}{\sqrt{2}}\right) \sqrt{1 - \frac{\omega_p^2}{\gamma^2 + \omega^2} + \sqrt{\frac{\gamma^2 + \omega^2 + (\omega^2 - \omega_p^2)^2}{\omega^2(\gamma^2 + \omega^2)}}} \tag{47}$$

$$k = \left(\frac{1}{\sqrt{2}}\right) \sqrt{-1 + \frac{\omega_p^2}{\gamma^2 + \omega^2} + \sqrt{\frac{\gamma^2 + \omega^2 + (\omega^2 - \omega_p^2)^2}{\omega^2(\gamma^2 + \omega^2)}}}. \tag{48}$$

One can easily write these equations in terms of energy by substituting $\omega \to E$ and $\gamma \to \Gamma$. Assuming that $\gamma \ll \omega_p$ both n and k reach their minimum ($1/\sqrt{2\sqrt{\omega_p}}$) at ω_p and they both

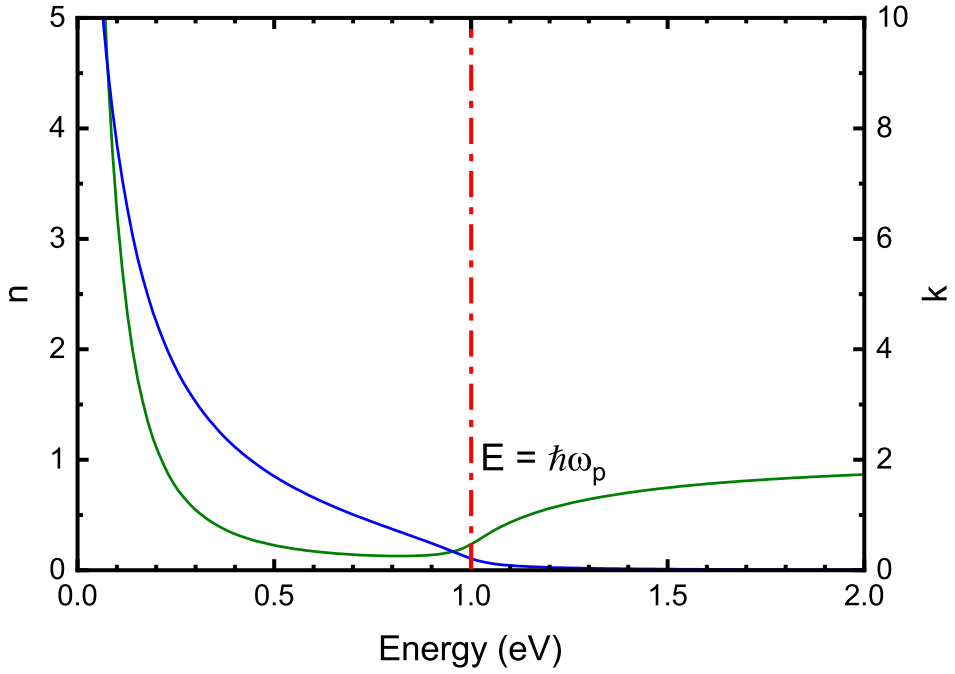

Figure 2.4: Refraction index n and extinction coefficient k for a Drude term defined in Fig. 2.3.

diverge as $\omega \to 0$ as illustrated in Fig. 2.4.

The optical conductivity is defined as

$$\begin{aligned} \sigma(\omega) &= -i\omega\epsilon_0[\epsilon(\omega) - 1], \\ \sigma(E) &= -\frac{i\epsilon_0 E}{\hbar}[\epsilon(E) - 1]. \end{aligned} \tag{49}$$

The quantity $\epsilon_0/\hbar = 134.52\ (\Omega\text{cmeV})^{-1}$ is very useful when extracting the optical conductivity from ellipsometry data. The optical conductivity can be simplified into its real and imaginary part as $\sigma = \sigma_1 + i\sigma_2$, where

$$\begin{aligned} \sigma_1(E) &= \frac{\epsilon_0}{\hbar} E\epsilon_2(E), \\ \sigma_2(E) &= \frac{\epsilon_0}{\hbar} E\left(1 - \epsilon_1(E)\right). \end{aligned} \tag{50}$$

We can now find the optical conductivity for the Drude term defined in Eq. (42)

$$\sigma_{Drude} = \frac{\epsilon_0}{\hbar}\left[\frac{A\Gamma}{E^2 + \Gamma^2} + i\frac{AE}{E^2 + \Gamma^2}\right] = \sigma_1 + i\sigma_2. \tag{51}$$

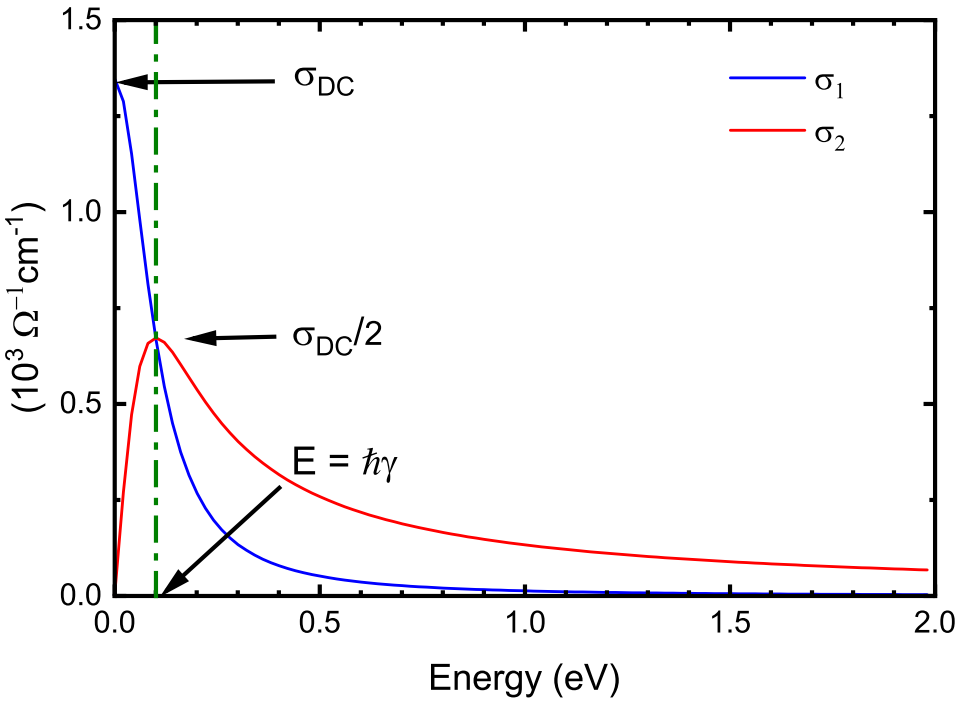

Figure 2.5: Real and imaginary part of the optical conductivity for a Drude term defined in Fig. 2.3. When there is only one carrier species, the real part of the optical conductivity has a maximum of σ_{DC} at $\hbar\omega = 0$ eV and the imaginary part has maximum of $\sigma_{DC}/2$ at the energy of $\hbar\omega = \hbar\gamma$). These relations do not hold when there are more than one type of free carriers.

Using Eq. (51) one can find the DC conductivity, which is defined as the case when $E \to 0$

$$\sigma_{DC}^{Drude} = \frac{\epsilon_0}{\hbar}\left(\frac{A}{\Gamma}\right). \tag{52}$$

The unit of σ_{DC} in Eq. (5.4) is $(\Omega\text{cm})^{-1}$ because $A = E_p^2$ is in units of eV^2 and Γ in units of eV, and $\epsilon_0/\hbar$ is in units of $(\Omega\text{cmeV})^{-1}$. As shown in Fig. 2.5 , when there is only one carrier species, $\sigma_1(\omega)$ has a maximum of σ_{DC} at $\omega = 0$, and $\sigma_2(\omega)$ has a maximum of $\sigma_{DC}/2$ at $\omega = \gamma$.

The loss function

$$\Im\left(-\frac{1}{\epsilon}\right) = \frac{\epsilon_2^2}{\epsilon_1^2 + \epsilon_2^2} \tag{53}$$

can be found for the Drude term, which yields

$$\Im\left(-\frac{1}{\epsilon}\right) = \frac{\gamma\omega\omega_p^2}{\gamma^2\omega^2 + (\omega^2 - \omega_p^2)}. \tag{54}$$

Equation (54) shows that the value of loss function for free carriers has a peak at $\omega = \omega_p$ with the maximum of ω_p/γ as demonstrated in Fig. 2.6. Figures 2.7 shows the ellipsometric angles ψ and Δ as a function of energy for one Drude term with $\hbar\omega = 1$ eV and $\hbar\gamma = 0.1$ eV. For this case when the angle of incidence $\theta = 0°$, ψ is always equal to 45° and $\Delta = 180°$. Therefore, Fig. 2.7 is simulated for an angle of incidence of 1°. The small dips in the ellipsometric angles are not detectable in measured data. The inset of Fig. 2.7 shows the ellipsometric angels at the angle of incidence of $\theta = 70°$. Using the extinction coefficient, the absorption coefficient $\alpha = 4\pi k/\lambda$ is plotted in Fig. 2.8 as a function of energy of the incident beam. The figure shows that for one type of carriers, there is a drastic decrease in the absorption coefficient for energies below the scattering rate and above the plasma energy. Most of the absorption occurs when the energy of the incident beam is between the scattering rate and the plasma energy. If there are more than one carrier species, one can easily write the dielectric function as a sum of Drude terms

$$\epsilon(\omega) = 1 - \sum_{i=1}^{n} \frac{\omega_{p,i}^2}{\omega^2 + i\gamma_i\omega}. \tag{55}$$

In this case, the DC conductivity is the sum of the conductivities [41]

$$\sigma_{DC,total} = \sum_{i=1}^{n} \sigma_{DC,i} = \frac{\epsilon_0}{\hbar} \sum_{i=1}^{n} \left(\frac{A_i}{\Gamma_i}\right). \tag{56}$$

One should note that when there are n carrier species, the loss function does not show n peaks. The loss function in this case is complicated. Figure 2.9 shows an example of this case with two Drude terms with $\hbar\omega_{p1} = 2$ eV, $\hbar\omega_{p2} = 3$ eV and $\hbar\gamma_1 = \hbar\gamma_2 = 0.1$ eV.

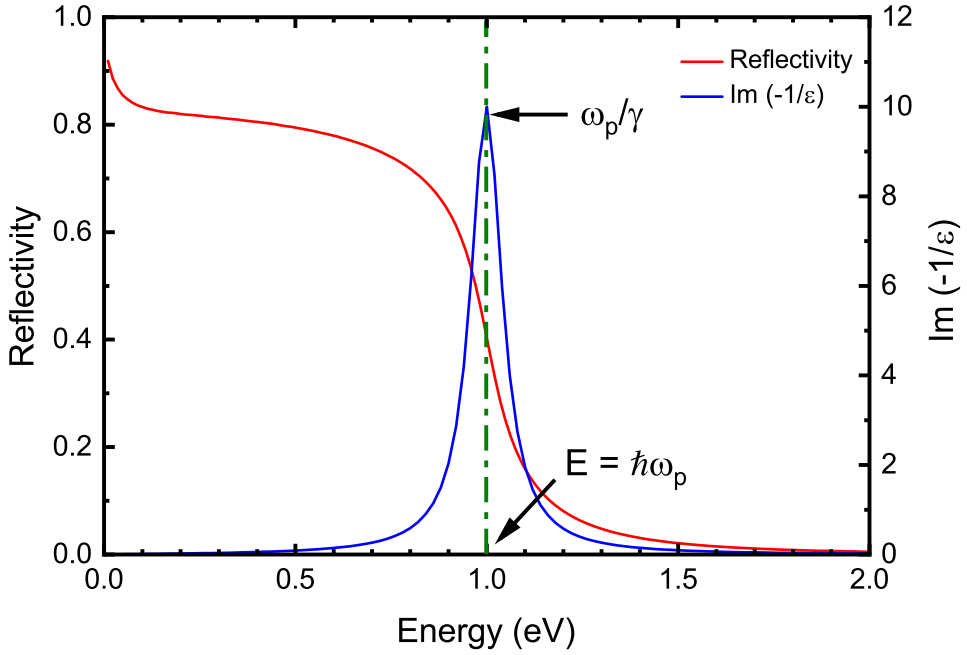

Figure 2.6: Reflictivity and loss function of a Drude term. For one Drude term, there is a peak in the loss function at the plasma frequency with the maximum of ω_p/γ and the reflectivity drops drastically at the plasma frequency.

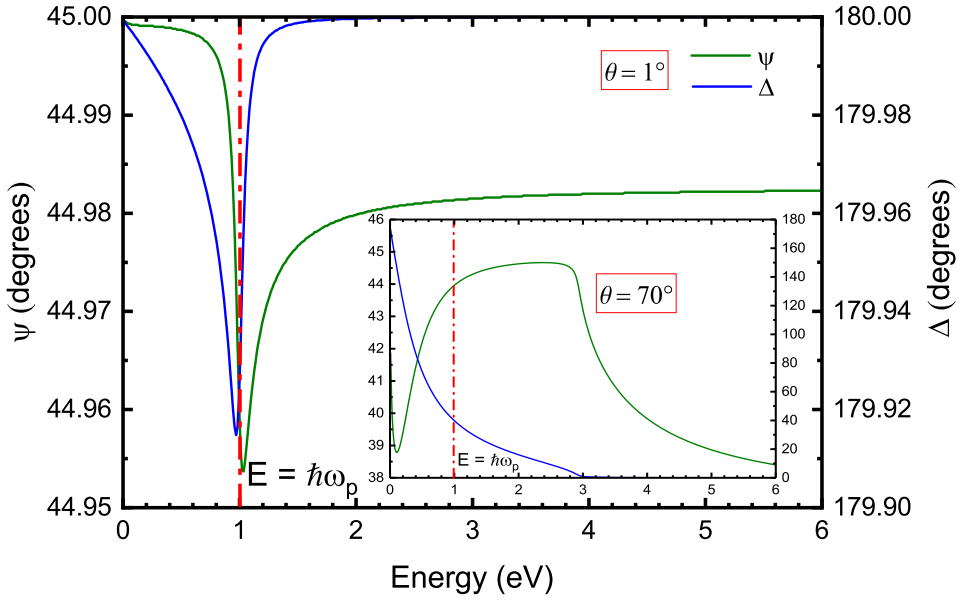

Figure 2.7: Ellipsometric angles for a Drude term defined in Fig. 2.3 $\hbar\omega_p = 1$ eV and $\hbar\gamma = 0.1$ eV. When the angle of incidence is zero, $\psi = 45°$ and $\Delta = 180°$, respectively. For clarity we show the ellipsometric angles for the angle of incidence $\theta = 1°$, where ψ and Δ are practically 0° and 180°,respectively, and the small dips at plasma frequency are not observable in measured data. The inset shows the ellipsometric angles at $\theta = 70°$.

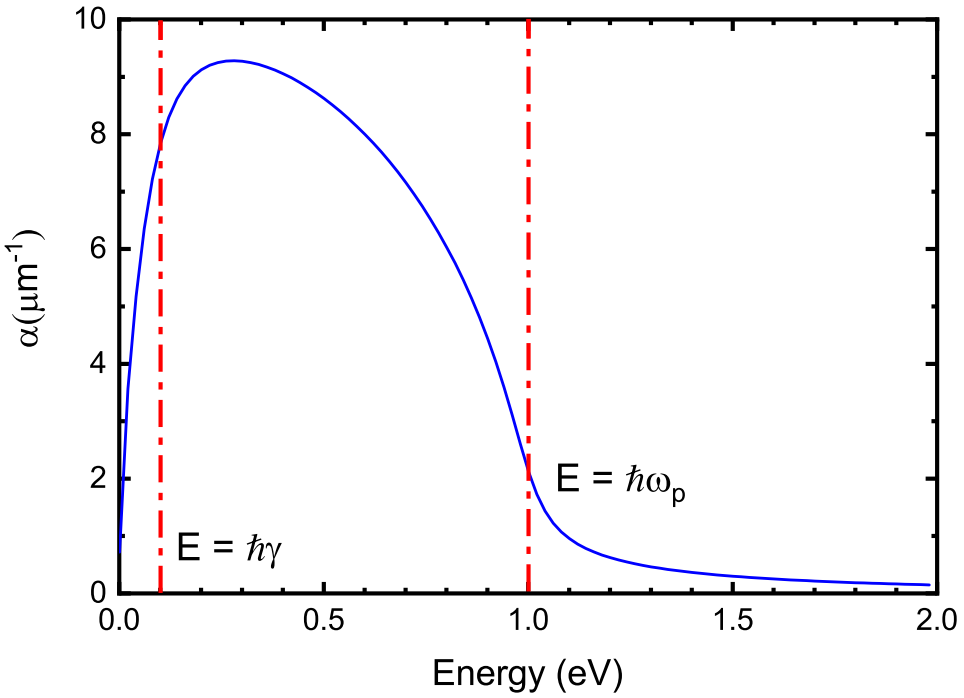

Figure 2.8: The absorption coefficient of a Drude term defined in Fig. 2.3. There is a drastic drop in the absorption coefficient below the scattering rate and above the plasma frequency.

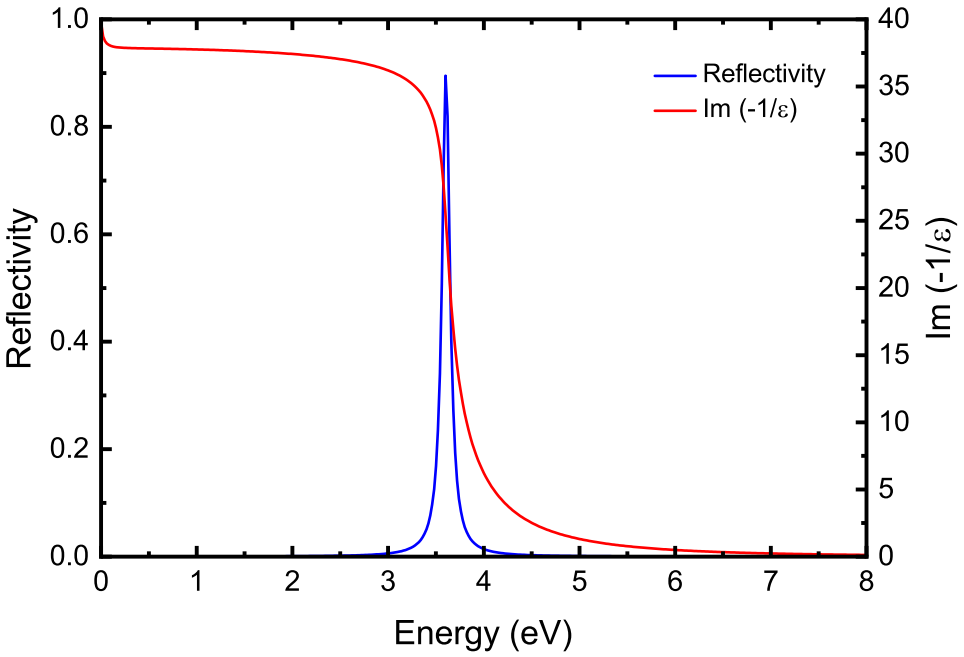

Figure 2.9: Reflectivity and loss function for two Drude terms with $\hbar\omega_{p1} = 2$ eV, $\hbar\omega_{p2} = 3$ eV, and $\hbar\gamma_1 = \hbar\gamma_2 = 0.1$ eV. The peak in the loss function and the drastic drop in the reflectivity do not occur at any of the plasma frequencies. In fact there is no simple relation between the Drude parameters and the position and the height of the peak in the loss function when there are more than one carrier species.

2.3.3 Lattice Absorption

When the frequency of the electromagnetic wave is the same as the resonance frequency of a crystal, the wave is absorbed and causes vibrations in the lattice of the crystal. These vibrations do not have random frequencies, but they are an integer factor of a specific frequencies that are defined by the bonding between the elements of the crystal. The quanta of the lattice vibration are called phonons. The phonons are classified into optical and acoustic ones. The optical phonons are the out-of-phase vibration of the lattice and the acoustic phonons are the in-phase and coherent vibration of the lattice. The vibrations where the atoms oscillate perpendicular to the propagation vector of the light are called transverse phonons and the oscillations along the propagation vector are called longitudinal phonons. As light is a transverse wave, it excites only transverse optical phonons at the frequency of ω_{TO}. The absorption of light by lattice occurs only when the crystal has a dipole moment. For example, the NaCl crystal has ionic bonding between the Na and Cl atoms. Therefore, they can cause dipole absorption, whereas elemental crystals like Ge or Si have a covalent bond and do not cause a dipole absorption. Therefore, the phonons in elemental crystals cannot be excited by light.

A phonon absorption in a crystal can be described by a Lorentzian oscillator defined as [39]

$$\epsilon(\omega) = 1 + \frac{A\omega_{TO}}{\omega_{TO}^2 - \omega^2 - i\gamma\omega}, \tag{57}$$

which can be simplified into its real and imaginary part

$$\begin{aligned} \epsilon_1(\omega) &= 1 + \frac{A\omega_{TO}(\omega_{TO}^2 - \omega^2)}{(\omega_{TO}^2 - \omega^2)^2 + \gamma^2\omega^2}, \\ \epsilon_2(\omega) &= \frac{A\omega_{TO}\gamma\omega}{(\omega_{TO}^2 - \omega^2)^2 + \gamma^2\omega^2}. \end{aligned} \tag{58}$$

The refractive index and the extinction coefficient can be derived by substituting Eq. (58) into Eq. (36)

$$n = \left(\frac{1}{\sqrt{2}}\right)\sqrt{1 + \frac{A\omega_{TO}\left(\omega_{TO}^2 - \omega^2\right)}{\gamma^2\omega^2 + \left(\omega_{TO}^2 - \omega^2\right)^2} + \sqrt{\frac{\gamma^2\omega^2 + \left(\left(\omega_{TO}^2 - \omega^2\right) + A\omega_{TO}\right)^2}{\gamma^2\omega^2 + \left(\omega_{TO}^2 - \omega^2\right)^2}}} \tag{59}$$

and

$$k = \left(\frac{1}{\sqrt{2}}\right)\sqrt{-1 - \frac{A\omega_{TO}\left(\omega_{TO}^2 - \omega^2\right)}{\gamma^2\omega^2 + \left(\omega_{TO}^2 - \omega^2\right)^2} + \sqrt{\frac{\gamma^2\omega^2 + \left(\left(\omega_{TO}^2 - \omega^2\right) + A\omega_{TO}\right)^2}{\gamma^2\omega^2 + \left(\omega_{TO}^2 - \omega^2\right)^2}}}. \tag{60}$$

Here, A is the oscillator strength, γ is the scattering rate of the phonons, and ω_{TO} is the transverse optical frequency of the lattice. Figure 2.10(B) shows the real and imaginary part of the dielectric function of a Lorentzian oscillator with $A = 1$, $\hbar\omega_{TO} = 1$ eV, and $\hbar\gamma = 0.1$ eV. For a Lorentzian oscillator, ϵ_2 has a peak at ω_{TO} with the maximum of A/γ and FWHM of γ. The scattering rate reflects the damping effect that the presence of the other atoms have on the oscillating dipole. If the scattering rate is zero, the extinction coefficient k becomes zero and the oscillator vibrates for an infinite amount of time and the incident light does not get attenuated. The real part of the dielectric function has extrema at $\sqrt{(\omega_{TO}^2 \pm \gamma\omega_{TO})}$ with the maximum and minimum of

$$\begin{aligned}
\epsilon_1\left(\omega = \sqrt{(\omega_{TO}^2 - \gamma\omega_{TO})}\right) &= 1 + \frac{\gamma\omega_{TO}^2}{\gamma^2\omega_{TO}^2 + \gamma^2(\omega_{TO}^2 - \gamma\omega_{TO})}, \\
\epsilon_1\left(\omega = \sqrt{(\omega_{TO}^2 + \gamma\omega_{TO})}\right) &= 1 - \frac{\gamma\omega_{TO}^2}{\gamma^2\omega_{TO}^2 + \gamma^2(\omega_{TO}^2 + \gamma\omega_{TO})},
\end{aligned} \tag{61}$$

respectively.

Figure 2.10(A) demonstrates the reflectivity for a Lorentzian oscillator. The region where the reflectivity is maximum is called Reststrahlen band. If the scattering rate is zero, this region has a reflectivity of 1. As the scattering rate increases, the reflectivity at this region decreases

as shown in Fig. 2.10(A) . This region occurs at normal incidence when the frequency of the incident beam is between the optical transverse frequency (ω_{TO}) and the optical longitudinal frequency (ω_{LO}), and ω_{LO} is defined as the frequency where $\epsilon_1 = 0$, which makes the propagation of longitudinal phonons possible. For semiconductors with band gaps far away from the phonon absorption, one can use the LST relation to find the relation between ω_{TO} and ω_{LO} [39]

$$\frac{\omega_{LO}}{\omega_{TO}} = \frac{\epsilon_{st}}{\epsilon_{\infty}}, \tag{62}$$

where ϵ_{st} is the dielectric constant at $\omega = 0$ and ϵ_{∞} is the dielectric function at high frequencies ($\omega \gg \omega_{LO}$) but still far below the bandgap. If there are more than one phonon absorption, one can write the phonon contribution to the dielectric function as a sum as follows

$$\epsilon(\omega) = 1 + \sum_{i=0}^{n} \frac{A_i \omega_{TO,i}}{\omega_{TO.i}^2 - \omega^2 - i\gamma_i \omega}. \tag{63}$$

One should note that applying Eq. (49) to the dielectric function of phonons to find the optical conductivity is not valid because phonon absorption does not cause a conductivity in the material. However, the scattering of free electrons with phonons reduces the DC conductivity. This topic will be discussed in chapter 5.

2.3.4 Electronic Absorption

The minimum energy required to excite an electron from the valence band to the conduction band is called the band gap (E_g) of the crystal. A thorough discussion of the band gap and the electronic properties of semiconductors can be found in Ref. 42. Excitation of an

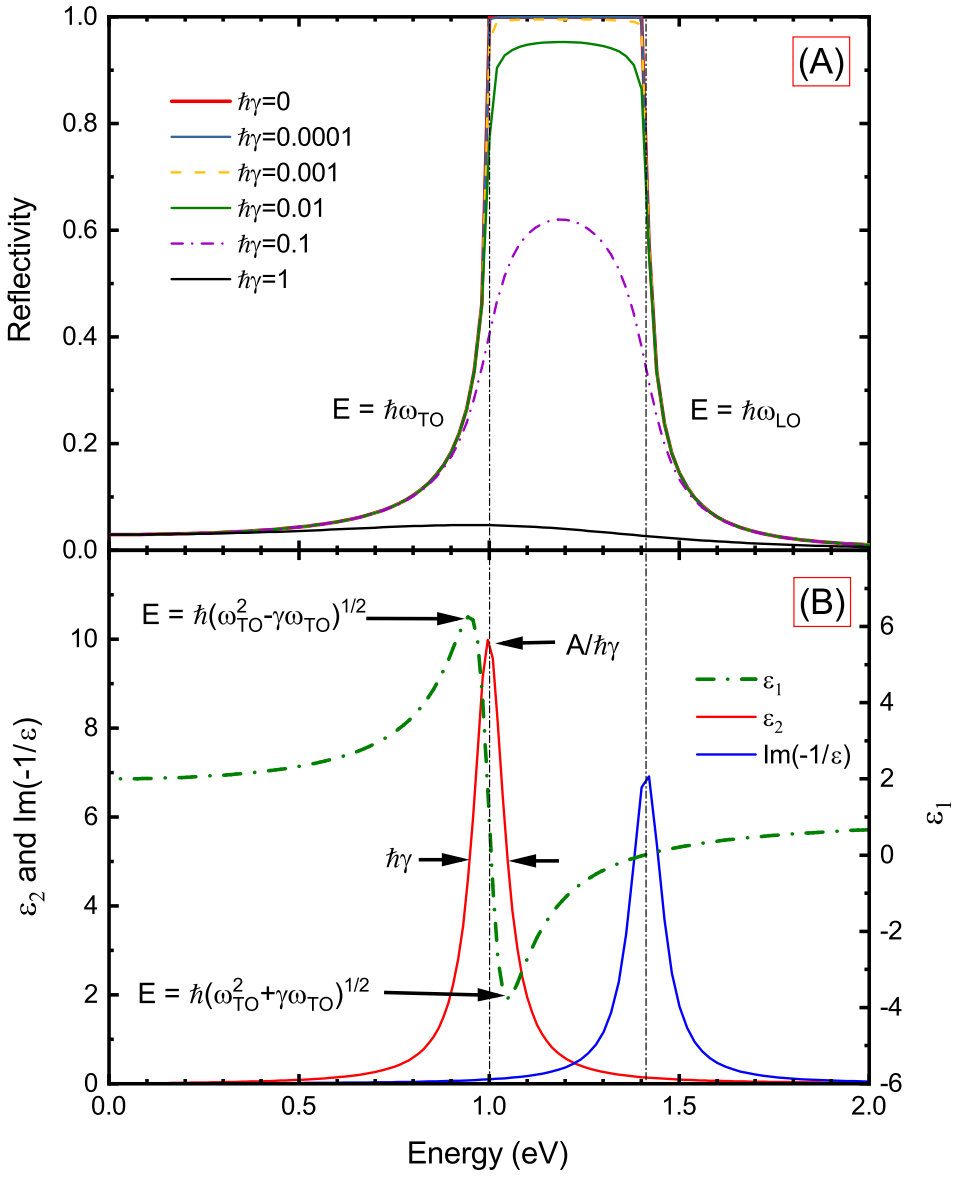

Figure 2.10: (A) reflectivity of a Lorentzian oscillator with $A = 1$, $\hbar\omega_{TO} = 1$ eV, and various values of $\hbar\gamma$. As γ increases, the reflectivity in the reststrahlen band decreases and corners are rounded. (B) real and imaginary part of the dielectric function, and loss function for a Lorentzian oscillator with $A = 1$, $\hbar\omega_{TO} = \ 1eV$, and $\hbar\gamma = 0.1$ eV. The peak in ϵ_2 occurs at ω_{TO} and has an FWHM equal to $\hbar\gamma$ and the maximum of $A/\hbar\gamma$. The peak in the loss function occurs at ω_{LO}. The figure also shows the energies at which the minimum and maximum of ϵ_1 take place.

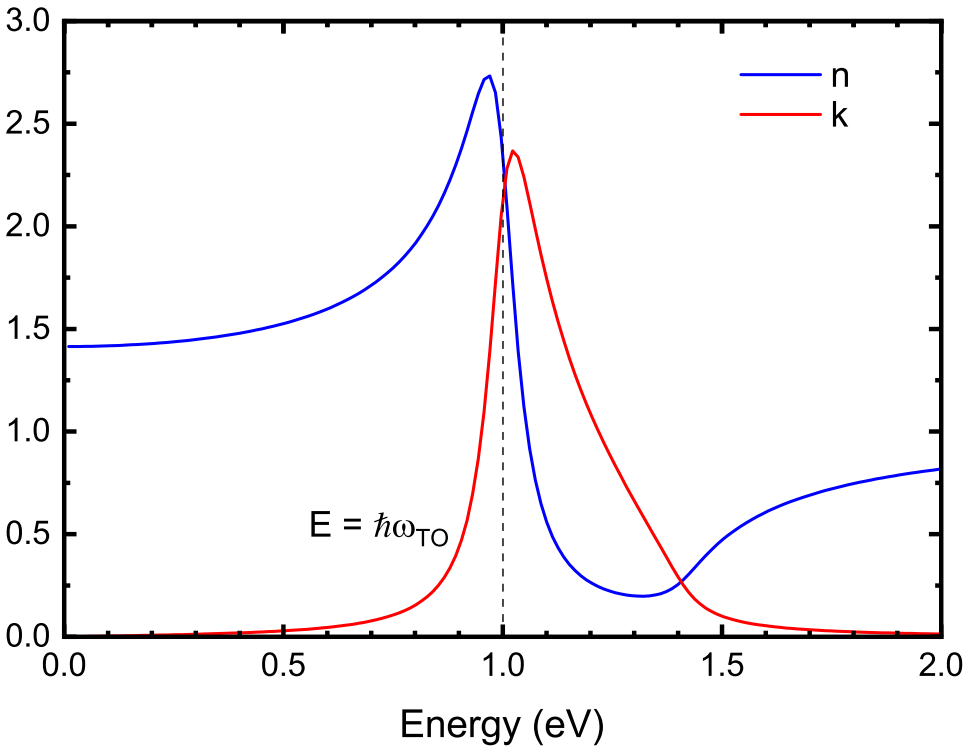

Figure 2.11: Refractive index n and extinction coefficient k of a Lorentzian oscillator defined in Fig. 2.10(B)

electron to the conduction band can also be discussed by using Eq. (57) with a slightly different notation and meaning of the parameters

$$\epsilon(\omega) = 1 + \frac{A\omega_0}{\omega_0^2 - \omega^2 - i\gamma\omega}, \tag{64}$$

where ω_0 is the energy required to excite an electron from the valence band to the conduction band, and γ is the scattering rate of the electrons. As there are usually more than one type of electronic absorption, one needs to use many Lorentz oscillators to describe the contribution of the interband absorption to the dielectric function of materials. In general, the total dielectric function of a crystal is written as

$$\epsilon = 1 + \chi_{FC} + \chi_{ph} + \chi_e, \tag{65}$$

where

$$\chi_{FC}(\omega) = \sum_{i=1}^{n} -\frac{\omega_{p,i}^2}{\omega^2 + i\gamma_i\omega},$$
$$\chi_{ph}(\omega) = \sum_{i=1}^{n} \frac{A_i\omega_{TO,i}}{\omega_{TO,i}^2 - \omega^2 - i\gamma_i\omega}, \tag{66}$$
$$\chi_e(\omega) = \sum_{i=1}^{n} \frac{A_i\omega_{0,i}}{\omega_{0,i}^2 - \omega^2 - i\gamma_i\omega}.$$

To find the optical conductivity of a material one should substitute Eq. (65) into Eq. (49). The DC conductivity is still driven by the free carriers since the optical conductivity due to interband transitions has the form of

$$\sigma_{Lorentz}(\omega) = \sigma_1(\omega) + i\sigma_2(\omega) = \frac{\epsilon_0\gamma\omega_0\omega^2}{(\omega_0^2 - \omega_2)^2 + \gamma^2\omega^2} - i\frac{\epsilon_0\omega_0\omega(\omega_0^2 - \omega^2)}{(\omega_0^2 - \omega_2)^2 + \gamma^2\omega^2}. \tag{67}$$

Both terms in Eq. (67) vanish when $\omega \to 0$. Therefore, interband transitions do not contribute to the DC conductivity of a crystal. Figure 2.12 demonstrate the optical conductivity of interband transitions described by a Lorentz oscillator with $A = 1$, $\hbar\omega_0 = 1$ eV, and $\hbar\gamma = 0.1$ eV.

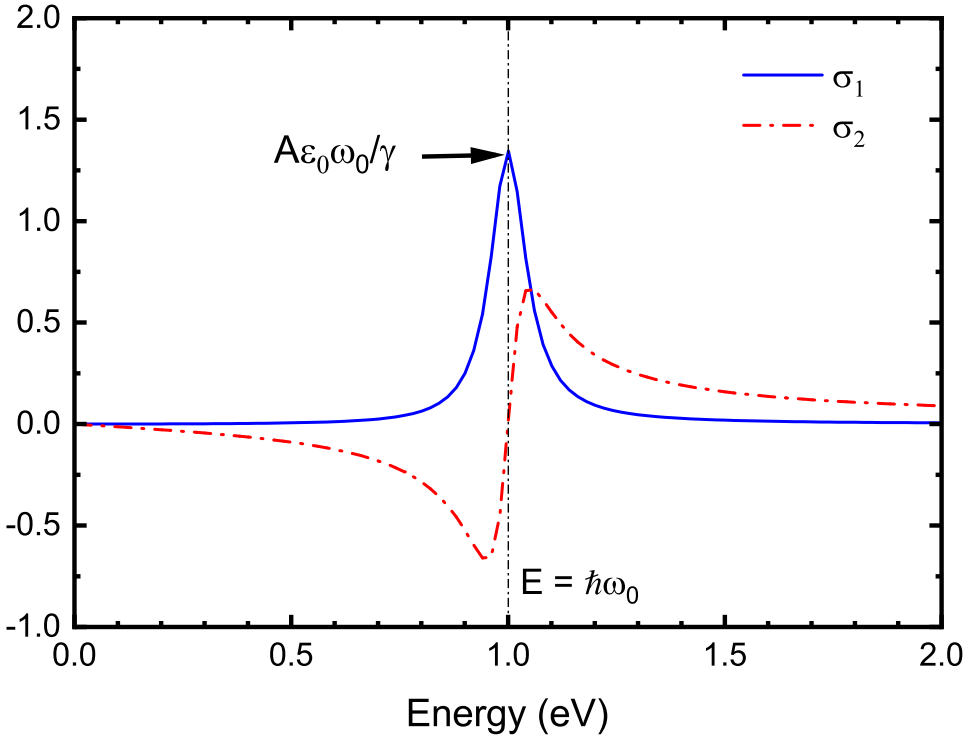

Figure 2.12: The optical conductivity of a Lorentzian oscillator with an interband energy $\hbar\omega_0 = 1$ eV, amplitude $A = 1$, and scattering rate of $\hbar\gamma = 0.1$ eV. The real part of the optical conductivity has a maximum of $\frac{A\epsilon_0\omega_0}{\gamma}$ at the energy of $\hbar\omega_0$. Both real and imaginary part of the optical conductivity vanish at $\omega = 0$, hence interband transitions described by Lorentz oscillators do not contribute to the DC conductivity of the crystal.

3 EXPERIMENTAL SETUP

Figures 3.1 and 3.2 show the two instruments that were used to measure the ellipsometric angles of Ni in air as well as in the cryostat at different temperatures. The J. A. Woollam VASE (Variable Angle Spectroscopic Ellipsometer) has an Xe arc light source with the spectrum of 0.5 eV to 6.5 eV (190 nm to 2 μm) as is shown in Fig. 3.3. This ellipsometer can measure the optical properties of a sample in air in the range of angles of incidence between 15° and 90°. The Xe lamp emits unpolarized light, which goes through a monochromator with low pass filters and is transferred via an optical fiber into the box called "incident beam" in Fig. 3.1 where it goes through a polarizer and a Bereth wave plate compensator (retarder) to become polarized. The polarized light then irradiates the sample and its polarization changes upon reflection off the sample before it enters the detector unit where the light goes through a rotating analyzer towards the detector. The detector of this instrument consists of a Si photodiode detector (1.1 eV to 6.5 eV) and an InGaAs photodiode detector for lower energies. The transition of the detectors occurs at the band gap of Si (1.14 eV). This transition does not affect the ellipsometric angles in a typical ellipsometry measurement. However, a small step in the off-diagonal measurements of an MM-measurement is observed at this energy. All measurements that we have taken in this work have an energy step size of 20 meV.

For temperature dependent measurements a sample is mounted inside a JanisST-400 UHV cryostat as is demonstrated in Fig. 3.1. All measurements in the cryostat are performed at an angle of incidence of 70°. However, the entrance and exit windows of this cryostat have a 3° angle offset to avoid multiple reflections of light by windows. These windows are

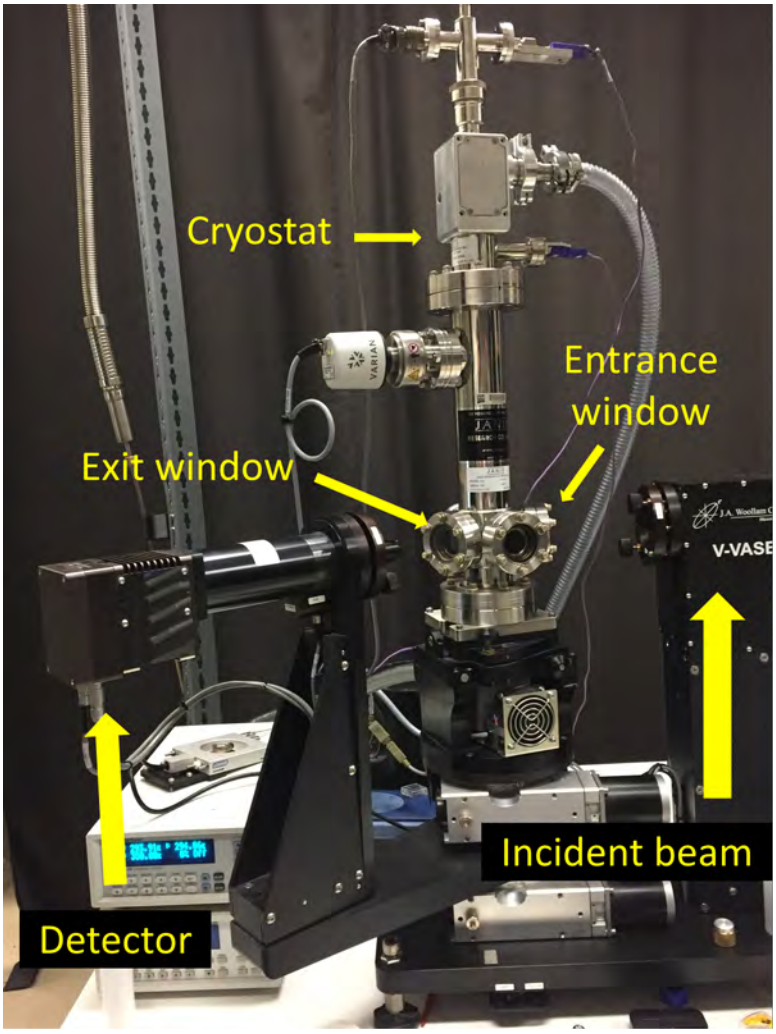

Figure 3.1: VASE ellipsometer (spectral range from 0.5 eV to 6.5 eV) with a cryostat attached for temperature dependent measurements. The VASE cryostat has quartz windows with a transparent region between 0.45 eV and 6.6 eV.

made out of fused silica (quartz) which is transparent between 0.45 eV and 6.6 eV. Using a roughing pump and a turbo pump, one can achieve a pressure below 10^{-9} Torr at 77 K and 10^{-7} Torr at 770 K. The pressure is in the range of 10^{-9} Torr at room temperature. The cryostat can be used for measurements from 4 K to 800 K.

Figure 3.2 shows the FTIR (Fourier transform infrared) ellipsometer that is utilized for

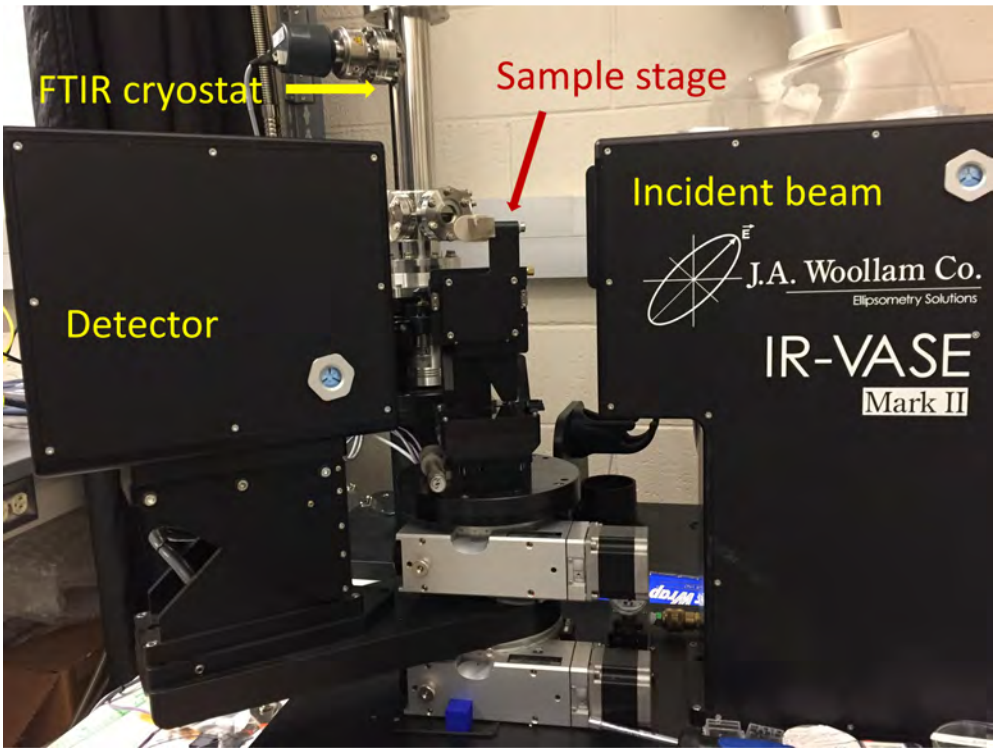

Figure 3.2: FTIR ellipsometer (spectral range from 0.03 eV to 0.8 eV). The sample stage in the picture is used for measurements at room temperature on small samples. The FTIR cryostat with diamond windows can be seen in the back.

the measurements in the IR range. The light source of this instrument is a globar, which is a silicon carbide bar that is heated electrically to produce black body spectrum. Figure 3.3 shows the baseline of this light source which emits from 0.03 eV to 0.8 eV. There is no monochromator in this instrument and the whole spectrum is detected at the same time by a Michelson Fourier-transform interferometer detector. A polarizer, which is usually fixed

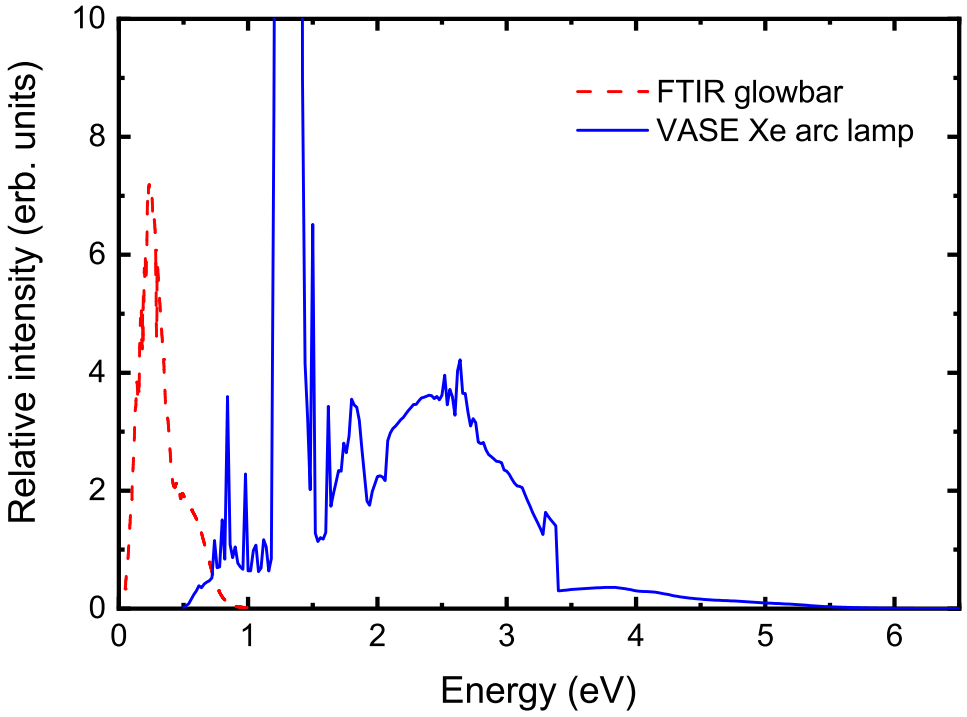

Figure 3.3: Baseline spectra of the VASE (solid) and the FTIR (dashed) light source. The Xe arc lamp of the VASE emits light from 0.5 eV to 6.5 eV. The two spikes in the spectrum of the Xe lamp are due to the discrete emission lines of Xe that occur at 880 nm and 1010 nm. The FTIR globar emits from 0.03 eV to 0.8 eV.

at 45°, is mounted at the source side, while the compensator and analyzer are located at the detector side. The position of the compensator matters only in MM measurements. All measurements in this work were taken with a resolution of 16 cm^{-1} which is 2 meV.

The cryostat that is used for IR ellipsometry measurements is identical to the VASE cryostat except for the windows. Different types of view ports exist that can be used based on the desired range of measurements. The ZnSe view ports are very common because they are transparent between 0.06 eV and 1.7 eV and relatively inexpensive. For measurements at lower energies one can use diamond windows, which are transparent between 0.01 eV and 5.4 eV. The temperature and the pressure range are the same as those of the VASE cryostat.

4 OPTICAL PROPERTIES OF POLY-CRYSTALLINE NI FROM 0.06 eV TO 6.0 eV AT 300 K

This article was published in the Journal of Vacuum Science and Technology B, volume **37**, 062920 (2019).

Farzin Abadizaman[1] and Stefan Zollner[1,2]

1. Department of Physics, New Mexico State University, P.O. Box 30001, Las Cruces, NM 88003, USA

2. Fyzikální ústav AV ČR, v.v.i., Sekce optiky, Na Slovance 2, CZ-18221 Praha 8, Czech Republic

4.1 Abstract

Using spectroscopic ellipsometry from 0.06 to 6.0 eV at room temperature, we determined the optical constants (complex dielectric function, refractive index, optical conductivity) of bulk cold-rolled polycrystalline Ni. To reduce the thickness of surface overlayers, the sample was heated in ultrahigh vacuum at 750 K for 6 hours and then kept in vacuum during measurements. We analyze the optical constants using three alternative, but mutually exclusive methods: we write the dielectric function as a multiband sum or product of Drude and Lorentz oscillators or with a Drude model with a frequency dependent scattering rate and plasma frequency. Below 1 eV, we find significant contributions from both d-intraband transitions and free carriers.

4.2 Introduction

Determining the complex dielectric function (DF) of bulk metals [43–45] is difficult, since one needs to minimize overlayers and surface roughness. For example, a Ni surface in air can be covered with a 50 Å thick film of water (or an adsorbed layer with similar optical constants), which is removable by annealing [46]. It is easier to achieve smooth surfaces of semiconductors than of metals. Clean metal surfaces are best prepared in ultra-high vacuum (UHV). Ellipsometry measurements should then be performed in UHV without breaking vacuum, to maintain a clean surface. This requires window corrections, since vacuum chamber windows disturb the polarization of the incident and reflected light beams [32, 48].

As early as 1969, Shiga and Pells [49] overcame these difficulties and measured the optical absorption of annealed polycrystalline bulk Ni from 0.5 to 6.0 eV at temperatures from 300 to 770 K in UHV using a rotating-analyzer ellipsometer [50]. Similar ellipsometry measurements of Ni at room temperature were performed by Lenham and Treherne [51, 52] at selected infrared wavelengths between 5 and 20 μm. Lynch, Rosei, and Weaver [53] measured the absorptivity of single-crystalline Ni at 4.2 K from 0.08 to 3.0 eV using a calorimetric technique and determined the DF by Kramers-Kronig transform. At higher photon energies (0.5 to 6.5 eV), Johnson and Christy [54] calculated the DF of evaporated semitransparent (20−50 nm thick) Ni thin films in nitrogen atmosphere from transmission and reflection data. A review of the early DF results of Ni was given by Lynch and Hunter in Palik's handbook [43]; also by Adachi [45]. More recently, ellipsometry measurements were also performed on $Ni_{1-x}Pt_x$ thin films for applications in semiconductor manufacturing metrology [9, 46, 47].

Considering the advances in spectroscopic ellipsometry and vacuum techniques over the last 50 years, it seems worthwhile to revisit the optical constants of Ni and determine the DF from 0.06 to 6.0 eV with improved accuracy. We tabulate parameters to calculate the optical constants of Ni using model DFs. We are particularly interested in the relative contributions to ϵ from free carriers and interband optical transitions. We also study the frequency dependence of the scattering rate and of the plasma frequency.

4.3 Experimental Methods

Several 10×10 mm^2 substrates of cold-rolled polycrystalline Ni (>99.9% purity) with 1 mm thickness were obtained commercially [55]. No preferred orientation was seen with powder x-ray diffraction. These pieces had a grain size of $10-50$ μm and an rms surface roughness of $1-3$ nm (measured with atomic force microscopy in 20×20 μm^2 scans and x-ray reflectance). Before our ellipsometry measurements, all samples were heated to 750 K for six hours in ultra-high vacuum (UHV) to remove adsorbed overlayers and then kept in vacuum during the measurements. No significant change in surface roughness was observed after annealing in UHV.

It was reported previously [56] that there is an anomaly in the optical response of Ni (bulk single- or poly-crystalline or sputtered thin film), as the sample is heated in UHV beyond the Curie temperature (627 K), see Fig. 4.1. Initially, we attributed this anomaly to three potential causes: (i) changes in the magnetic structure (transition between ferromagnetic and paramagnetic phase at the Curie temperature), (ii) bulk crystal structure of the sample, for example grain growth after annealing [57], (iii) surface overlayers.

Since we find this anomaly in single-crystalline and poly-crystalline bulk substrates as

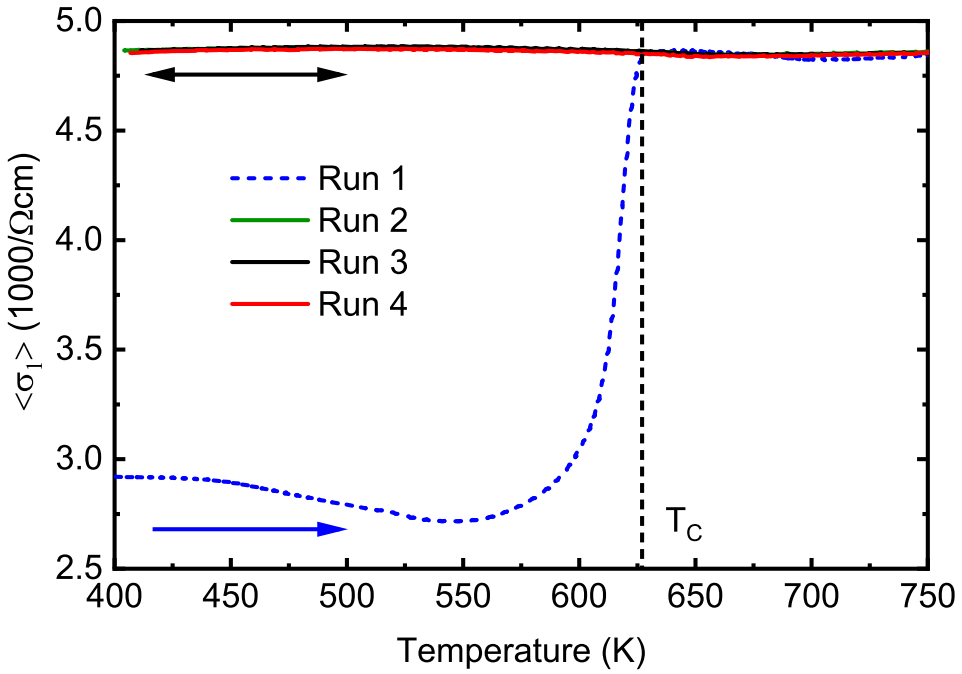

Figure 4.1: Optical pseudo-conductivity of a 1000 Å thick Ni layer on thick SiO_2 on a Si substrate as a function of temperature, measured by ellipsometry in ultra-high vacuum at a single photon energy of 1.97 eV at an incidence angle of 70°. Compare Fig. 4.9 with data for poly- and single-crystalline Ni.

well as in thin layers (see Fig. 4.9), we conclude that the grain size or other structural changes due to annealing are not a likely cause of our anomaly. Since it is irreversible (only occurs during the initial heating of the substrate) and cannot be restored by placing the sample in a saturating magnetic field, while the phase transition (ferromagnetic to paramagnetic) at the Curie temperature is reversible, the anomaly cannot be a magnetic effect. The most likely explanation for this anomaly is therefore degassing of the sample surface, for example by evaporation of adsorbed overlayers. Additional details are given in the supplemental material. Heating the Ni sample in UHV was the most effective cleaning method we were able to find.

The ellipsometric angles from 0.06 to 6.0 eV at 70° incidence angle were acquired at room temperature on two different ellipsometers (J. A. Woollam FTIR-VASE and J. A.

Woollam VASE, Lincoln, NE, USA) as described elsewhere [41]. From 0.5 to 6.0 eV, we used a commercial UHV chamber (Janis Research ST-400, Woburn, MA, USA) with strain-free quartz windows [56]. From 0.06 to 0.9 eV, we used a similar chamber, but with ZnSe windows. Changes in the polarization of the beam by the windows were corrected with a proprietary algorithm of the supplier. For data analysis, we assumed a surface roughness thickness of 20 Å. The surface roughness was described within the Bruggeman effective medium approximation as a 50/50 mixture of Ni and voids [14].

A similar experimental setup for rotating-analyzer ellipsometry measurements using Drude's method from 0.46 to 5.9 eV at temperatures from 77 to 950 K in a UHV chamber was already described in 1967 by Pells [50]. We extend this method further into the infrared spectral region with the use of a Fourier-transform spectrometer. Our setup also has increased accuracy due its computer-controlled Berek wave plate compensator and corrections for the effects of windows on the polarization of the incident and reflected light beam. Using their apparatus, Shiga and Pells [49] showed that Ni could be cleaned by heating at 770 K for at least twelve hours, confirming earlier photoemission results by Seib and Spicer [58, 59].

4.4 Experimental Results and Data Analysis

The ellipsometric angles ψ and Δ for bulk cold-rolled poly-crystalline Ni at room temperature are shown in Fig. 4.2 (symbols). If we assume a surface roughness of 20 Å, we can directly calculate the DF $\epsilon(\omega)$ and the optical conductivity

$$\sigma(\omega) = -i\epsilon_0\omega\left[\epsilon(\omega) - 1\right] \tag{68}$$

from the ellipsometric angles [14], see Figs. 4.3 and 4.4. This is known as a point-by-point fit. We also fit these data using multiband model DFs assuming 20 Å surface roughness, see below.

In our first multiband model, we write the DF as a sum of two Drude oscillators (to describe the optical response of free carriers) and several Lorentzians (to describe interband optical transitions of bound carriers) [14, 41]

$$\epsilon(\omega) = 1 + \chi_{\text{free}}(\omega) + \chi_{\text{bound}}(\omega), \tag{69}$$

$$\chi_{\text{free}}(\omega) = \sum_i \frac{\omega_{P,i}^2}{-\omega(\omega + i\gamma_{D,i})}, \tag{70}$$

$$\chi_{\text{bound}}(\omega) = \sum_i \frac{A_i \omega_{0,i}^2}{\omega_{0,i}^2 - \omega^2 - i\gamma_{0,i}\omega}, \tag{71}$$

where χ is the susceptibility, $\omega_{P,i}{=}n_i e^2/\epsilon_0 m_i$ the unscreened (unrenormalized, frequency-independent) plasma frequency, γ_D the (unrenormalized, frequency-independent) Drude scattering rate, A the dimensionless Lorentz amplitude, ω_0 the resonance frequency, and γ_0 the Lorentzian broadening. n_i is the density of the carrier species i and m_i their effective mass (also called the bare optical band mass) [60–62]. The parameters yielding the best fit to our data with this sum model are listed in Table 4.1

In our second multiband model, we write the dielectric function as a Kukharskii product [40, 41] of one Drude oscillator and several Lorentzians resulting in

$$\epsilon(\omega) = \frac{\omega_{\text{LP}}^2 - \omega^2 - i\gamma_{\text{LP}}\omega}{-\omega(\omega + i\gamma_D)} \prod_i \frac{\omega_{\text{L},i}^2 - \omega^2 - i\gamma_{\text{L},i}\omega}{\omega_{0,i}^2 - \omega^2 - i\gamma_{0,i}\omega}, \tag{72}$$

where ω_{LP} and γ_{LP} are the lower plasmon frequency and its broadening, while ω_0 is the Lorentz resonance frequency and ω_L the corresponding longitudinal frequency [41], where $\epsilon(\omega)$ crosses zero, with its broadening γ_L. (A second Drude factor was not needed to achieve

a good fit.) The parameters resulting in the best fit to our data with this product model are given in Table 4.2.

These two multiband models are identical only if the broadening parameters in the numerator and denominator are equal and much smaller than the differences between the resonance frequencies [41]. The additional broadening parameters in the numerators of the second (Kukharskii product) model offer flexibility by adding different widths to the zeros and poles of the dielectric function. The lower plasmon frequency ω_{LP} is usually smaller than the plasma frequency ω_P due to the repulsion by the longitudinal frequencies ω_L of bound carriers, similar to plasmon-phonon coupling in the Raman or infrared spectra of doped semiconductors [40, 41]. See Ref. 41 for the motivation of both models, additional details, and historical references.

The best fit to the ellipsometric angles using the product model is shown by the lines in Fig. 4.2. The best fit with a sum model yields similar results. The difference between the model and the data is no more than 0.3° for ψ and no more than 0.7° for Δ. Typical experimental errors from the measurement are 0.01° for ψ and 0.1° for Δ. The average mean square deviation between data and model is lower than the experimental errors, but there is a stastically significant difference between the data and both multiband models from 0.5 to 1.0 eV which we could not reduce with the addition of another oscillator.

The dielectric functions from the point-by-point fit and from the product model (72) are shown in Fig. 4.3. The corresponding optical conductivities are shown in Fig. 4.4. The loss function $-1/\epsilon$ is given in Fig. 4.5. We also show the complex refractive index in Fig. 4.11 and the absorption coefficient and the penetration depth in Fig. 4.12. The complex impedance in the infrared spectral region is shown in Fig. 4.18.

The third model to describe the optical constants of a metal assumes that the optical conductivity is due to a single species of free carriers (single-band model), leading to an optical conductivity of the form

$$\sigma(\omega) = \frac{\epsilon_0 \omega_P^2}{\gamma - i\omega} = \frac{\epsilon_0 \omega_P^2 \tau}{1 - i\omega\tau} = \frac{ne^2\tau}{m(1 - i\omega\tau)}. \tag{73}$$

If the Drude model with a single free carrier species truly describes the optical constants, then γ, τ, and m are frequency-independent constants. If, however, there is more than one carrier species or if the carriers interact with other elementary excitations or if there is a contribution to the conductivity from infrared-active optical phonons or interband transitions, then the scattering rate and mass need to be renormalized and depend on the angular frequency ω. The supplementary material lists the equations how these frequency-dependent quantitites can be calculated [62]. This method has been used to describe the optical constants of alkali metals [61], heavy Fermion compounds [62, 63], or correlated conducting metal oxides [64–67]. While this method has often been applied to investigate and interpret the optical conductivity determined from reflectance measurements, it is not widely known in the ellipsometry community. We are not aware of an application of this technique to transition metals with two species of free carriers.

4.5 Discussion

4.5.1 Optical Constants

There are significant differences between our optical constants and those in the literature [43, 46, 54]. see Fig. 4.6. Our *in situ* data of a polycrystalline Ni sample cleaned by heating and corrected for 2 nm surface roughness show the highest (lowest) values of ϵ_2 (ϵ_1) and

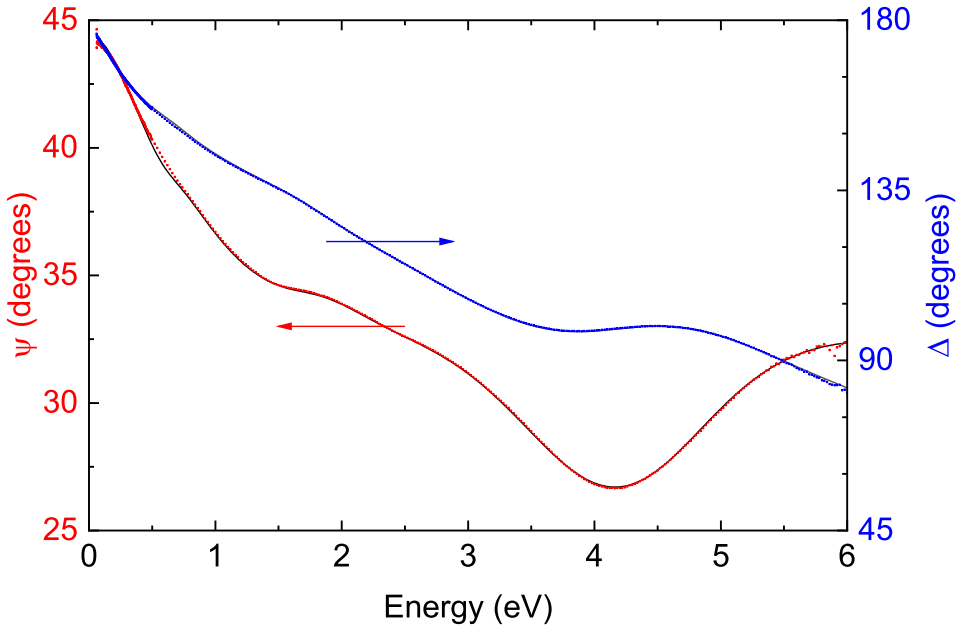

Figure 4.2: Ellipsometric angles ψ and Δ of clean poly-crystalline bulk Ni at room temperature. Symbols show experimental data, lines the best fit with a product model (72) with parameters in Table 4.2.

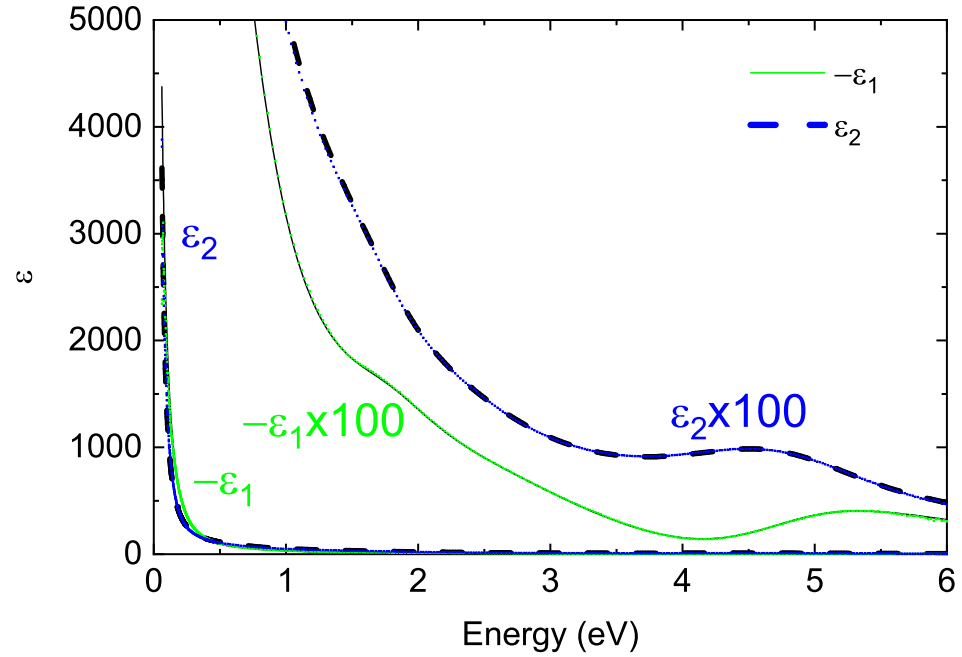

Figure 4.3: Dielectric function of poly-crystalline Ni determined from the ellipsometric angles shown in Fig. 4.2, assuming 2 nm surface roughness. Symbols show a point-by-point fit (without assuming a model dielectric function), while the lines show the dielectric function described by Eq. (72) with parameters in Table 4.2.

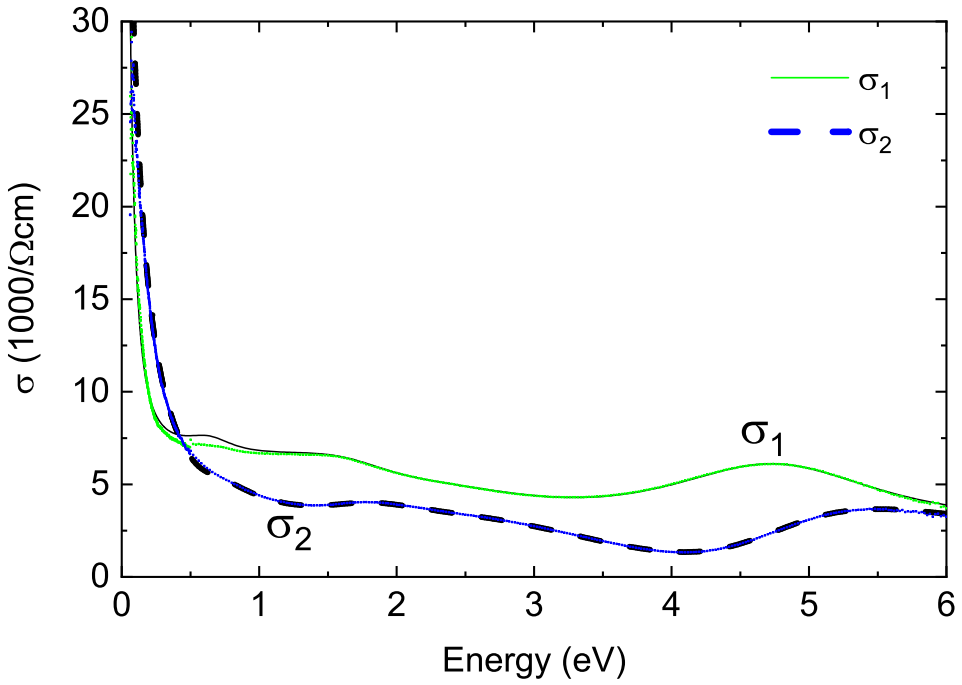

Figure 4.4: Same data as in Fig. 4.3, but displayed as an optical conductivity.

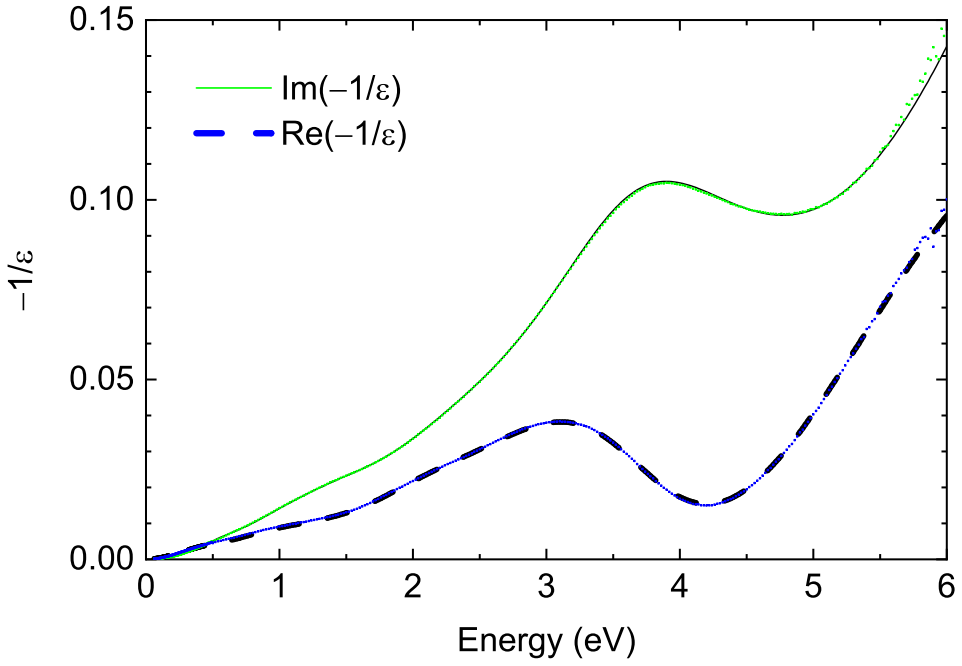

Figure 4.5: Same data as in Fig. 4.3, but as a loss function $-1/\epsilon$.

Table 4.1: Parameters used to describe the optical constants of polycrystalline Ni with a sum model: amplitude A, plasma frequency ω_P, energy ω_0, and broadening γ. All parameters are given with three significant digits. Due to parameter correlations, the uncertainty is probably much larger. The DC conductivity σ_0 was calculated from the Drude parameters using Eq. (92).

	A	$\hbar\omega_P$	$\hbar\omega_0$	$\hbar\gamma$	σ_0
	(1)	(eV)	(eV)	(eV)	(1/Ωcm)
Drude 1		11.9		2.87	6,640
Drude 2		4.86		0.0421	75,500
Lorentz 1	7.07		0.636	0.503	
Lorentz 2	3.52		1.56	1.06	
Lorentz 3	0.437		2.59	1.27	
Lorentz 4	2.90		4.80	2.17	
Lorentz 5	1.62		9.17	1.16	

Table 4.2: Parameters (in units of eV) used to describe the optical constants of polycrystalline Ni with a product model: longitudinal and transverse frequencies ω_0 and ω_L (or ω_{LP}) and the related broadenings γ_0 (or γ_D) and γ_L (or γ_{LP} for the Drude factor). All parameters are given with three significant digits. Due to parameter correlations, the uncertainty is probably much larger. (f) indicates that the parameter was fixed.

	$\hbar\omega_0$ (eV)	$\hbar\gamma_0$ (eV)	$\hbar\omega_L$ (eV)	$\hbar\gamma_L$ (eV)
Drude	0	0.0426	0.693	0.519
Lorentz 1	0.696	0.468	1.21	3.15
Lorentz 2	1.88	0.916	1.92	0.956
Lorentz 3	2.82	3.67	3.80	2.08
Lorentz 4	4.85	2.23	7.38	2.21
Lorentz 5	9.73	1.0(f)	19.5	1.0(f)

therefore likely represent the most pristine surface compared to other experiments, see Fig. 4.10. It is not likely that we over-corrected our ellipsometric angles to obtain the dielectric function, since our surface roughness was determined by atomic force microscopy and x-ray reflectance.

Johnson and Christy [54] as well as Vehse and Arakawa [68] briefly exposed their layers to air and measured in N_2 gas, likely leading to an adsorbed water layer, similar to Abdallah *et al.* [46] In the near-infrared region, our ϵ_1 data agree well with those of Johnson and Christy [54], but there is a large discrepancy for ϵ_2. This might also be related to cleaning, see Fig. 4.10. Data from Ref. 43 below 3.0 eV were acquired at 4 K on single crystals. Therefore, the structure at 1.5 eV is much more pronounced than in our data taken at 300 K. Also, the Drude scattering rate is expected to be much smaller at low temperatures and therefore the Drude divergence should be sharper at 4 K. This might explain the difference between our data and those listed by Lynch and Hunter [43] in the near-infrared. Above 3.1 eV, Ref. 43 reports data from Vehse and Arakawa [68] on a sample exposed to air that might not have been as clean as ours. In the infrared, differences between our impedance (Fig. 4.18) and that of Lenham and Treherne [52] are likely related to the lower scattering rate of single crystals compared to polycrystalline Ni. Losurdo *et al.* [57] report $\langle\epsilon_1\rangle$=−1.0 and $\langle\kappa\rangle$=2.1 at 4.2 eV. This compares well with our roughness-corrected results of ϵ=−1.4+9.6i (or κ=2.4).

4.5.2 Interband Transitions

The spin-polarized band structure of Ni, including Fermi surfaces, effective masses, and optical conductivity, has been discussed by Ehrenreich *et al.* [69] and by Wang and Callaway [70–72] as well as others [46, 73, 74]. Electronic states near the Fermi level are comprised

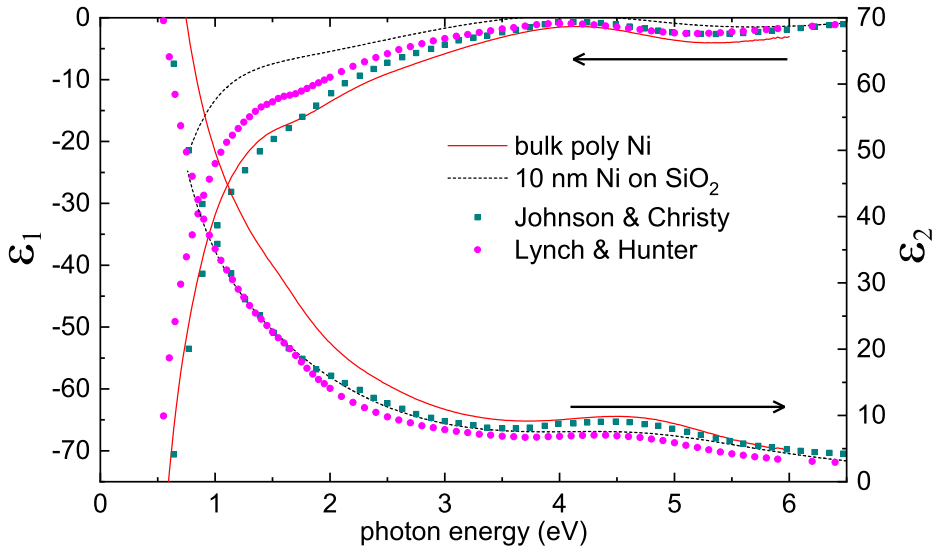

Figure 4.6: Comparison of the dielectric function of Ni from this work on bulk polycrystalline Ni (solid), a 10 nm thick Ni layer [46] on SiO_2 (dotted), from transmission and reflectance measurements of thin layers by Johnson and Christy [54] at 300 K, and as tabulated by Lynch and Hunter [43] (at 300 K above 3.1 eV and at 4 K below 3.0 eV).

of sp- and d-orbitals. Because of ferromagnetic ordering, there is a considerable exchange splitting [75] (about 0.5 eV) between the majority (spin-up) and minority spin (spin-down) d-orbitals. The spin-up band is completely full, while the spin-down d-orbital crosses the Fermi surface. Therefore, we expect d-intraband transitions at arbitrarily low energies, as well as interband transitions between sp- and d-orbitals.

Refs. 70 and 72 predict interband transitions at 0.3 eV (buried in the Drude background in our room-temperature data, but perhaps observable in low-temperature ellipsometry measurements), 0.8 eV (between parallel d-bands, related to the exchange splitting), at 2 or 2.5 eV, and between 5.1 and 5.5 eV (from the lower d-bands to the sp-bands above the Fermi energy). The latter peak can be lowered to 4.8 eV by self-energy corrections. Several regions in the Brillouin zone contribute to these transitions. Due to spin-orbit splitting, spin-flip interband transitions are weakly allowed [72].

An inspection of the ellipsometric angle ψ at low photon energies shows immediately that Ni is not a good Drude metal. ψ is related to the reflectivity R and ψ=45° is equivalent to R=1. In a Drude metal (compare gold in Fig. 4.19), ψ remains near 45° until the onset of interband transitions (near 2.5 eV for Au). In Ni, ψ drops nearly linearly from 44.3° at 0.06 eV to 35.1° at 1.3 eV (for an incidence angle of 70°). Therefore, intraband transitions occur at very low energies, as expected from the partially filled d-band.

It is difficult to quantify the interband transitions in our dielectric function (Fig. 4.3) because the Drude contribution is dominant at low energies. Therefore, we subtract the Drude contribution (70) from our multiband sum model (69) and plot the remaining interband contribution (71) in Fig. 4.13. The parameter correlations for our Drude-Lorentz model are below 0.9 (not as bad as it could be). Nevertheless, this subtraction method is somewhat arbitrary, because it depends on the number of oscillators and whether they are characterized as Drude or Lorentz oscillators. This was already pointed out by Ehrenreich *et al.* [69] Our best model in Table 4.1 has strong Lorentz peaks in ϵ_2 at 0.6, 1.5, and 4.7 eV and a shoulder at 2.5 eV. This is, of course, related to the Lorentzian resonance energies listed in Table 4.1. The sum of the Lorentzian amplitudes yields $\epsilon_\infty = \sum A_i$=15.5. A significant contribution to ϵ_∞ is from the lowest peak at 0.64 eV. The broadenings of the interband transitions are quite large, between 0.5 and 2.2 eV. The temperature dependence of interband transition energies and broadenings will be published elsewhere. In general, the agreement between our Drude-Lorentz model (69) and theory [70, 72] is excellent.

Our product model (72) also shows five interband transitions with energies and broadenings similar to the Drude-Lorentz model (69), but separating the Drude and interband contributions in the product model is not straightforward.

Lynch, Rosei, and Weaver [53] report several infrared peaks below 1 eV in their absorption (calorimetry) measurements at 4 K. These peaks are absent in our analysis, see Table 4.1, possibly because the free-carrier absorption in our results at 300 K overwhelms these interband transitions. Our results agree on interband transition peaks near 1.5 eV. Our peak at 2.6 eV was also found in ellipsometry measurements at 77 K by Stoll [76, 77], but we do not observe any fine structure due to spin-orbit splitting.

Johnson and Christy [54], Shiga and Pells [49] as well as Abdallah *et al.* [46] report a strong conductivity or ϵ_2 peak at 4.8 eV, which is also present in our data. As mentioned, it arises from transitions from the lower d-orbital to the sp-like bands. Shiga and Pells [49] report that the peak at 4.8 eV is a superposition of two peaks separated by an energy difference, which is proportional to spontaneous magnetization. This energy difference may be related to the exchange splitting. They show that the broadening of this peak has an anomalous temperature dependence, which decreases with increasing temperature. The width of our 4.8 eV peak is indeed quite large (2.1 eV), but we could not improve our fit with two separate contributions. We will revisit this topic when we report temperature-dependent ellipsometry results for Ni.

4.5.3 Free-Carrier Properties

The only Drude parameters reported previously for Ni that we are aware of are those of Lenham and Treherne [78] cited by Wang and Callaway [70]: n=6.5×10^{21} cm^{-3}, E_P=2.99 eV (assuming an optical mass m_0, the electron mass in vacuum), σ_0=186,000/Ωcm (18.6×10^{15}/s in Gaussian units), and τ=11.3 fs (Γ=58 meV). Lynch *et al.* [53] report a Drude scattering rate of Γ=20 eV at 4 K, which is unphysically large because of the anomalous skin effect [43].

However, their value of σ_0=658,000/Ωcm is quite reasonable at 4 K.

In the limit of high frequencies (but below the onset of interband transitions) and low scattering ($\omega\tau \gg 1$), the dielectric function of a Drude metal is approximated by

$$\epsilon_1(\omega) \approx \epsilon_\infty - \frac{\omega_P^2}{\omega^2} = \epsilon_\infty - \frac{E_P^2}{E^2}, \tag{74}$$

where ϵ_∞ is the high-frequency dielectric constant, i.e., the contribution to ϵ by bound charges. It is therefore customary [78–80] to plot ϵ_1 versus $1/E^2$, which yields ϵ_∞ as the intercept and E_P^2 as the slope. This technique was used by Lenham and Treherne [78] to find E_P=2.99 eV, from which they calculated the carrier density n=6.5×10^{21} cm^{-3} (assuming an optical mass of m_0). Our data and a linear interpolation are shown in Fig. 4.7 (a). Our linear regression to the data for $1/E^2 < 30$ (0.18 to 6.0 eV) finds a plasma frequency of 4.7 eV, which is consistent with one of the plasma frequencies found in our sum model, see Table 4.1. We also find an unphysical (negative) value of ϵ_∞=-5.4. We expect $\epsilon_\infty \approx$15, see Fig. 4.13. A linear fit over the entire spectral range from 0.06 to 6.0 eV finds a plasma frequency of 3.7 eV, which is similar to the energy of the main loss function peak, see Fig. 4.5. If we fit from 71 to 100 meV (our lowest-frequency data), we find E_P=3.4 eV. We see that this interpolation scheme only yields a rough estimate of the plasma frequency for one of the two carrier species.

To calculate the carrier density, we need to know the optical (effective) masses. Ehrenreich *et al.* [69] find an optical mass of 1.4 for s-electrons and 3.5 for d-electrons. If we associate the Drude term with small Γ = 42 meV (Drude 2) with s-electrons, then E_P = 4.86 eV results in an electron density of 24×10^{21} cm^{-3} (0.26 e/atom). Similarly, if the Drude 1 term with Γ = 2.87 eV and E_P=11.9 eV arises from d-electrons, then the carrier density is

359×10^{21} cm^{-3} (3.9 e/atom). We thus find a total density of about 4.2 e/atom from our optical measurements (assuming masses from Ref. onlineciteEhPh63), less than half of the expected density of 10 electrons per atom. Similarly, if we use effective masses calculated by Wang and Callaway [70], we overestimate e/atom.

In the same high-frequency limit ($\omega\tau \gg 1$), we also find

$$\epsilon_2(\omega) \approx \frac{\omega_P^2}{\omega^2} \times \frac{1}{\omega\tau} = \frac{E_P^2}{E^2}\frac{\Gamma}{E}. \tag{75}$$

One therefore plots [80] $\epsilon_2 E$ versus $1/E^2$, which should yield (for a Drude metal) a straight line through the origin with a slope of $E_P^2\Gamma$. If E_P is found from the plot of ϵ_1 versus $1/E^2$ (as discussed above), then one can calculate the scattering rate Γ. We apply this analysis method to our data in Fig. 4.7 (b) and find a slope of $E_P^2\Gamma$=0.82 eV^3, which agrees well with the results listed in Table 4.1, where we find $E_P^2\Gamma$=0.77 eV^3 for one species of carriers. The positive (non-zero) intercept of the $\epsilon_2 E$ versus $1/E^2$ graph can be explained with the contributions of bound carriers to ϵ_2 (interband transitions).

Without having to rely on the $\omega\tau \gg 1$ limit, the Drude model implies [61]

$$\epsilon_1(\omega) = 1 - \omega\tau\epsilon_2(\omega) = 1 - \frac{1}{\Gamma}\epsilon_2(E)\,E. \tag{76}$$

One therefore plots ϵ_1 versus $\epsilon_2 E$, which should yield $-1/\Gamma$ as the slope. Using this method, Lenham and Treherne [78] found Γ=58 meV, which compares well with our Drude 2 broadening in Table 4.1. As shown in Fig. 4.8, this graphical approach results in Γ=53 meV for our data. This value is larger than Γ=42 meV in Table 4.1 because of the discrepancy between the ellipsometry data and our Drude-Lorentz model in this energy range (compare the line and symbols in Fig. 4.8).

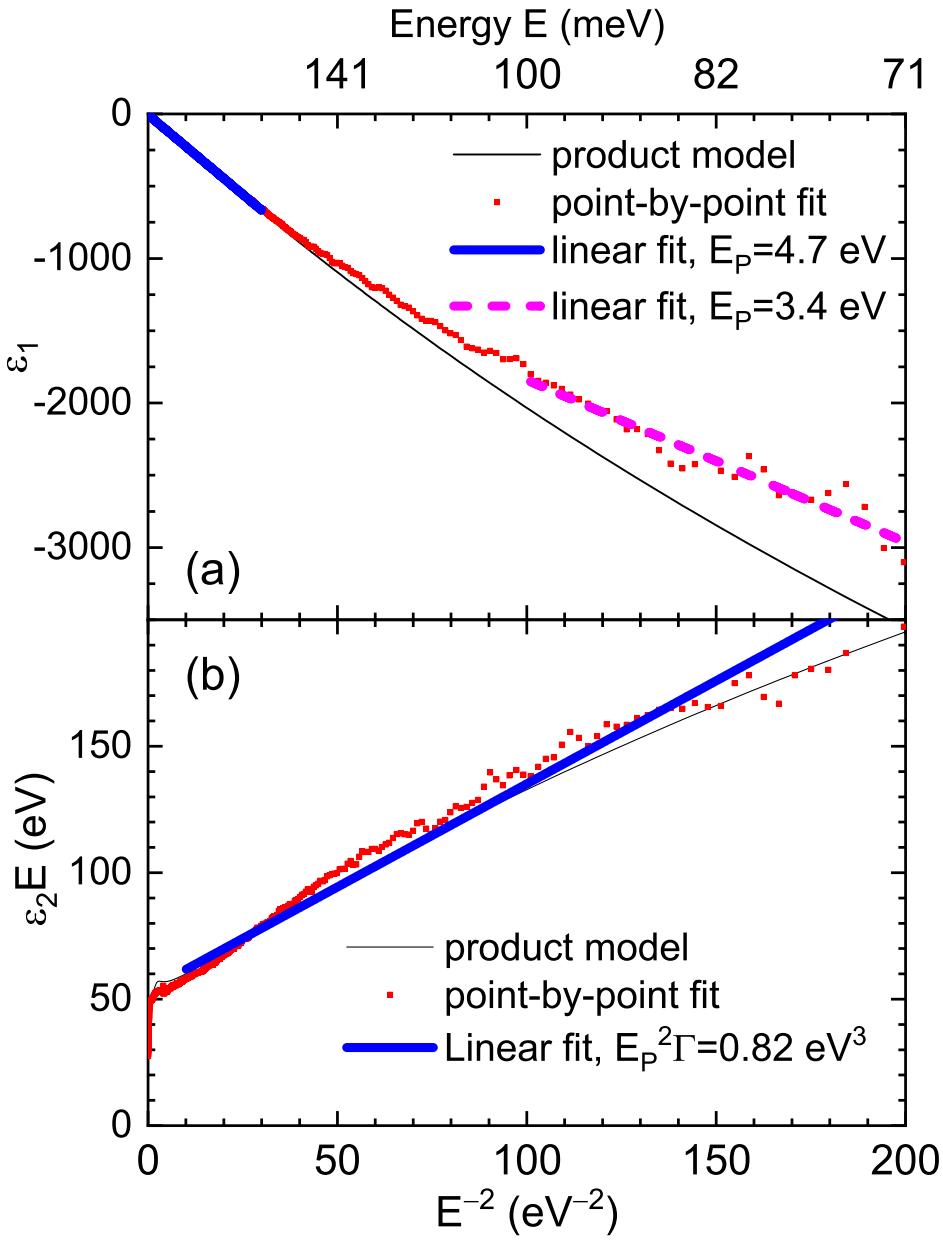

Figure 4.7: Drude parameters of polycrystalline Ni at 300 K extracted from the dielectric function in the high-frequency, low-scattering limit ($\omega\tau \gg 1$) using (a) Eq. (74) and (b) Eq. (75).

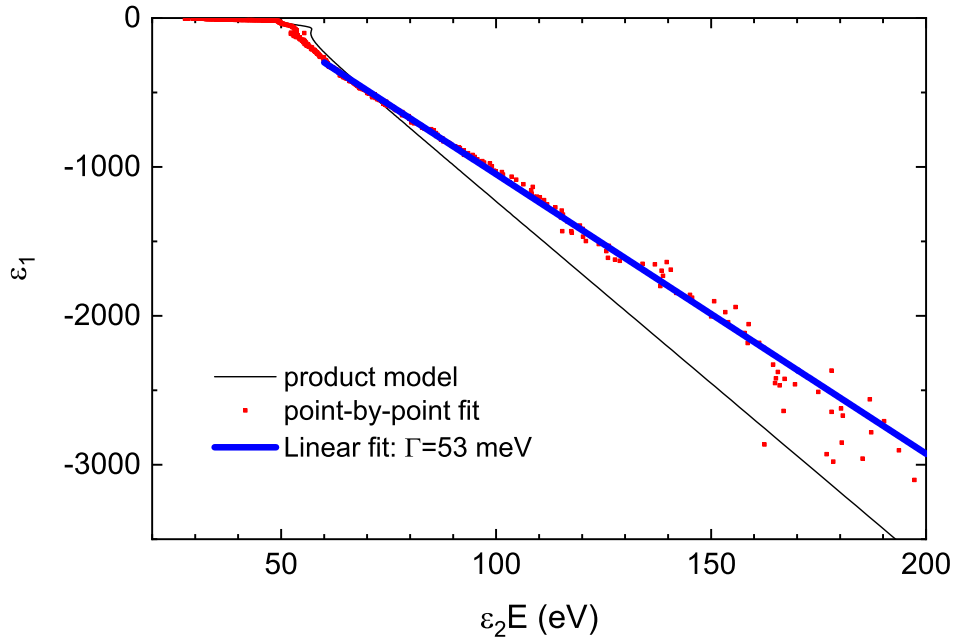

Figure 4.8: Drude parameters of polycrystalline Ni at 300 K extracted from the dielectric function using Eq. (76).

It has been argued that free-electron contributions to the optical constants of Ni are neglible [54, 80, 81], because intraband transitions between different partially filled d-orbitals are possible at arbitrarily low energies [43]. Nevertheless, our Drude-Lorentz model with two carrier species gives a remarkably good agreement with our near-infrared and visible optical constants of Ni. Since we use two free carrier species with different plasma frequencies and broadenings, there is a significant Drude contribution even at 6 eV, see Fig. 4.13. The usual graphical techniques [80], when applied to our infrared data, yield reasonable values for the plasma frequency and broadening without any modeling, but only for species of carriers with the smaller broadening. The other Drude contribution (with large broadening) has a strong overlap with visible and UV interband transitions and therefore can only be extracted by fitting the ellipsometric angles with a Drude-Lorentz lineshape.

4.5.4 Frequency Dependent Scattering Rate

Instead of modeling our experimental data with multiband sum or product lineshapes, we can also attribute the entire optical response to a single Drude term with frequency-dependent scattering rate, effective mass, and plasma frequency [62], as described in the supplementary material. Between 0 and 2 eV, we see a nearly threefold increase of the plasma frequency in Fig. 4.15. This can be explained as follows: at low energies, the Drude 2 term (E_P=4.86 eV and Γ=42 meV) dominates. At higher frequencies, the Drude 1 term with its larger broadening (E_P=11.9 eV, Γ=2.87 eV) becomes more important, roughly explaining the threefold increase in E_P. Above 2 eV, the frequency-dependent plasma frequency is dominated by interband transitions, leading to a large peak at 4.3 eV.

Similarly, the frequency-dependent renormalized scattering rate shown in Fig. 4.16 is small (about 50 meV) at low energies, dominated by the Drude 2 term. It increases nearly linearly (with a quadratic onset at very low energies) and flattens out above 1 eV at a value of 2.4 eV, similar to the scattering rate of the Drude 1 term.

4.6 Summary

We used thermal cleaning in UHV to prepare a nearly pristine poly-crystalline Ni surface. With *in situ* spectroscopic ellipsometry from 0.06 to 6.0 eV on two different instruments, we determined the ellipsometric angles and the optical constants of Ni, superseding 50 year-old literature data from various sources. Our data can be described well with a multiband Drude-Lorentz model. Parameters are listed and can be used to calculate reference dielectric functions for Ni. Our model separates contributions to the optical constants from free carriers

and interband transitions. We require two species of carriers (perhaps sp- and d-electrons) to describe our data, with very different plasma frequencies and scattering rates. Despite earlier claims to the contrary, graphical methods to extract free-carrier properties from the optical constants work quite well. We also find broad d-intraband transitions even at our lowest energies. At higher photon energies, several interband transitions take place, which agree well with previous studies.

Acknowledgements

This work was supported by the National Science Foundation (DMR-1505172), the European Union Structural and Investment Funds, and the Czech Ministry of Education, Youth, and Sports (CZ.02.2.69/0.0/0.0/16_027/0008215, Project IOP Researchers Mobility).

4.7 Supplementary Material

4.7.1 Optical Constants Anomaly of Ni Near the Curie Temperature

The optical pseudo-conductivity $< \sigma_1 >$ at 1.97 eV for three different Ni samples as a function of temperature is shown in Fig. 4.9, determined using spectroscopic ellipsometry at a 70° incidence angle. All data were acquired in UHV with a pressure below 10^{-8} Torr, to avoid surface contamination. During the first run (blue), the temperature of the sample was increased slowly from room temperature to 750 K. The heater was then turned down slowly and we measured $< \sigma_1 >$ as the sample cooled down to 400 K (run 2, green). We then turned the heater on again and heated the sample again to 750 K (run 3, black). Finally (run 4, red), we turned the heater down again and measured $< \sigma_1 >$ as the sample cooled down. Similar data for the pseudo-dielectric function of poly-crystalline Ni were reported

previously [56].

All Ni samples show an anomaly in the optical pseudo-conductivity at elevated temperatures, where there is a rapid rise of $< \sigma_1 >$. Since the temperature was measured with a thermocouple attached to the sample, it is difficult to obtain accurate temperature readings. Errors of up to 50 K are possible. Therefore, the temperature where the rise of $< \sigma_1 >$ occurs may or may not be the same for all samples, due to these errors.

The anomaly occurs only during the first heating of the sample past the Curie temperature. Since magnetic phase transitions (ferromagnetic to paramagnetic) should be reversible, it is not likely that the anomaly is due to magnetic effects. The anomaly could not be restored by removing the sample from the cryostat and placing into a saturating magnetic field of about 1 T. A partial restoration of the anomaly was possible by leaving the sample in humid air for several weeks. We therefore conclude that the anomaly is not due to magnetic effects as argued previously [56], but due to changes in surface conditions. We attribute the initial low-temperature pseudo-conductivity for each sample to different adsorbed surface layers (which were removed by the initial heating of the Ni sample). It was reported previously [46] that about 50 Å of water can be removed from the surface of thin Ni layers by heating in UHV. After heating, when adsorbed overlayers have evaporated, the final optical pseudo-conductivity is due to different surface roughness conditions (or other overlayers that cannot be removed by heating) or due to different bulk conduction mechanisms. For example, single-crystalline Ni is expected to be more conducting than cold-rolled poly-crystalline Ni.

We conclude that heating our Ni samples above the Curie temperature for about six hours is an effective way of preparing Ni surfaces for optical constants measurements. This cleaning

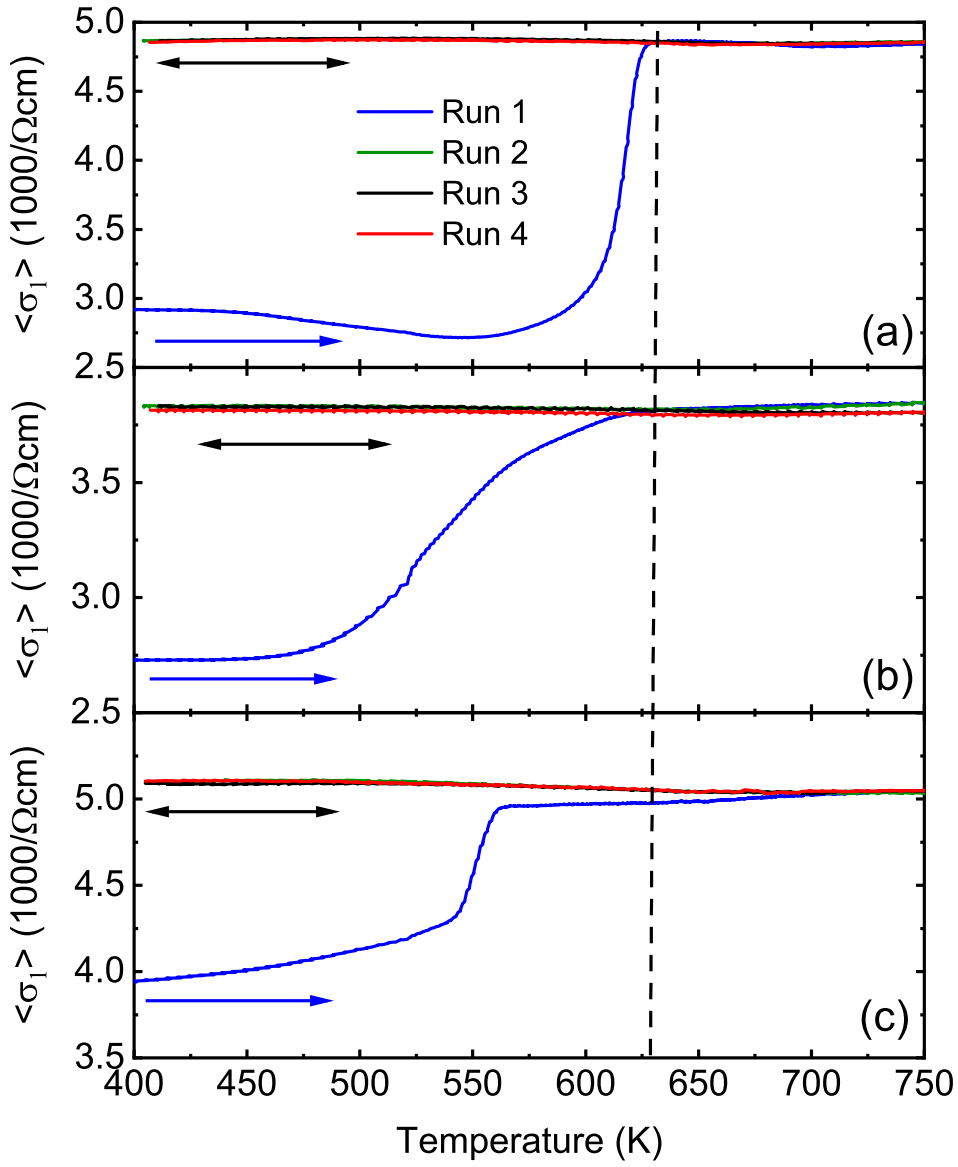

Figure 4.9: Optical pseudo-conductivity $< \sigma_1 >$ as a function of temperature, measured by ellipsometry in ultra-high vacuum at a single photon energy of 1.97 eV at an incidence angle of 70° for (a) a 1000 Å thick sputtered Ni layer on thick SiO_2 on Si, (b) a bulk poly-crystalline cold-rolled Ni substrate, (c) a single-crystalline Ni (001) substrate. The dashed vertical line shows the Curie temperature.

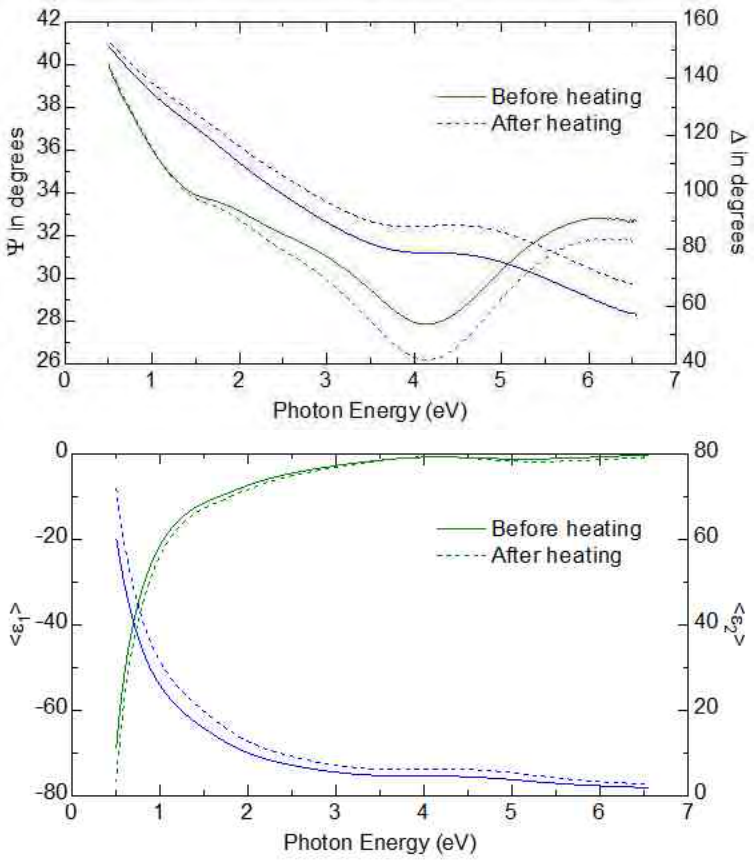

Figure 4.10: Ellipsometric angles ψ and Δ at 70° incidence angle (top) and pseudodielectric function (bottom) as a function of photon energy for a cold-rolled polycrystalline Ni substrate at room temperature, acquired in a UHV cryostat before (solid) and after (dashed) heating to 750 K for 6 hours. ψ and $< \epsilon_1 >$ are shown in green, Δ and in $< \epsilon_1 >$ blue.

procedure was therefore used for all ellipsometry measurements on Ni described in this work. To demonstrate the impact of cleaning, we show the room-temperature ellipsometric angles and the pseudo-dielectric function of cold-rolled pseudo-crystalline Ni in Fig. 4.10. The ellipsometric angle ψ decreases and Δ increases, as adsorbed layers are removed by heating, especially near the critical point at 4.8 eV. Changes in the ellipsometric angles are smaller in the near-infrared below 1 eV than in the UV. Similarly, $< \epsilon_1 >$ decreases and $< \epsilon_2 >$ increases after heating of the sample. The largest changes of $< \epsilon >$ are observed in the near-infrared spectral region.

In vacuum technology processing (for example in the semiconductor industry), heating of a wafer in vacuum is known as degassing. The experiments described in this section essentially monitor the degassing of Ni by *in situ* spectroscopic ellipsometry.

Similar changes in the ellipsometric angles and the pseudo-DF after heating in H_2 or exposure to O_2 have been reported by others [57] (Hanekamp 1983). Slow annealing of an amorphous as-sputtered Ni layer in H_2 promotes crystallization and desorption of surface layers [57]. This leads to a *decrease* of $\langle\epsilon_1\rangle$ by 1.4 and an increase in $\langle\kappa\rangle$ by 1.0 at 4.2 eV. (If the sample remains in H_2 too long at high temperatures, nickel hydrides may form, which deteriorates the pseudo-DF again.) In our annealing experiments, we find an *increase* of our polycrystalline bulk Ni samples of $\langle\epsilon_1\rangle$ by 0.2 and an increase in $\langle\kappa\rangle$ by 0.2 at 4.2 eV. This discrepancy of sign and magnitude can perhaps be explained by the fact that crystallization of an amorphous sputtered layer (associated with changes in position and broadening of the peak at 4.8 eV) and surface cleaning both contribute to the pseudo-DF. An energy of 4.2 eV may not be the best position for monitoring the cleanliness of a Ni surface. Hanekamp and van Silfhout (1983) show a decrease of Δ by about 1° at 1.97 eV after exposure to O_2,

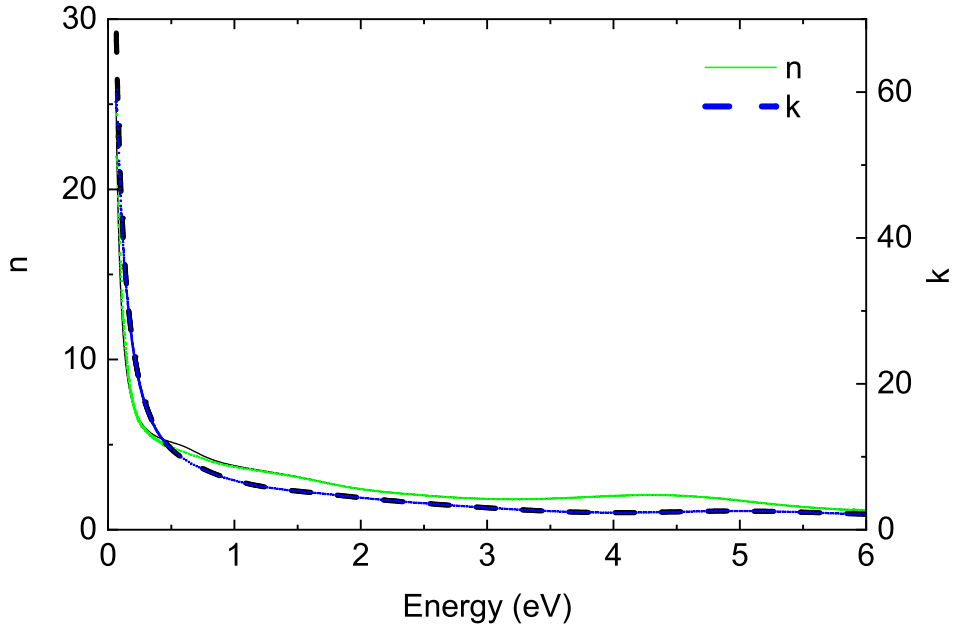

Figure 4.11: Complex refractive index of polycrystalline Ni at 300 K calculated from the data shown in Fig. 4.3. Symbols show results from a point-by-point fit, lines the results from the product model using Eq. (72).

significantly smaller than our observed change of 5° due to annealing.

4.7.2 Additional Experimental Data

The complex refractive index calculated from the dielectric function of polycrystalline Ni is shown in Fig. 4.11. The absorption coefficient and penetration depth are shown in Fig. 4.12, the infrared complex impedance in Fig. 4.18. Separate Drude and Lorentz contributions to the total dielectric function in the sum model (69) are shown in Fig. 4.13. A spreadsheet with experimental and sum model data (ψ, Δ, ϵ_1, ϵ_2, n, k) versus photon energy is also available as supplementary material.

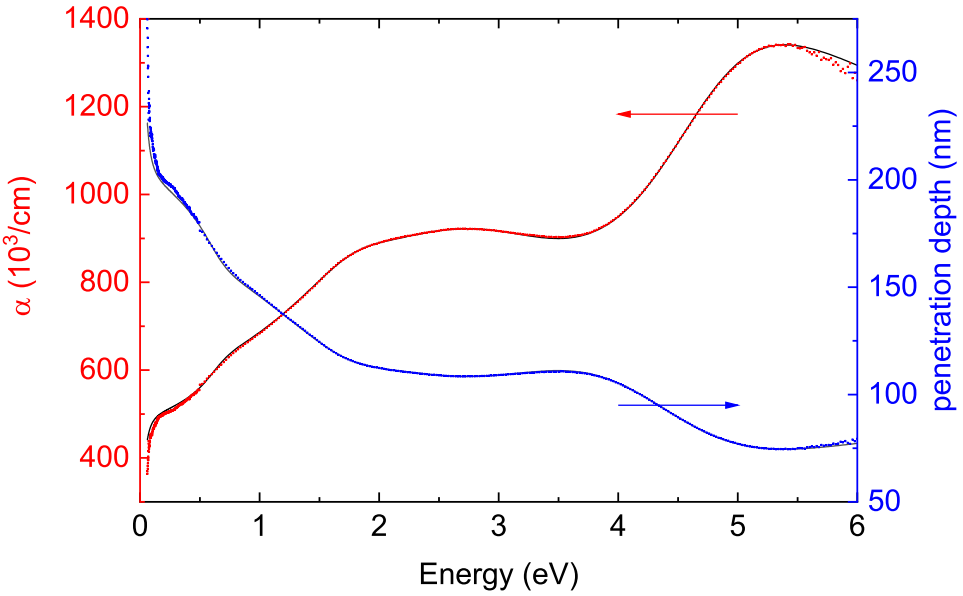

Figure 4.12: Absorption coefficient and penetration depth of polycrystalline Ni at 300 K calculated from the data shown in Fig. 4.3. Symbols show results from a point-by-point fit, lines the results from the product model using Eq. (72).

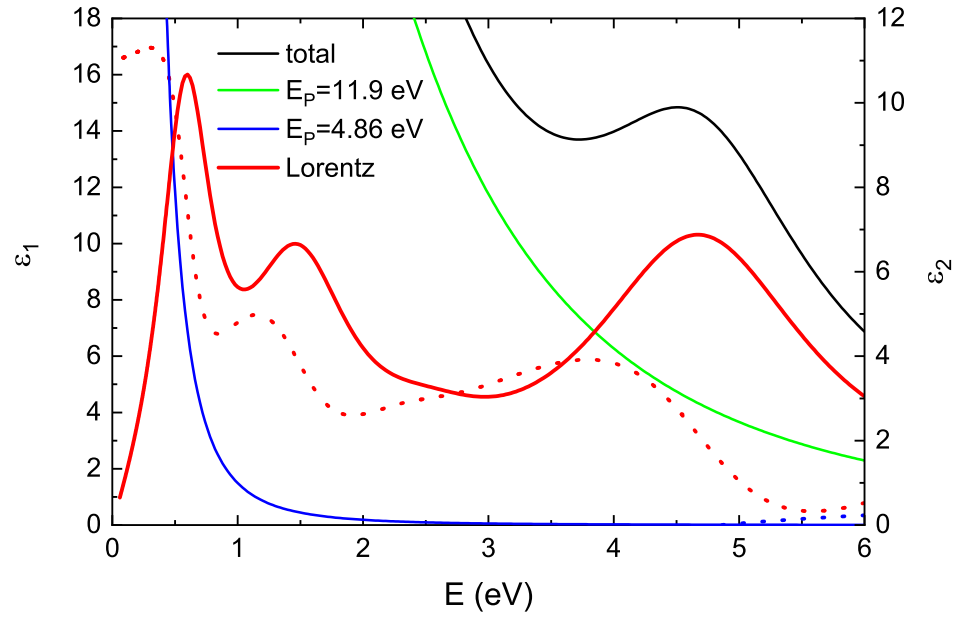

Figure 4.13: Real (dotted) and imaginary (solid) parts of the dielectric function of Ni at 300 K calculated from the sum model (69), but showing the total contribution (black) as well as the Drude (green, blue) and Lorentz (red) contributions separately.

4.7.3 Drude Model with Frequency Dependent Scattering Rate

A) Dielectric function

Within the Drude model (for a single species of free carriers), the dielectric function ϵ versus angular frequency ω is written as [14]

$$\epsilon(\omega) = 1 - \frac{\omega_P^2}{\omega^2 + i\gamma\omega} = 1 + i\frac{\omega_P^2}{\omega(\gamma - i\omega)}, \tag{77}$$

where

$$\omega_P^2 = \frac{ne^2}{\epsilon_0 m} \tag{78}$$

is the *unscreened* plasma frequency and γ the scattering rate, with the carrier density n, the effective mass m (sometimes called *bare optical band mass*) [61], electronic charge e, and the permittivity of vacuum ϵ_0. These equations assume that time-dependent fields vary like $e^{-i\omega t}$. Otherwise, all expressions in this section need to be replaced with their complex conjugates.

Some authors [61] add a high-frequency dielectric constant ϵ_∞ to the Drude expression (77) and introduce an associated screened plasma frequency [41]. We do not need this approach, because our models include explicit oscillators outside of our spectral range to consider the optical contribution from high-energy oscillators.

Written in real and imaginary components, Eq. (77) becomes

$$\epsilon(\omega) = \epsilon_1(\omega) + i\epsilon_2(\omega) = 1 - \tfrac{\omega_P^2}{\omega^2+\gamma^2} + i\tfrac{\omega_P^2}{\omega^2+\gamma^2} \times \tfrac{\gamma}{\omega}. \tag{79}$$

$$\epsilon_1(\omega) = 1 - \frac{\omega_P^2}{\omega^2 + \gamma^2} = 1 - \frac{\omega_P^2\tau^2}{1 + \omega^2\tau^2} \tag{80}$$

and

$$\epsilon_2(\omega) = \frac{\omega_P^2}{\omega^2 + \gamma^2} \times \frac{\gamma}{\omega} = [1 - \epsilon_1(\omega)] \times \frac{\gamma}{\omega} = \frac{\omega_P^2\tau^2}{1 + \omega^2\tau^2} \times \frac{1}{\omega\tau}, \tag{81}$$

where $\tau = 1/\gamma$ is the *unrenormalized* scattering time.

In the limit of high frequencies (but below the onset of optical interband transitions) and low scattering, $\omega\tau \gg 1$, we find

$$\epsilon_1(\omega) \approx 1 - \frac{\omega_P^2}{\omega^2} \quad \text{and} \quad \epsilon_2 \approx \frac{\omega_P^2}{\omega^2} \times \frac{1}{\omega\tau} \approx 0. \tag{82}$$

One can therefore plot $\epsilon_1(\omega)$ versus ω^{-2}, which yields $-\omega_P^2$ as the slope. Similarly, plotting $\epsilon(\omega)\omega$ versus ω^{-2} yields $\omega_P^2\gamma$ as the slope.

Sievers [61] writes the result (81) as

$$\frac{1}{\omega\tau} = \frac{\epsilon_2(\omega)}{1-\epsilon_1(\omega)} \quad or \quad \epsilon_1(\omega) = 1 - \tau\omega\epsilon_2(\omega). \tag{83}$$

Plotting $\epsilon_1(\omega)$ versus $\omega\epsilon_2(\omega)$ therefore yields the scattering time $-\tau$ as the slope.

B) Drude optical conductivity

The complex optical conductivity is defined as

$$\sigma(\omega) = -i\epsilon_0\omega[\epsilon(\omega) - 1] \tag{84}$$

or written in components as

$$\sigma(\omega) = \sigma_1(\omega) + i\sigma_2(\omega) \tag{85}$$

with

$$\sigma_1(\omega) = \epsilon_0\omega\epsilon_2(\omega) \quad \text{and} \quad \sigma_2(\omega) = \epsilon_0\omega[1 - \epsilon_1(\omega)]. \tag{86}$$

Sievers' result (83) for the Drude scattering rate can also be written in terms of the optical conductivity as

$$\frac{1}{\omega\tau} = \frac{\sigma_1(\omega)}{\sigma_2(\omega)}. \tag{87}$$

One can therefore determine the scattering rate directly at each frequency, if both real and imaginary parts of the optical conductivity are known, for example from an ellipsometry measurement.

Within the Drude model (77), the optical conductivity (84) becomes

$$\sigma(\omega) = \frac{\epsilon_0 \omega_P^2}{\gamma - i\omega} = \frac{\epsilon_0 \omega_P^2 \tau}{1 - i\omega\tau} = \frac{ne^2\tau}{m(1 - i\omega\tau)}. \tag{88}$$

This can be written in components as

$$\sigma_1 = \frac{\epsilon_0 \omega_P^2 \gamma}{\omega^2 + \gamma^2} = \frac{\epsilon_0 E_P^2 \Gamma}{\hbar(E^2 + \Gamma^2)}, \tag{89}$$

$$\sigma_2 = \frac{\epsilon_0 \omega_P^2 \omega}{\omega^2 + \gamma^2} = \frac{\epsilon_0 E_P^2 E}{\hbar(E^2 + \Gamma^2)}, \tag{90}$$

$$|\sigma|^2 = \frac{\epsilon_0^2 \omega_P^4}{\omega^2 + \gamma^2} = \frac{\epsilon_0^2 E_P^4}{\hbar^2(E^2 + \Gamma^2)}. \tag{91}$$

We note that

$$\sigma_1(\omega = 0) = \frac{\epsilon_0}{\hbar}\frac{E_P^2}{\Gamma} = \sigma_0 \quad \text{and} \quad \sigma_2(\omega = 0) = 0. \tag{92}$$

The real and imaginary parts σ become equal at ω=γ.

Figure 4.14 shows the real and imaginary parts of the optical conductivity calculated from two sets of parameters similar to those labeled Drude1 and Drude2 in Table 4.1. We calculate σ_0=6640/Ωcm for Drude1 and σ_0=75,500/Ωcm for Drude2. We therefore associate the Drude1 term with d-electrons (because of their large scattering rate) and the Drude2 term with sp-electrons (because of their dominant contribution to the DC conductivity, see Mott 1936). The total conductivity calculated from our optical data is 82,100/Ωcm, which is lower than, but of the same order of magnitude as the commonly cited electric conductivity of Ni of 146,000/Ωcm. σ_2 indeed becomes 0 at low frequencies for the Drude1 term, but we cannot observe this for the Drude2 term because we did not measure at sufficiently low

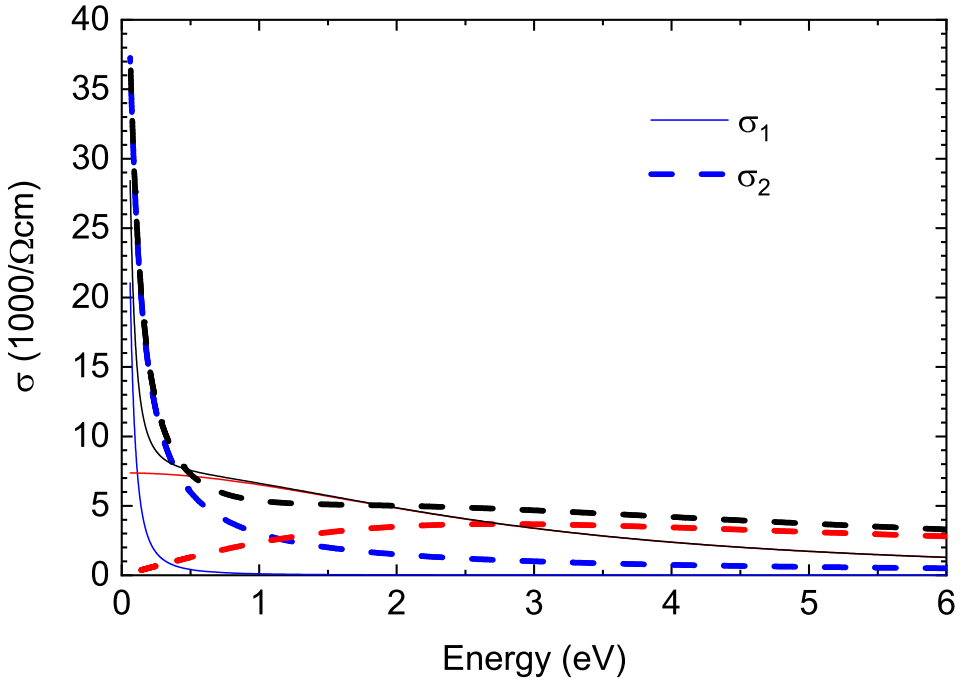

Figure 4.14: Real (solid) and imaginary (dashed) parts of the optical conductivity calculated from the Drude model, see Eqs. (89) and (90). Drude1 (red): E_P=12.3 eV, Γ=2.76 eV; Drude2 (blue): E_P=4.73 eV, Γ=34.6 meV. The black line shows the sum of both contributions.

energies (below Γ=42.1 meV).

There is a crossing of σ_1 and σ_2 at Γ=2.76 eV for the Drude1 term. This crossing is below our spectral range for the Drude2 term. At the lowest frequencies, the Drude2 term is the dominant contribution to σ_1, while the Drude1 term dominates above 1 eV.

Equation (88) implies

$$\tau^{-1} = \gamma = \frac{\epsilon_0 \omega_P^2}{\sigma} + i\omega = \frac{\epsilon_0 E_P^2 \sigma_1}{\hbar^2 |\sigma|^2} + i\left(\omega - \frac{\epsilon_0 E_P^2 \sigma_2}{\hbar^2 |\sigma|^2}\right) \tag{93}$$

$$\tau^{-1} = \gamma = \frac{\epsilon_0 \omega_P^2 \sigma_1}{|\sigma|^2} + i\omega\left(1 - \frac{\epsilon_0 \omega_P^2 \sigma_2}{\omega |\sigma|^2}\right), \tag{94}$$

where we have introduced $E_P = \hbar\omega_P$. We also note that $\epsilon_0/\hbar$=134.52 1/ΩcmeV and $\hbar^2 e^2/\epsilon_0 m_0$=1.379×10^{-21} cm^{3}eV^2. In Gaussian units, 1/Ωcm is equivalent to 10^{-11}/s. Equation (94) allows us to calculate the unrenormalized scattering rate from the measured optical

conductivity, if we "guess" the plasma frequency or determine it from other sources.

4.7.4 Renormalized Frequency Dependent Scattering Rate, Plasma Frequency, and Effective Mass

Following Sulewski *et al.* [62], we define in MKSA units

$$\Gamma_1(\omega) = \frac{\epsilon_0 E_P^2 \sigma_1}{\hbar |\sigma|^2}, \tag{95}$$

$$1 + \lambda(\omega) = \frac{\epsilon_0 E_P^2 \sigma_2}{\hbar E |\sigma|^2}, \tag{96}$$

$$\hbar\gamma^*(\omega) = \frac{\hbar}{\tau^*(\omega)} = \frac{\Gamma_1(\omega)}{1 + \lambda(\omega)}, \tag{97}$$

$$\omega_P^{*2}(\omega) = \frac{\omega_P^2}{1 + \lambda(\omega)}, \quad \text{and} \tag{98}$$

$$m^*(\omega) = m[1 + \lambda(\omega)], \tag{99}$$

which makes Eq. (94) equivalent to

$$\hbar\tau^{-1} = \hbar\gamma = \Gamma_1(\omega) - iE\lambda(\omega). \tag{100}$$

Sievers [61] writes Eq. (98) in terms of the dielectric function $\epsilon(\omega)$ as

$$\frac{E_P^{*2}(\omega)}{E^2} = \frac{\epsilon_2^2(\omega) + [1 - \epsilon_1(\omega)]^2}{1 - \epsilon_1(\omega)} \tag{101}$$

which is, of course, equivalent.

The unstarred quantities τ, γ, ω_P, and m are the *unrenormalized* scattering time, scattering rate, plasma frequency and the *bare optical band* mass. The equivalent quantities with the asterisk are called the frequency-dependent *renormalized* quantities. m^* is also called the infrared (experimental) mass [61], if it is calculated using Eq. (99) from the measured optical conductivity. The quantity $1 + \lambda(\omega)$ is the frequency-dependent *mass enhancement factor*. We have defined Γ_1 in units of energy with an $\hbar$ prefactor. All equations are in MKSA units.

If the optical conductivity $\sigma(\omega)$ follows the Drude model, then it is easy to see from Eq. (87) that

$$\gamma^*(\omega) = \frac{1}{\tau^*(\omega)} = \frac{\sigma_1}{\sigma_2}\omega = \frac{1}{\tau} \tag{102}$$

and $1 + \lambda(\omega) = 1$. Therefore, the renormalized plasma frequency is equal to the unrenormalized plasma frequency and the renormalized mass is equal to the bare optical band mass.

It gets more interesting, if the optical conductivity does not show pure Drude behavior, for example because the (classical) frictional force is not proportional to the velocity (which was one of the assumptions in deriving the Drude and Lorentz models). In a quasi-particle picture, free electrons might interact with other excitations (phonons or interband transitions or surface plasmons [61]), which causes deviations of the optical conductivity from the pure Drude response. This is sometimes called the Holstein (1954, 1964) effect. In such cases, we can still calculate the renormalized frequency-dependent scattering rate, because the plasma frequency cancels in Eq. (97). We can only calculate the renormalized frequency-dependent mass, if the plasma frequency is known (at least approximately). Sometimes, we will guess a value of the plasma frequency in this calculation. An error introduced by an incorrect plasma frequency will only cause a constant factor in the renormalized mass m^*.

4.7.5 Application to Drude Model with Two Carrier Species

While the frequency-dependent scattering formalism has been applied to a variety of materials [61–67], especially alkali metals, heavy Fermion compounds, and conducting metal oxides, we are not aware of an application of this concept to a dielectric function determined by two species of free carriers. Drude (1900) already speculated that metals required two different species of free charge carriers to explain their optical constants. This topic was

revisited by Roberts (1955, 1959) and applied to Ni.

For a single Drude carrier species, the mass enhancement factor equals unity, as already mentioned. The dotted line in Fig. 4.15 (a) shows the mass enhancement factor calculated with Eq. (96) from an optical conductivy written as a sum of two free carrier terms [41] given in Eq. (88). This calculation requires choosing a fixed value of the plasma frequency, so we picked E_P=4.73 eV similar to Table 4.1. At first, it seems strange that the renormalized mass parameter would drop from 80% of the bare mass to 13% as the photon energy increases. Since the free carrier absorption is dominated by s-electrons (with a small mass) at low energies and by d-electrons (with a large mass) at high energies, the opposite should be the case. The key to understand this graph is to consider that we used a fixed plasma energy of E_P=4.73 eV in this calculation.

It is more helpful to plot the energy dependence of the inverse mass enhancement factor, see the dotted line in Fig. 4.15 (b). This equals the square of the ratio of the energy-dependent plasma frequency to our assumed value of E_P=4.73 eV. For low photon energies, free carrier absorption is dominated by the sp-electrons (term Drude2) with a plasma frequency of E_P=4.73 eV, equal to our assumed value. Therefore, the inverse mass enhacement factor is about 1. As the photon energy increases, the contribution to the free carrier absorption by the sp-electrons decreases and the contribution of the d-electrons (Drude1 term) with a plasma frequency of 12.3 eV increases. We therefore expect the inverse mass enhancement factor to reach 6.8 at very high energies, which is close to the value of 7.6 at 6 eV, see Fig. 4.15 (b). The plasma frequency (78) ω_P^2=$ne^2/\epsilon_0 m$ is determined by the ratio of two parameters, the carrier density and the effective mass. While we expect the effective mass to be larger for d-electrons than for sp-electrons (which tends to decrease the plasma frequency), the carrier

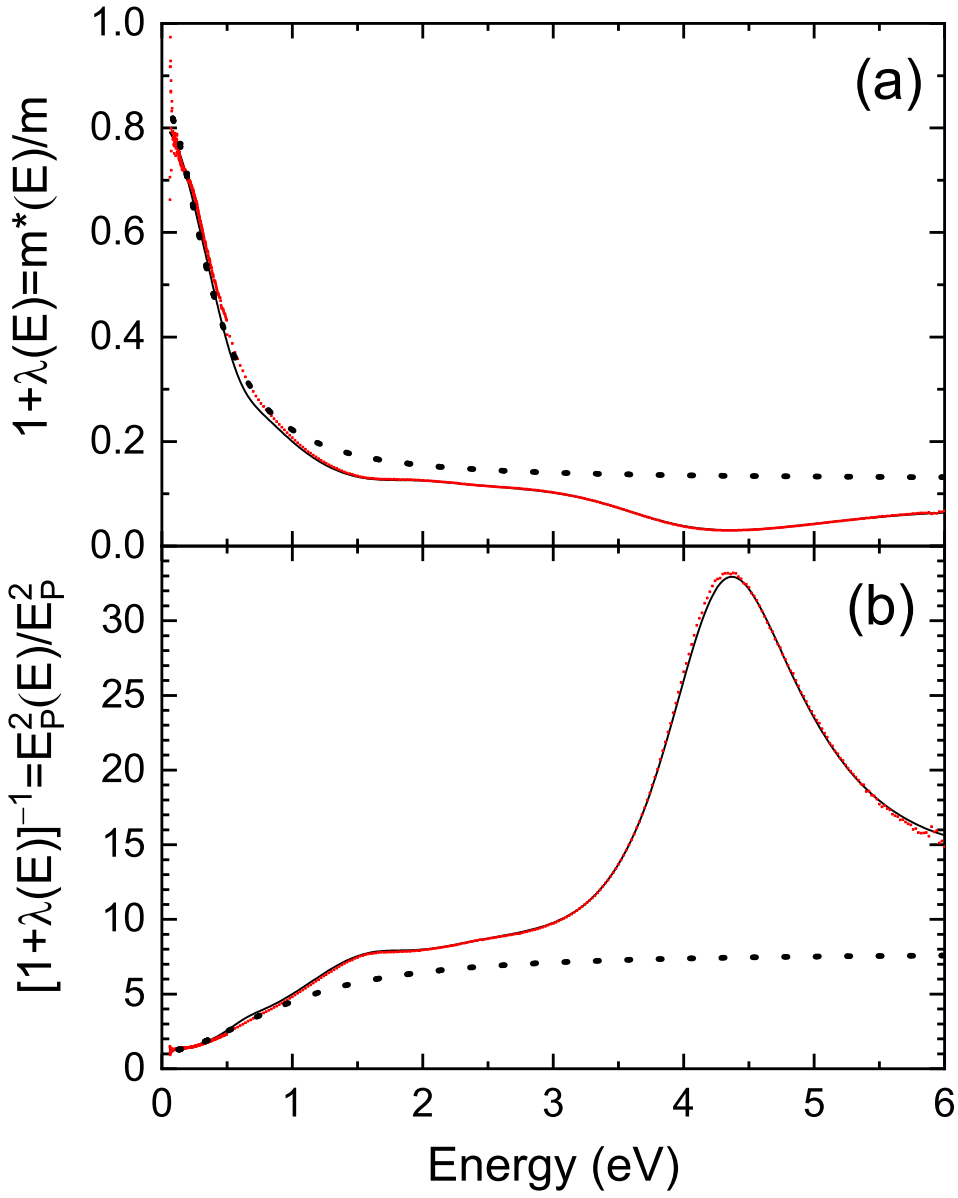

Figure 4.15: Mass enhancement factor $1 + \lambda(E)$ (a) and its inverse (b) as a function of photon energy, calculated from Eq. (96). The dotted line shows results calculated from a Drude model with two carrier species as shown in Fig. 4.14. The symbols and solid lines show results calculated from our experimental data and our product model, respectively. We assumed a value of E_P=4.73 eV for the plasma frequency in this figure.

density increases even more than the effective mass and therefore the plasma frequency for d-electrons is larger than for sp-electrons,

We now understand why $m^*(E)$ decreases with photon energy. m^* is close to unity at low frequencies, because we have chosen the correct plasma frequency of sp-electrons (4.73 eV) in this frequency range. At higher energies (above 1 eV), the contribution from d-electrons with a plasma frequency of 12.3 eV dominates. The effective mass parameter therefore decreases, because we have chosen a plasma frequency which is much too low for the spectral range above 1 eV. (The same decrease of m^* with increasing energy would occur, if we had chosen E_P=12.3 eV in our calculation, but it would reach a high-energy limit of unity.)

In summary, it is our impression that a frequency-dependent mass parameter is not a useful concept in the description of the optical constants of a free electron gas with two types of carrier with different densities and optical band masses. Instead, it is more intuitive to consider the frequency dependence of the renormalized plasma frequency, see Fig. 4.15 (b).

The frequency-dependent renormalized scattering rate $\hbar/\tau^*$ calculated from a sum of two Drude terms with parameters in Table 4.1 is shown in Fig. 4.16 (dotted). At low energies, $\hbar/\tau^*$ equals 0.05 eV, because most of the scattering is due to sp-electrons with a scattering rate of 0.0421 eV. Only a small contribution to the scattering rate is due to d-electrons (and therefore the total value of $\hbar/\tau^*$ slightly larger than 0.0421 eV). As the photon energy increases and scattering of d-electrons becomes dominant, $\hbar/\tau^*$ increases also, first quadratically and then linearly. The increase flattens out above 1 eV and $\hbar/\tau^*$ approaches 2.4 eV at an energy of 2 eV, close to the Drude1 scattering rate of d-electrons shown in Table 4.1.

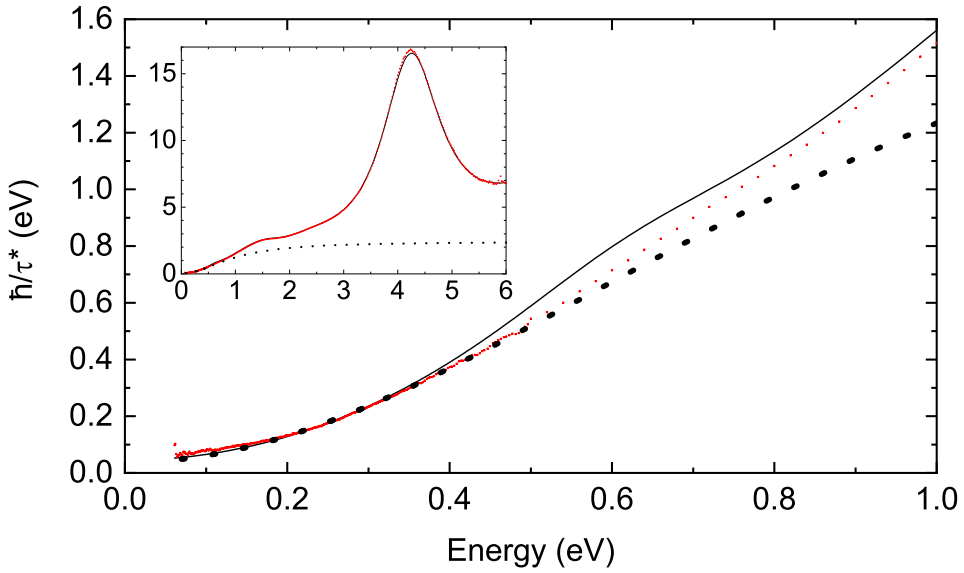

Figure 4.16: Frequency-dependent scattering rate as a function of photon energy, calculated from Eq. (97). The dotted line shows results calculated from a Drude model with two carrier species as shown in Fig. 4.14. The symbols and solid lines show results calculated from our experimental data and our product model, respectively.

4.7.6 Impedance and Refractive Index

Faraday's Law (the third Maxwell equation) for electromagnetic waves in vacuum reads in MKSA units

$$\vec{\nabla} \times \vec{E} = -\mu_0 \frac{\partial \vec{H}}{\partial t}, \tag{103}$$

where $\vec{E}$ and $\vec{H}$ are the electric and magnetic field strengths and μ_0 the permeability of free space. For a plane wave with wave vector $\vec{k}$ and angular frequency ω, this becomes

$$\vec{k} \times \vec{E}_0 = \omega \mu_0 \vec{H}_0, \tag{104}$$

where the subscript 0 stands for the complex amplitude of the plane wave. We can eliminate $\vec{k}$ with the wave equation

$$\vec{\nabla}^2 \vec{E} - \frac{1}{c^2} \frac{\partial^2 \vec{E}}{\partial t^2} = 0 \tag{105}$$

and the resulting dispersion equation

$$k^2 = \frac{\omega^2}{c^2}. \tag{106}$$

From Eqs. (104) and (106), we find the relationship

$$E_0 = \mu_0 c H_0 = \sqrt{\frac{\mu_0}{\epsilon_0}} H_0 = Z_0 H_0 \tag{107}$$

between the magnitudes of the electric and magnetic field strength amplitudes, where we have introduced the speed of light in vacuum

$$c = \frac{1}{\sqrt{\epsilon_0 \mu_0}} \tag{108}$$

and the impedance of vacuum

$$Z_0 = \sqrt{\frac{\mu_0}{\epsilon_0}} = 377\ \Omega. \tag{109}$$

The corresponding Maxwell equation (Faraday's Law) in a dispersive medium (e.g., a metal) is

$$\vec{\nabla} \times \vec{E} = -\frac{\partial \vec{B}}{\partial t}, \tag{110}$$

where $\vec{B} = \mu \mu_0 \vec{H}$ is the magnetic flux density, or

$$\vec{k} \times \vec{E}_0 = \omega \vec{B}_0 = \omega \mu \mu_0 \vec{H}_0 \tag{111}$$

for plane waves. At optical frequencies, μ=1. In an anisotropic medium, we no longer have a wave equation similar to Eq. (105) (because $\vec{E}$ is not in general perpendicular to the wave vector). We therefore restrict the following discussions to isotropic media.

The wave equation

$$\vec{\nabla}^2 \vec{E} - \frac{1}{c^2} \frac{\partial^2 \epsilon \vec{E}}{\partial t^2} = 0 \tag{112}$$

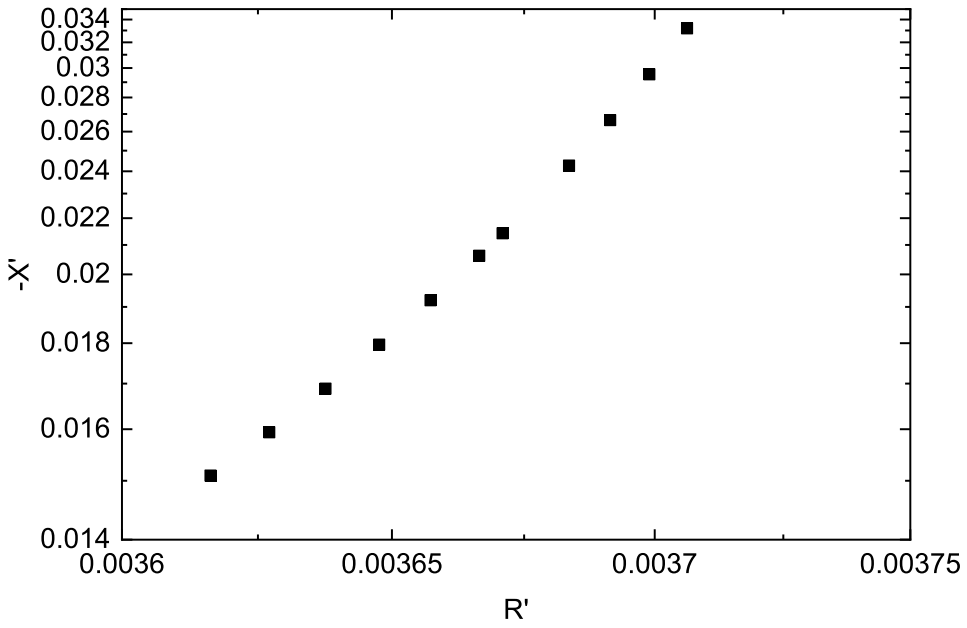

Figure 4.17: Lenham-Treherne diagram [51] for the complex impedance (in units of Z_0) at selected wavelengths between 8 and 17 μm calculated from a Drude dielectric function with E_P=4.7 eV and a Drude broadening Γ=35 meV. Note the reciprocal axes.

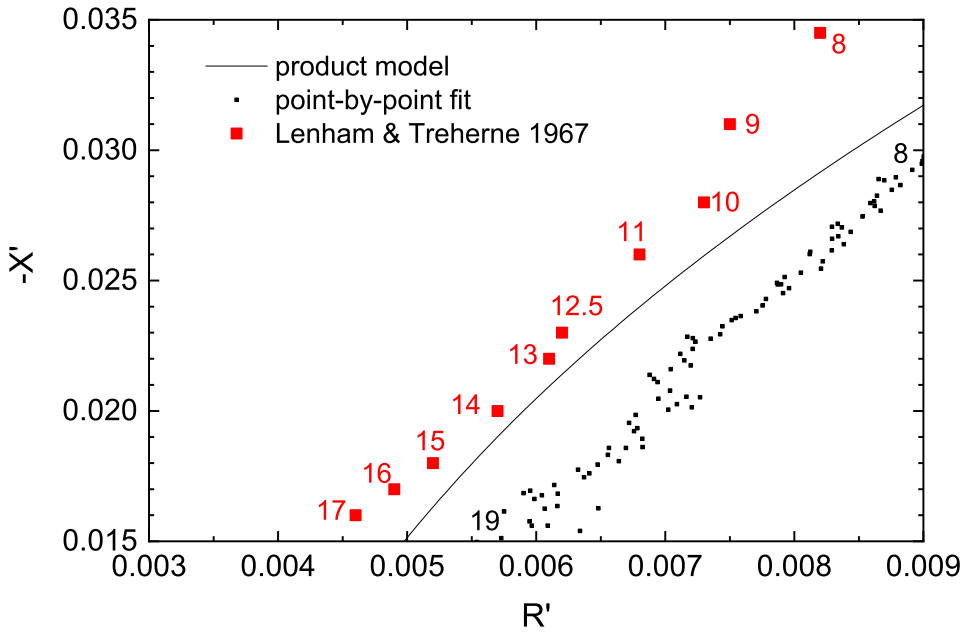

Figure 4.18: Argand diagram of the complex optical impedance (in units of Z_0) defined in Eqs. (117) and (118) calculated from the complex dielectric function shown in Fig. 4.3 for polycrystalline Ni at 300 K. Note the linear axes. Small symbols show results from a point-by-point fit. The line was calculated from the product model (72) with parameters in Table 4.2. Large symbols show the results of Lenham and Treherne on Ni single crystals from 8 to 17 μm wavelength [52], indicated by numbers.

for an isotropic medium with μ=1 results in the dispersion relation

$$|k|^2 = \epsilon \frac{\omega^2}{c^2} \tag{113}$$

for a generalized (or inhomogeneous) plane wave with a complex wave vector $\vec{k}$ and real angular frequency ω (Mansuripour 1995, Stratton 2007). From Eqs. (111) and (113), we find the relationship

$$\sqrt{\epsilon} E_0 = \mu_0 c H_0 = \sqrt{\frac{\mu_0}{\epsilon_0}} H_0 = Z_0 H_0 \tag{114}$$

between the magnitudes of the amplitudes of the electric and magnetic field strengths. This is similar to Eq. (107) except for a factor $\sqrt{\epsilon}$, where ϵ is the frequency-dependent dielectric constant. This results in

$$E_0 = \frac{Z_0}{\sqrt{\epsilon}} H_0 = Z H_0, \tag{115}$$

where $Z = Z_0/\sqrt{\epsilon} = R + iX$ is the complex impedance of the wave in an isotropic medium with μ=1. R and X are the real part (resistance) and imaginary part (reactance) of the complex impedance [52]. It is convenient to introduce the dimensionless complex impedance [52]

$$Z' = R' + iX' = \frac{Z}{Z_0} = \frac{1}{\sqrt{\epsilon}} = \frac{1}{n + i\kappa} \tag{116}$$

with real part

$$R' = \frac{n}{n^2 + \kappa^2} \tag{117}$$

and imaginary part

$$X' = \frac{-\kappa}{n^2 + \kappa^2}. \tag{118}$$

The older literature [52] sometimes includes a factor of $4\pi/c$, which arises from the definition of the surface impedance of a conductor (Dingle 1953, Jackson 1975) in Gaussian units. This

does not affect the definition of the dimensionless impedance Z' in Eq. (116). Our results are therefore directly comparable to those of Lenham and Treherne [52].

It was customary in the older literature [52] to plot X' (reactance) versus R' (resistance), in units of Z_0, sometimes with reciprocal axes [51]. It is not possible to write the complex refractive index with real part (Fox 2010)

$$n = \frac{1}{\sqrt{2}}\sqrt{\epsilon_1 + \sqrt{\epsilon_1^2 + \epsilon_2^2}} \tag{119}$$

and imaginary part

$$\kappa = \frac{1}{\sqrt{2}}\sqrt{-\epsilon_1 + \sqrt{\epsilon_1^2 + \epsilon_2^2}} \tag{120}$$

for free-carrier absorption with simple equations, without approximations that are too restrictive ($\omega\tau \gg 1$) for our purposes. We therefore show $-X'$ versus R' with reciprocal axes for a Drude metal with plasma frequency 4.7 eV (carrier density n=1.6×10^{22} cm^{-3}) and a Drude broadening of 35 meV, which corresponds to a scattering time τ=19 fs (similar to Ni, see Table 4.1) in Fig. 4.17. The negative sign in $-X'$ is due to our convention $\exp(-\omega t)$ for the time-varying fields. This figure is similar to Fig. 1 in Ref. 51.

From our dielectric function for polycrystalline Ni at 300 K (determined from a point-by-point fit and from our product model), we can calculate the complex impedance. The results are shown in Fig. 4.18. As mentioned by Lenham and Treherne [51], an Argand diagram for the complex impedance is much more sensitive to show small differences between data and a model than the dielectric function (Fig. 4.3) or the complex optical conductivity (Fig. 4.4). We compare our results with those measured by Lenham and Treherne [52] in Fig. 4.18. The agreement between our data and theirs is about the same as the agreement between our data and our product model. A horizontal shift of the Argand impedance curve towards smaller R'

values indicates a larger scattering time [51]. In other words, the resistance in the Lenham-Treherne single crystals [52] should be expected to be smaller than in our polycrystalline Ni samples.

4.7.7 Anomalous Skin Effect

The anomalous skin effect [43] (Dingle 1953, Wooten 1972, Jones 1972) affects the optical response of metal surfaces when the electron mean free path l=$v_F\tau$ (where v_F is the Fermi velocity) becomes of the order of the penetration depth or larger. We calculate l=16 nm from v_F=10^8 cm/s, see Ref. 69, and τ=$\hbar/\Gamma$=16 fs (Table 4.1). Our penetration depths are at least 75 nm, i.e., much larger than the electron mean free path, see Fig. 4.12. We therefore do not take the anomalous skin effect into account in the analysis of our room temperature data. (We were unable to confirm the value of v_F given by Kamineni *et al.* [9] in the sources they cited.)

According to Lynch and Hunter [43], the anomalous skin effect correction to the normal-incidence reflectance is $\frac{3}{4}\frac{v_F}{c}$ for diffuse surface scattering, which equals 0.0025 for Ni.

The question about the anomalous skin effect contributions to ellipsometry data should be revisited with low-temperature measurements of a high-conductivity metal like Au or Al.

Brückner *et al.* (1989) write that the complex refractive index must sometimes be modified due to the anomalous skin effect. An ellipsometry or reflectance experiment measures an effective complex refractive index $n^* + i\kappa^*$, which is related to the Drude-Lorentz refractive index $n + i\kappa$ by

$$\frac{n^* + i\kappa^*}{n + i\kappa} = 1 - \frac{3v_F}{16c}\frac{\kappa - in}{-i + (1/\omega\tau)}. \tag{121}$$

Shelton *et al.* (2008) take the viewpoint that the free carrier concentration n in the Drude

model must be replaced with a frequency-dependent carrier concentration

$$n^*(\omega) = \frac{n}{\tau}\frac{\beta^{2/3}}{v_F^{2/3}}\sqrt[3]{\frac{2m}{\omega n e^2 \mu_0}}. \tag{122}$$

The dimensionless parameter β is related to the surface roughness and describes if scattering of electrons by the surface is specular or diffuse.

4.7.8 Zeros and Poles on the Imaginary Axis

It is well known [40,41] (Berreman 1968) that the dielectric function of a solid can be written as a product (72) with zeros and poles in the complex plane. In the case of infrared lattice absorption, the poles represent the transverse optical phonons and the zeros the longitudinal optical phonons. For electronic transitions, the poles represent the energy gap (resonance frequency) and the zeros the strengths of the transitions [41]. For a metal, the free carrier absorption is described by a pole on the imaginary axis, where the associated zero (which represents the plasma frequency) is not on the imaginary axis.

We struggled for some time with how to model the dielectric function of a metal using Eq. (72) if the free carrier absorption is described by two species of carriers. We solved this problem numerically and found an equivalent description of the dielectric function as a sum or a product of Drude oscillators with parameters listed in Table 4.3. The results are somewhat surprising and warrant some discussion. We find that the Drude parameters of the term with the larger plasma frequency (Drude 1) are comparable in both models. The broadenings are identical and the plasma frequency differs by only 10%. The broadenings of the second Drude term are also identical. It is surprising, however, that the zero of the second Drude term is on the imaginary axis. This is the first time we have encountered the

Table 4.3: The optical constants of a metal calculated from a sum of two Drude terms in Eq. (69) (top part) were fitted with a product of two Drude terms as in Eq. (72) (bottom part).

	$\hbar\omega_P$ (eV)	$\hbar\gamma$ (eV)
Drude 1	11.9	2.87
Drude 2	4.86	0.0421

	$\hbar\omega_0$ (eV)	$\hbar\gamma_0$ (eV)	$\hbar\omega_L$ (eV)	$\hbar\gamma_L$ (eV)
Drude 1	0	2.87	12.8	2.46
Drude 2	0	0.0422	0	0.450

need for a zero of the dielectric function on the imaginary axis.

4.7.9 Optical Constants of Gold

A) Ellipsometric angles and model parameters

For comparison with Ni, we also measured the ellipsometric angles for gold using the same instruments, but in air with angles of incidence from 65° to 80° with 5° steps. The gold layer used for these measurements was a calibration standard (gold mirror) shipped with the FTIR ellipsometer by the J. A. Woollam Company. This gold layer was not cleaned (by heating in UHV) and measured in air. Therefore, this sample was probably not clean, but covered with surface layers. Therefore, we consider the optical constants reported here a qualitative estimate. They do not carry the same accuracy as our Ni data. The main reason for reporting optical constants of gold in this context is to have a qualitative comparison of

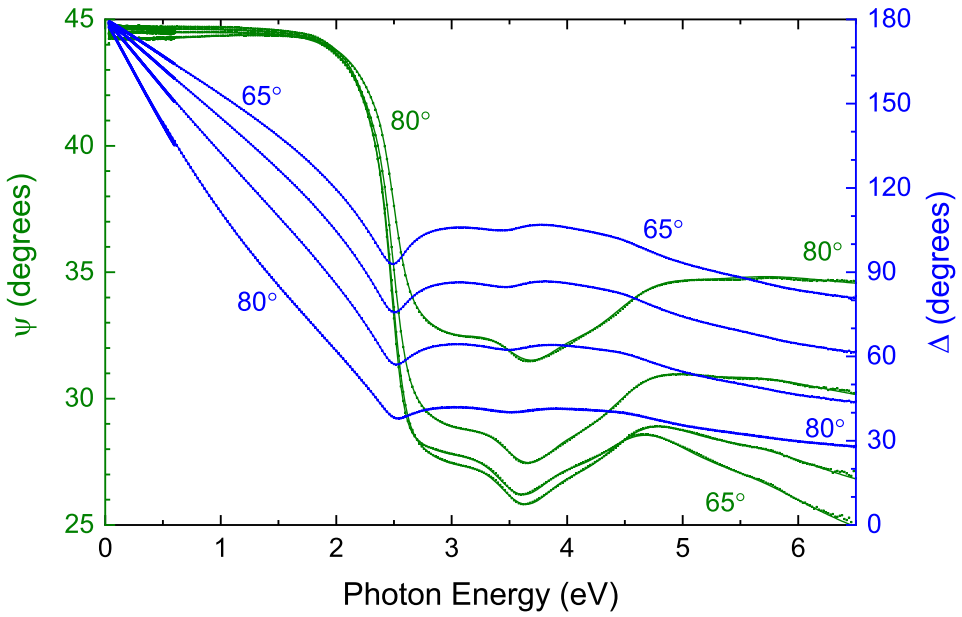

Figure 4.19: Ellipsometric angles ψ and Δ for a gold mirror measured in air as a function of photon energy from 65° to 80° angle of incidence.

the physics governing the optical constants of these two materials. Using x-ray reflectance, we estimate the surface roughness of the gold mirror to be about 3 nm.

The ellipsometric angles of gold acquired at four angles of incidence (65° to 80° with 5° steps) are shown in Fig. 4.19. We see that the restrahlen band in gold is much more pronounced than in Ni. For gold, ψ stays just below 45° to about 2 eV. For Ni, ψ drops below 45° at very low energies, because of d-intraband transitions. (Within a reststrahlen band, where ψ is nearly 45°, ellipsometry is very sensitive to weak absorption processes, see Willett-Gies, 2015.) Since Au is a noble metal, the d-bands are completely full and such d-intraband transitions are not possible.

The deviation of ψ from 45° is measurable and increases with angle of incidence (0.3° for 65° incidence angle, 0.6° at 80°). It is related to the Drude scattering rate. We observe a small discontinuity in our ψ data at 1.2 eV, where the VASE ellipsometer switches detectors. The ellipsometric angle Δ decreases almost linearly from 180° with increasing photon energy.

At our low-energy end of the spectral range (0.03 eV), Δ is still a few degrees lower than 180°, especially for shallow incidence angles. The deviation of Δ from 180° is not related to the Drude scattering rate. Instead, the slope of Δ is related to the plasma frequency. At zero energy, all Δ curves converge to 180° like a fan.

The ellipsometric angle ψ drops sharply at 2.5 eV due to the onset of interband transitions. We model this transition with a Tauc-Lorentz oscillator centered at 2.54 eV. The asymmetry of this oscillator, with a sharp cutoff at the Tauc gap of 2.34 eV and a broadening of 0.47 eV shapes the knee of ψ between 1.8 and 2.3 eV. Depending on the angle of incidence, Δ has a more or less pronounced minimum at this transition. We added six Gaussians and a pole to model the dispersion and achieved an excellent fit to the data in Fig. 4.19, with the parameters listed in Table 4.4. (We chose Gaussians rather than Lorentzians to avoid the slow drop of the Lorentzians, which might influence the absorption at low energies.) The strongest Gaussians at 3.1 and 4.2 eV lead to valleys in ψ and Δ.

B) Optical constants

The pseudo-dielectric function of gold, determined from the ellipsometric angles with a point by point fit (ignoring surface overlayers) and from the model with parameters listed in Table 4.4, is shown in Fig. 4.20. The Drude divergence is much stronger in gold than in nickel, because gold has a very low scattering parameter. In gold, conduction is entirely due to s-electrons (which have a low value of Γ). The d-band conduction (with its large scattering rate) is missing in gold, because all d-bands are filled. Therefore, $< \epsilon_2 >$ dips below 1 at 1.8 eV. At higher energies, $< \epsilon_2 >$ rises again due to interband transitions. The onset of interband transitions is very sharp and stands well above the low Drude contribution, thus

Table 4.4: Parameters used to describe the optical constants of polycrystalline gold with a sum of oscillators: Energy E, Tauc gap E_g, plasma frequency $E_P = \hbar\omega_P$, broadening Γ, and the pole amplitude A are in units of eV, the Gaussian amplitudes are dimensionless. All parameters are given with three significant digits. Due to parameter correlations, the uncertainty is probably much larger.

	A	E	Γ	E_g	E_P
Drude			0.0438		8.53
Tauc-Lorentz	61.5	2.54	0.466	2.34	
Gauss 1	3.63	3.08	1.20		
Gauss 2	0.697	3.75	0.479		
Gauss 3	2.82	4.16	1.02		
Gauss 4	0.670	5.013	1.10		
Gauss 5	1.01	5.33	2.33		
Gauss 6	2.68	8.28	7.07		
Pole	21.3	423			

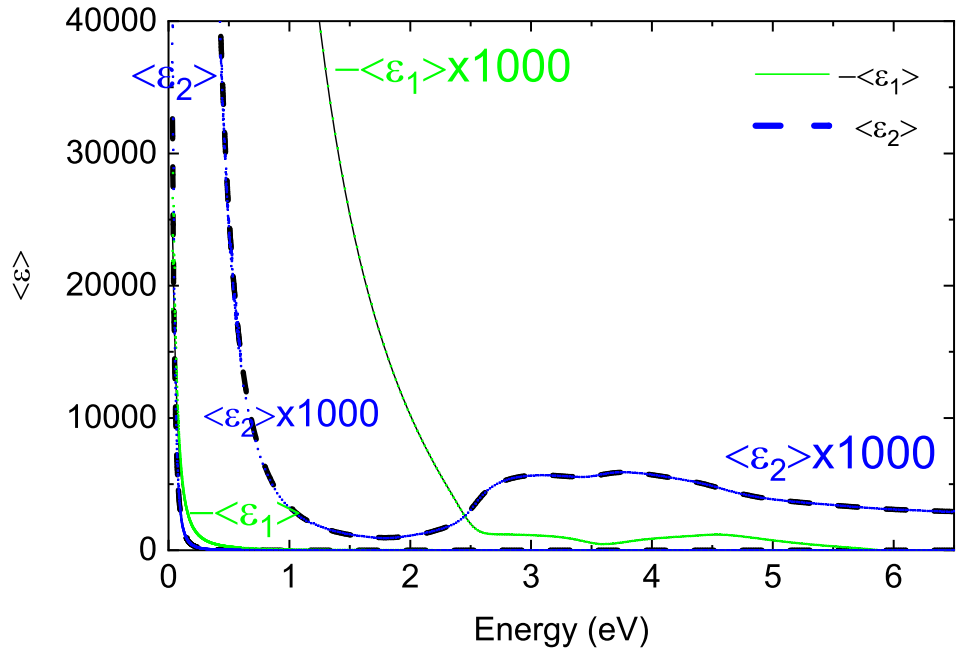

Figure 4.20: Pseudodielectric function of a gold mirror (without surface corrections). Symbols show the results of a point-by-point fit, ignoring overlayers, lines show the best fit to the ellipsometric angles using a sum of oscillators with parameters shown in Table 4.4.

the need for a Tauc-Lorentz oscillator.

The Drude divergence can be removed partially by plotting the optical conductivity, which is shown in Fig. 4.21. However, for Au the electrical conductivity at low energies is much larger than the interband conductivity above 2 eV. This makes it hard to show the electrical and interband conductivity on the same graph. From our Drude parameters in Table 4.4, we calculate a DC conductivity of 5×10^6 $1/\Omega$cm from Eq. (92), which is an order of magnitude lower than σ_0 derived from electrical measurements. The anomalous skin effect may play a role here, since high frequencies reduce the number of carriers contributing to the electronic transport (Shelton 2008).

The loss function for gold (shown in Fig. 4.22) is dominated by peaks related to interband absorption in the 2 to 4 eV range. At higher photon energies, $\mathrm{Im}(-1/ < \epsilon >)$ still rises, because the plasma frequency at 8.5 eV is outside of our spectral range. The complex refractive

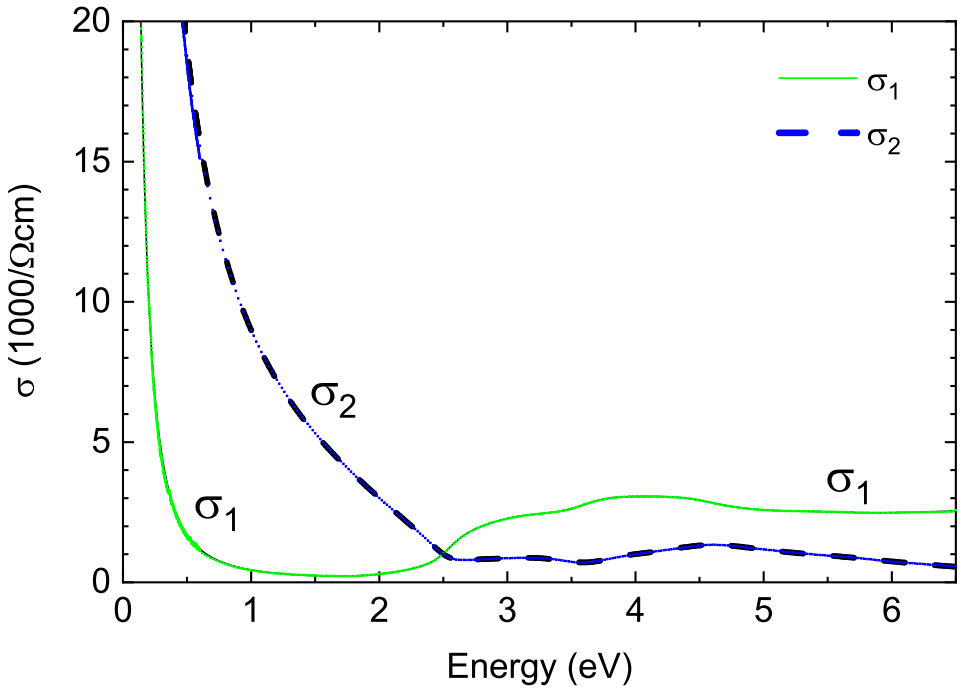

Figure 4.21: Same data as in Fig. 4.20, but shown as an optical pseudo-conductivity.

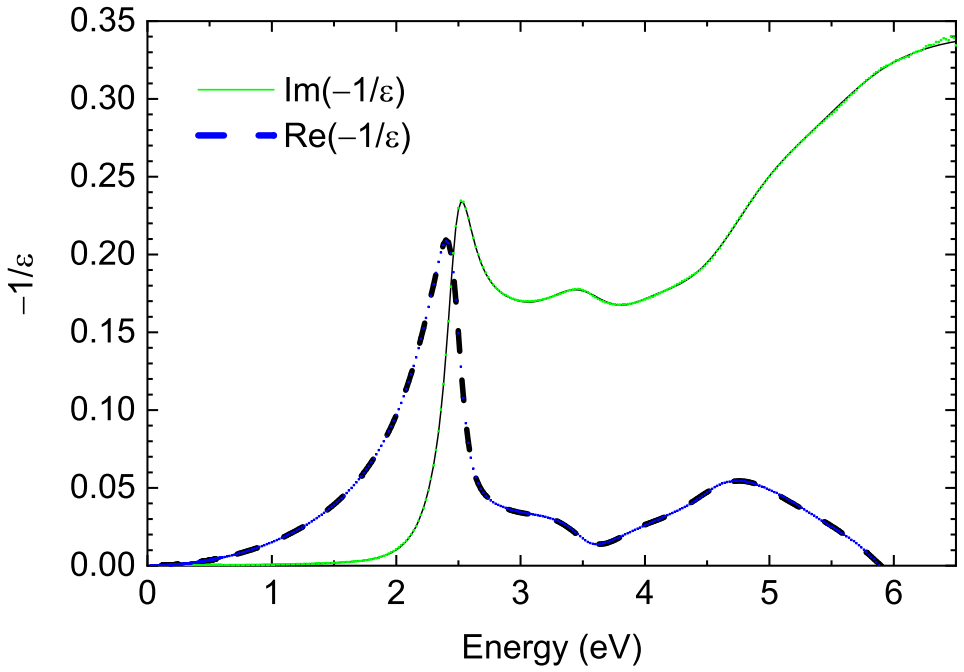

Figure 4.22: Same data as in Fig. 4.20, but shown as a pseudo-loss function.

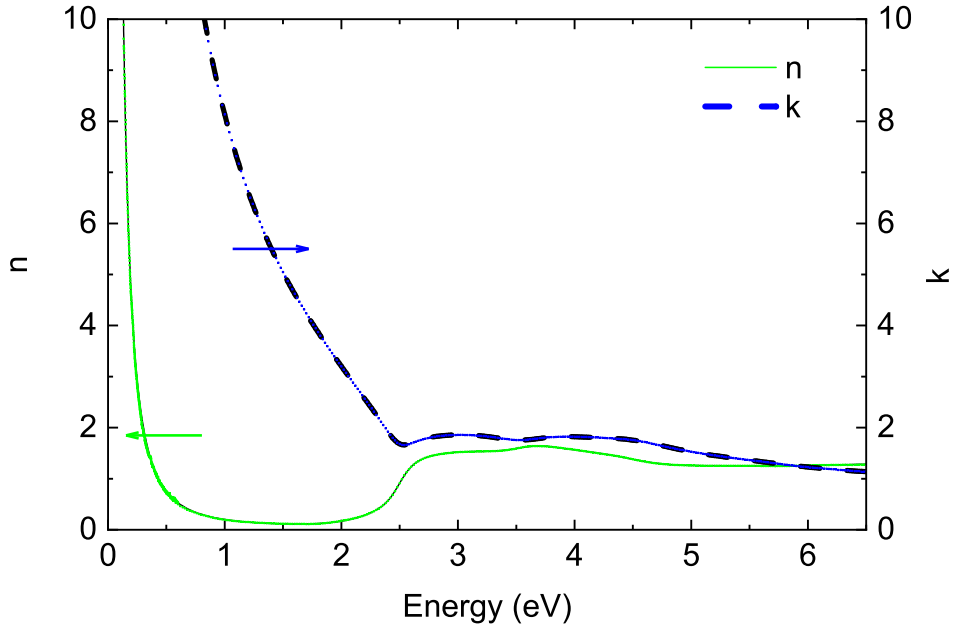

Figure 4.23: Same data as in Fig. 4.20, but shown as a complex pseudo-refractive index $<n>+i<k>$.

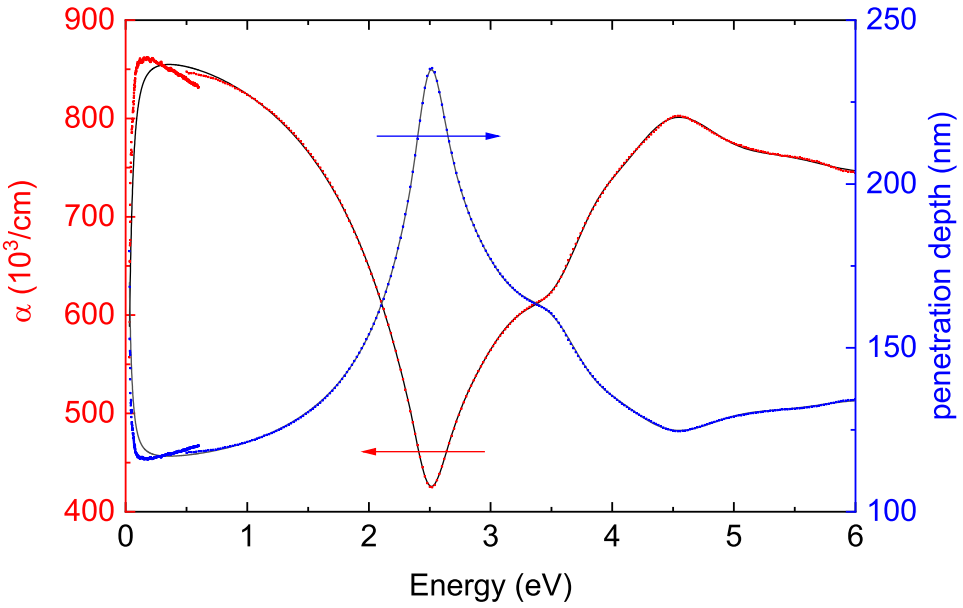

Figure 4.24: Same data as in Fig. 4.20, but shown as a pseudo-absorption coefficient $< \alpha >$ and a pseudo-penetration depth $< \lambda_P >$.

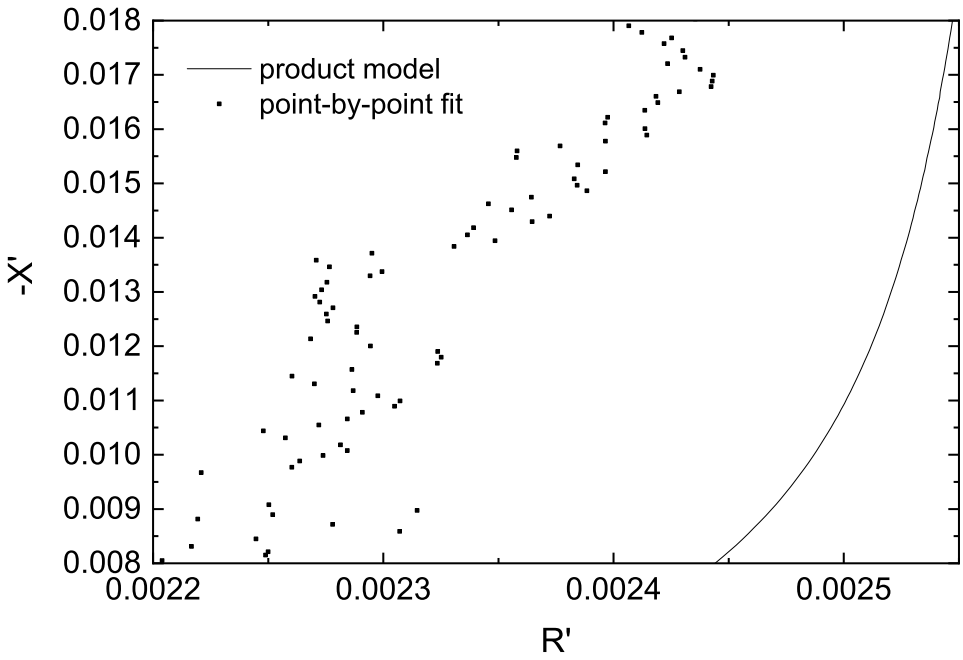

Figure 4.25: Argand diagram of the complex optical pseudo-impedance of gold at 300 K (in units of Z_0) defined in Eqs. (117) and (118) in the mid-infrared (from 0.07 to 0.16 eV), calculated from the complex pseudo-dielectric function shown in Fig. 4.20. Small symbols show results from a point-by-point fit. The line was calculated from the Drude-Lorentz model with parameters in Table 4.4.

index is shown in Fig. 4.23. We note that $< n > \ll < \kappa >$ (Fox 2010). Interband transitions are more obvious in $< n >$ than in $< \kappa >$. The pseudo-absorption coefficient $< \alpha >$ and the pseudo-penetration depth $< \lambda_P >$ are shown in Fig. 4.24. We note that a discontinuity in the data near 0.7 eV, where we have merged data from both ellipsometers. Also, the absorption coefficient is more sensitive to small differences between data and model. The absorption coefficient is small at the longest wavelengths and then rises sharply and reaches a global maximum near 0.3 eV. It then falls gradually and reaches a global minimum near 2.5 eV, just below the onset of interband transitions. As we compare the penetration depth in the mid-infared between Au and Ni, we notice that the penetration depth is only 125 nm below 1 eV, signifcantly lower than for Ni due to the absence of d-intraband transitions in Au. This will have consequences for the anomalous skin effect in both materials. The complex optical pseudo-impedance of gold at 300 K (in units of Z_0), defined in Eqs. (117) and (118), is shown in Fig. 4.25 in the mid-infrared spectral region (from 0.07 to 0.16 eV). We note that the resistance of gold is lower than the resistance of Ni, as expected. The reactance also is much smaller for gold. This graph clearly shows the discrepancy between our model and the point-by-point fit results.

C) Drude parameters

To determine the plasma frequency graphically using Eq. (82), we plot ϵ_1 versus $1/E^2$ in Fig. 4.26. We find E_P=8.13 eV, which is in good agreement with our parameter E_P=8.53 in Table 4.4 determined from a Drude-Lorentz fit to the ellipsometric angles. We also plot $\epsilon_2 E$ versus $1/E^2$, which yields $E_P^2\Gamma$=2.7 eV as the slope, in good agreement with the value of 3.2 eV calculated from the data in Table 4.4. Overall, this graph seems qualitatively similar

for Ni and Au and therefore free carrier absorption should play an important role in both materials.

The frequency-dependent mass parameter $m^*(E) = m[1 + \lambda(E)]$ calculated from Eq. (96) and its inverse, the frequency-dependent plasma frequency $E_P(E)$ are shown in Fig. 4.27. In our Drude-Lorentz model (solid line), the mass is constant in the infrared, as expected for transport with a single species of Drude carriers (dotted line). This trend is supported by the data obtained from the point-by-point fit between 0.2 and 0.8 eV (symbols). In the visible, the mass peaks sharply, as interband transitions contribute as well. The initial rise of the mass below 0.2 eV is puzzling. In a complementary view, the plasma frequency drops here. This is not supported by our Drude-Lorentz model. Indeed, as we explore the ellipsometric angles in this spectral region, we find that ψ approaches the ideal metallic value of 45° faster than predicted by our Drude-Lorentz model, see Fig. 4.28. It is not clear if this is an issue with our model parameters, an experimental error in the ellipsometry measurement, or a physics effect, such as the anomalous skin effect or diffraction effects described by Humlíček and Bernhard (2004). This discrepancy requires additional work, for example measurements at low temperatures on a clean Au sample.

The frequency-dependent scattering rate for gold at 300 K, calculated from Eq. (97), is shown in Fig. 4.29. It is quite apparent that the scattering rate is nearly independent of energy in the infrared, as expected from the Drude response for an electron gas with a single species of carriers (shown by the dotted line). It increases only slightly from 0.042 at 0.03 eV to 0.049 eV at 1eV, similar to the Drude scattering rate of 0.044 eV in our Drude-Lorentz model, see Table 4.4. This slight increase is probably from the tail in our Tauc-Lorentz oscillator due to interband transitions. These interband transitions show a strong rise in the

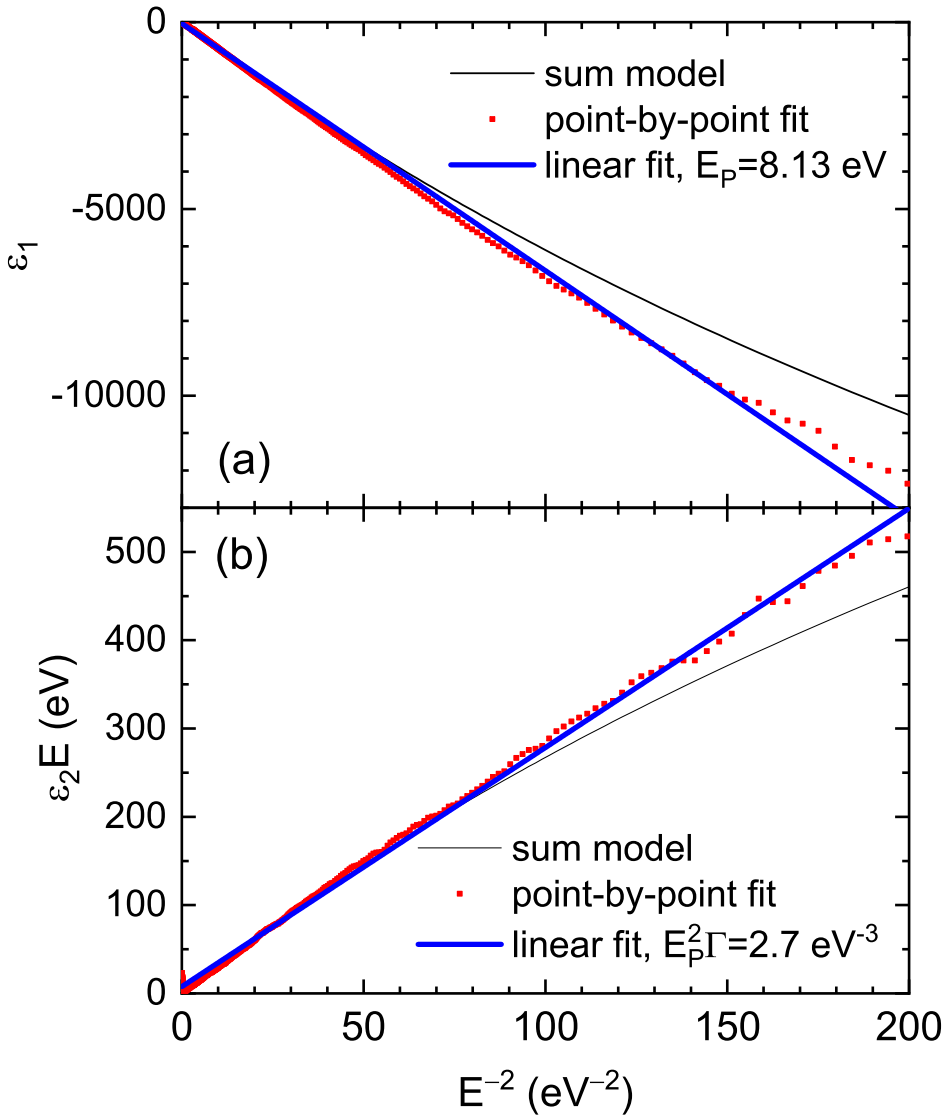

Figure 4.26: Same as Fig. 4.7, but for gold (without surface corrections).

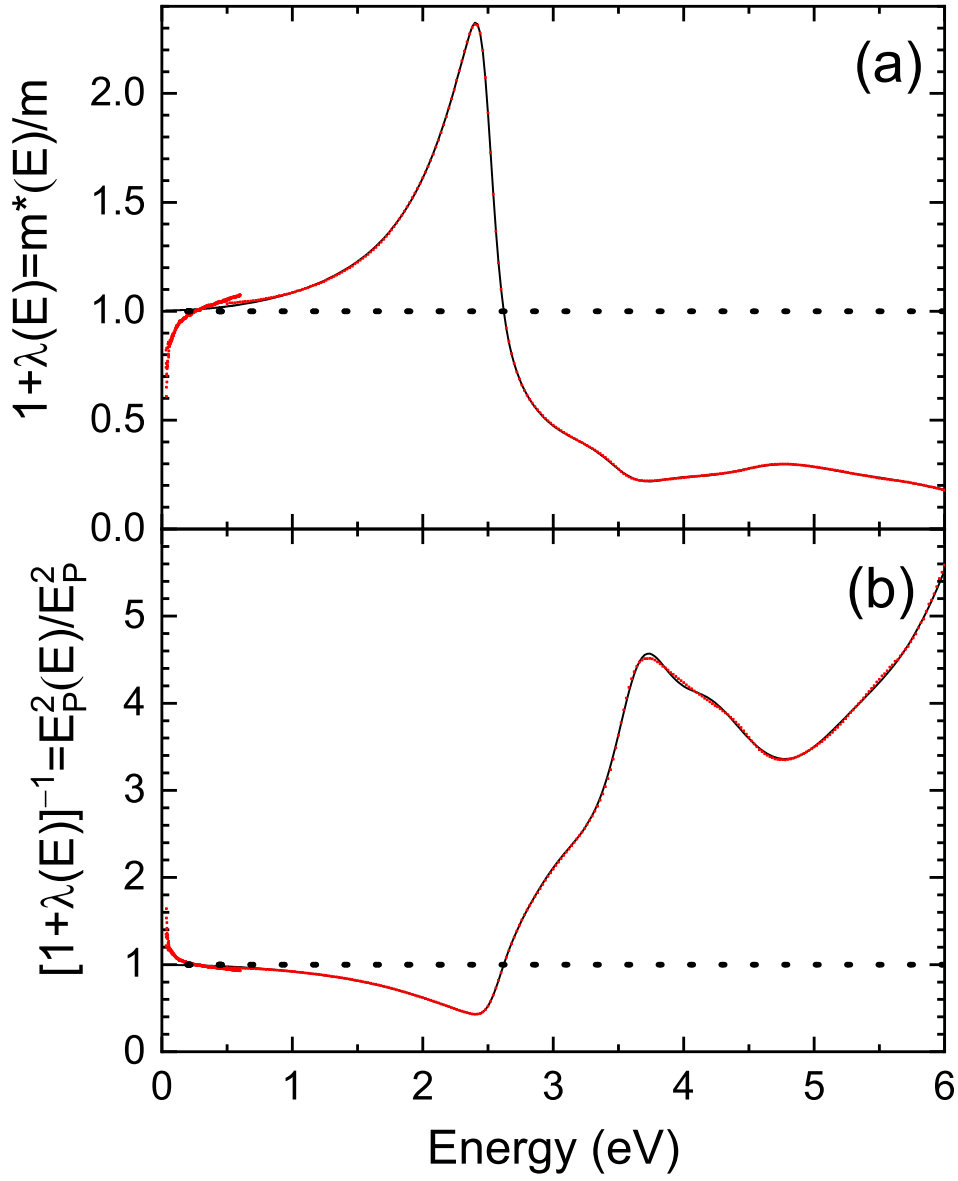

Figure 4.27: Mass enhancement factor $1 + \lambda(E)$ (a) and its inverse (b) as a function of photon energy for Au at 300 K, calculated from Eq. (96). The dotted line shows results calculated from a Drude model with a single carrier species. The symbols and solid lines show results calculated from our experimental data and our Drude-Lorentz model, respectively. We assumed a value of E_P=8.53 eV for the plasma frequency in this figure.

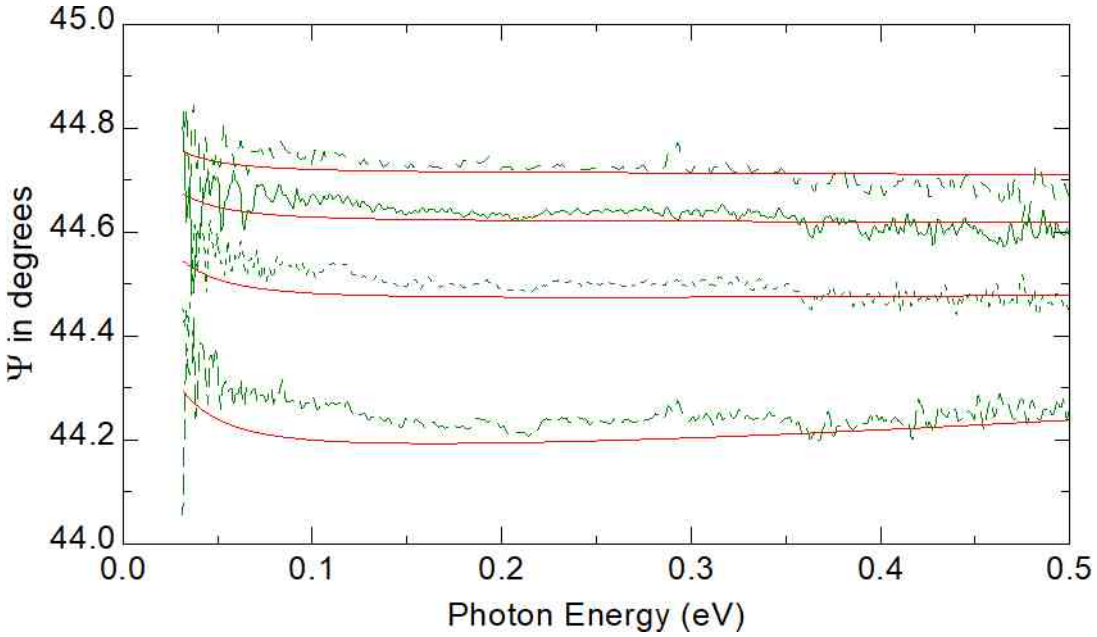

Figure 4.28: Ellipsometric angle ψ of gold at 300 K in the infrared. Green and red lines show experimental data and results from a Drude-Lorentz model, respectively. The experimental data approach 45° faster than our model at the lowest energies.

scattering rate in the visible and UV spectral regions. This nearly constant scattering rate for gold is in stark contrast to Ni, see Fig. 4.16. Conduction from d-electrons in Ni (with a much larger scattering rate) causes a nearly linear rise of $\hbar/\tau^*$. Since the d-bands are full in gold and do not contribute to electronic conduction, there is only one species of Drude carriers and thus a nearly frequency-independent $\hbar/\tau^*$.

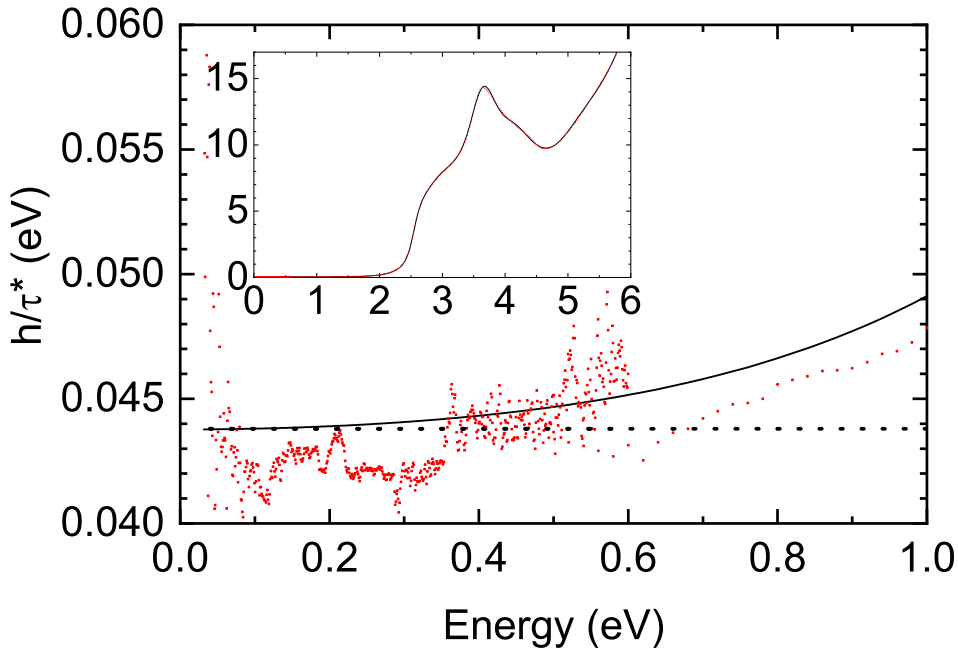

Figure 4.29: Frequency-dependent scattering rate as a function of photon energy for gold, calculated from Eq. (97). The symbols and solid lines show results calculated from our experimental data and our Drude-Lorentz model, respectively. The dotted line shows the Drude response without the Lorentz contributions of interband transitions.

5 OPTICAL CONSTANTS OF SINGLE-CRYSTALLINE NI(100) FROM 77 K TO 770 K FROM ELLIPSOMETRY MEASUREMENTS

5.1 Abstract

Ellipsometry measurements were taken on single-crystalline Ni(100) at various temperatures between 77 K and 770 K. DC conductivity and resistivity are extracted from the model optical constants and their temperature dependence is discussed. The authors find only qualitative agreement in the general shape of the resistivity measured by ellipsometry and electrical measurements. The temperature dependence of the main absorption peak at 4.8 eV indicates that the interband transitions are broadened by magnons with an effective energy of about 77 meV. The reduction of the width of the main absorption peak is found to be 0.31 eV and is interpreted as the ferromagnetic exchange energy at the L-point. The temperature dependence of the absorption peak at 1.5 eV is explained by assigning the peak to $L_{3\downarrow} \rightarrow L_{3\downarrow}$ transitions, which accounts for the decrease in magnitude of the peak and its constant energy.

5.2 Introduction

This paper is an extension of our previous article [82], hereafter referred to as I, where we modeled the dielectric function of bulk poly-crystalline Ni from ellipsometry measurements in an energy range of 0.06 eV to 6 eV at 300 K. The model consists of two Drude and five Lorentzian oscillators to describe the two carrier types (s- and d-electrons) and interband transitions. In this work, we model the dielectric function of single-crystalline Ni(100) at temperatures from 77 K to 770 K with temperature steps of about 50 K. The temperature

dependence of interband transitions shines light on the origin of the absorption peaks in the optical conductivity. Nickel has been extensively studied theoretically and experimentally, for instance in Refs.70, 83–89 and the references therein. This paper is inspired by the work of Shiga and Pells [49] and Kirillova et. al. [90] who studied the temperature dependence of the optical properties of poly-crystalline and single-crystalline Ni(110), respectively. The purpose of this work is to investigate the discrepancies that are observed in the description of the temperature dependence of the energy of the main peak. Shiga and Pells [49] describe the red shift of the main absorption peak in the optical conductivity as a linear shift. In this work, we fit the red shift with a Bose-Einstein model [91] and further discussion about the interband transitions is provided. In addition, the temperature dependence of the absorption peak at 1.5 eV is studied using the change of optical conductivity [92] $\delta\sigma = \sigma(T) - \sigma(77)$. This new method reveals a significant feature of this peak that has not been observed before due to being buried under the large plasma frequencies of Ni. This method also provides a new insight into the origin of the absorption peak at this energy.

5.3 Experimental Results and Data Analysis

The measurements were taken on a 10×10 mm^2 single-crystalline Ni(100) sample with a thickness of 1 mm that was obtained commercially [55]. The cleaning procedure and experimental setup are described in I. After heat treating the sample in a UHV cryostat at 770 K and at a pressure of 10^{-7} Torr, ellipsometry measurements were taken by a J. A. Woollam VASE ellipsometer from 0.5 eV to 6.5 eV with a step size of 20 meV from 770 K to 77 K in 50 K steps. The sample was kept at each temperature for 30-45 min to reach a thermal equilibrium. Afterwards the same measurements were taken from 77 K to 770 K. No significant

changes in the data at the same temperatures in the two runs of increasing and decreasing temperature were observed. Next, the sample was mounted in another UHV cryostat with diamond view ports and was heat treated at 770 K to remove possible contamination and oxidation from transferring the sample from one instrument to the other. The same ellipsometry measurement were then taken by a J. A. Woollam FTIR ellipsometer from 0.03 eV to 0.8 eV with a resolution of 16 cm^{-1}. The data from two instruments were merged using the method explained in appendix A. Two Drude and four Lorentzian oscillators were used to model the dielectric function of Ni. This model has one Lorentzian oscillator less than in I, because the new merging procedure removes the mismatch between the data from two instruments and reduces the minimum number of oscillators needed to model the dielectric constant, which is given by six oscillators with a total of 16 parameters to fit [82]

$$\epsilon(E) = 1 + \sum_{i=1}^{2} \frac{-E_{p,i}^2}{E(E + i\gamma_i)} + \sum_{i=1}^{4} \frac{A_i E_{0,i}^2}{E_{0,i}^2 - E^2 - i\gamma_i E}. \tag{123}$$

Figure 5.1 demonstrates the measured ellipsometric angles of cleaned single-crystalline Ni(100) for a 70° angle of incidence at 300 K modeled by Eq. (123) with the parameters given in Table 5.1. To minimize the number of correlated parameters, the energy of the first Lorentzian oscillator at about 1.5 eV is retained constant as suggested by Fig. 5.2, which shows the change in the optical conductivity with temperature, and other studies [49]. Furthermore, the broadening of the Lorentzian oscillator at about 12 eV is retained constant since it is beyond our spectral range. All data were corrected for 20 Å of surface roughness.

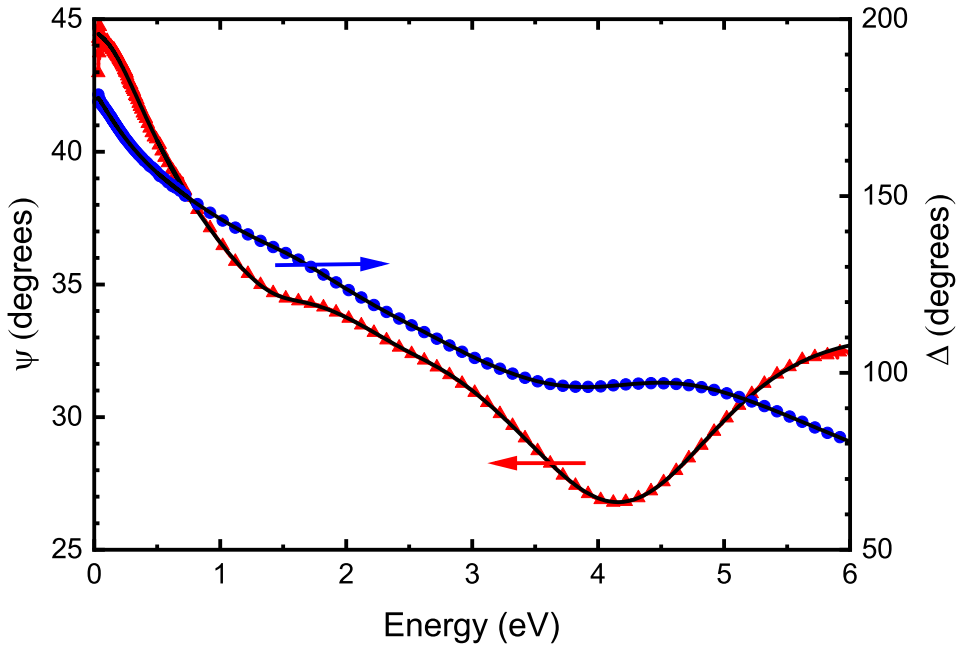

Figure 5.1: Ellipsometric angles ψ (▲) and Δ (●) of clean single-crystalline Ni(100) at 300 K at an angle of incidence of 70°. Symbols show experimental data, lines the best fit with Eq. (123) and parameters in Table I. Not all data points are shown.

Table 5.1: Parameters used to describe the optical constants of single-crystalline Ni(100) at T = 300 K: Amplitude A, plasma energy E_p, energy E_0, and broadening γ. The DC conductivity σ_0 was calculated from the Drude parameters using Eq. (124).

	A	E_P	E_0	γ	σ_0
	(1)	(eV)	(eV)	(eV)	(1/Ωcm)
Drude 1		12.1		2.91	6,766
Drude 2		4.81		0.0403	77,200
Lorentz 1	1.83		1.57	0.847	
Lorentz 2	0.138		2.58	0.888	
Lorentz 3	2.42		4.77	2.08	
Lorentz 4	1.91		12.7	6.01	

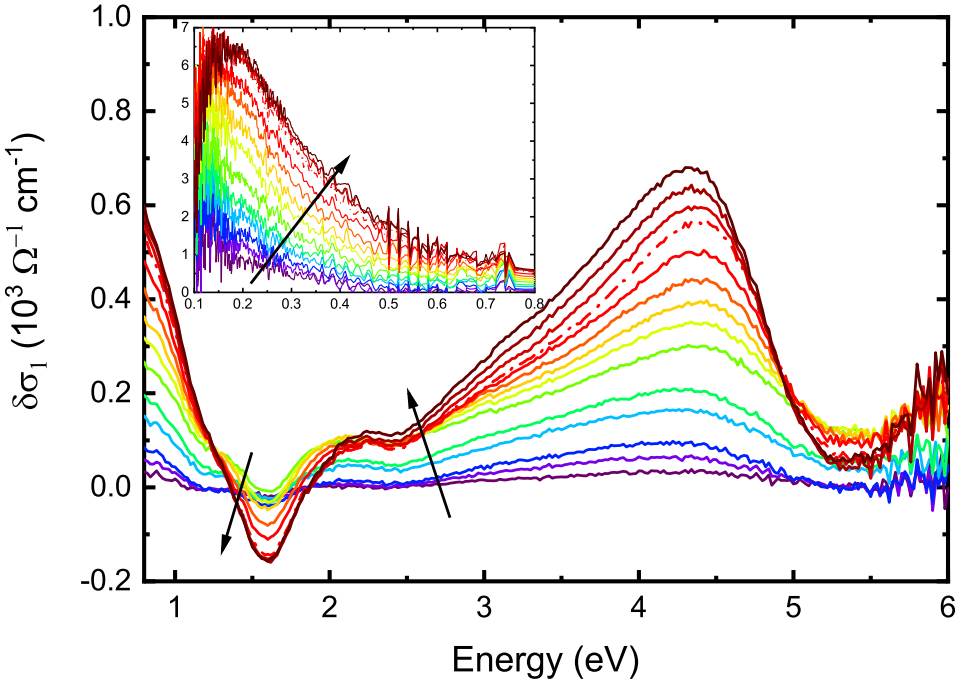

Figure 5.2: Change in optical conductivity of single-crystalline Ni (100) $\delta\sigma_1 = \sigma_1(T) - \sigma_1(77\ \mathrm{K})$ at temperatures between 77 K and 770 K. The dash-dotted line is the data at T = 627 K. The inset shows the infrared spectral range.

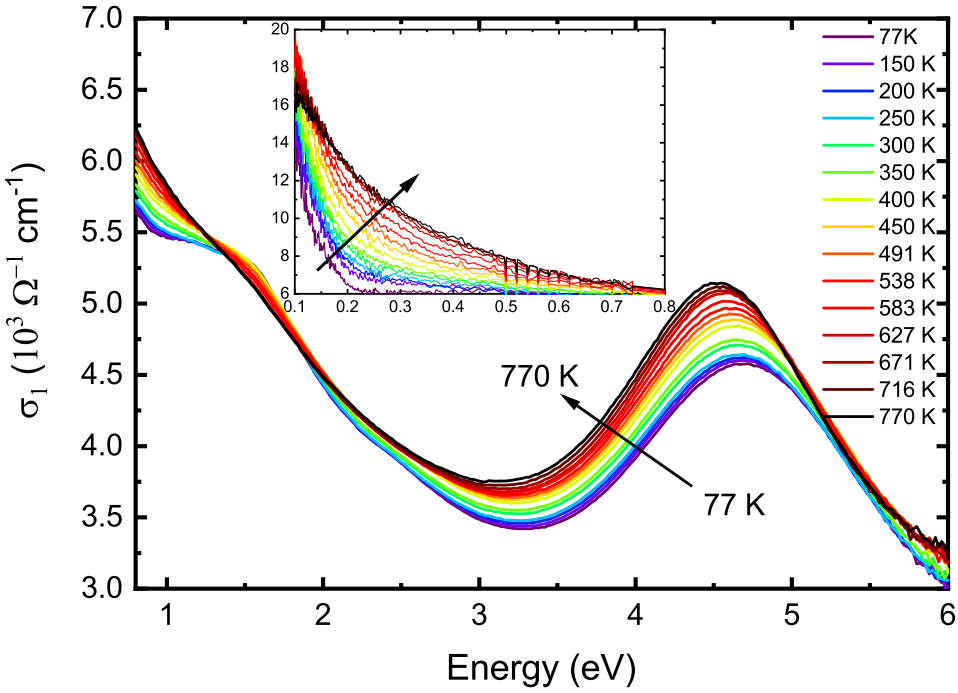

Figure 5.3: Optical conductivity of single-crystalline Ni(100) from 77 K to 770 K. The inset shows the infrared spectral range. The arrows indicate the direction of rising temperature. The data below 0.1 eV and above 6.0 eV are not shown due to noise.

5.4 Optical Conductivity

Figure 5.3 shows the optical conductivity of our Ni sample at various temperatures. Two well known features at about 1.5 eV and 4.8 eV are present [49,69,76,93]. The peak at about 1.5 eV is mainly due to the transitions within the minority spin bands (spin down), whereas both spin directions contribute to the main peak, which is dominated by transitions from the bottom of the d-band to the states near the Fermi level [72]. The temperature dependence of optical properties of Ni has been little investigated. Johnson and Christy [80] claim that the optical constants of Ni do not change over the temperature range between 77 K and 423 K and they are identical to its optical constants at room temperature. However, Fig. 5.3 displays a noticeable change in the optical constants of Ni as the temperature rises. Such changes have also been reported by Shiga and Pells [49]. Many interband transitions have been assigned to the absorption peaks based on the calculated or experimental bands structures [49, 76, 77]. Using polarimetry techniques, Stoll [77] has reported several small interband transition peaks in the optical conductivity of ferromagnetic and paramagnetic single-crystalline Ni(110) at various temperatures. We do not observe any of those peaks in the optical conductivity of our sample. Stoll's measurements on poly-crystalline Ni [76] also show many small structures between 2.0 eV and 2.5 eV, which are not observed in our data. In order to see the change of optical conductivity with temperature, Fig. 5.2 shows the change in optical conductivity at each temperature relative to the optical conductivity at our lowest temperature $\delta\sigma_1 = \sigma_1(T) - \sigma_1(77K)$. Stoll and Jung [94] suggest that the Drude term increases with temperature as function of T^2. Our measured data also indicate an increase in the Drude term as the temperature rises. However, Fig. 5.2 illustrates that

the Drude term increases with temperature up to about the Curie temperature T_c and stays almost constant above that. Another noticeable feature in Fig. 5.2 is that the magnitude of the absorption peak at 1.5 eV decreases as temperature rises and stays constant above T_c. To the best of our knowledge, this has not been reported in the literature thus far. We will discuss this matter further in section VI.

The DC conductivity can be found as the zero energy limit of the Drude response [82]

$$\sigma_{DC} = \frac{\epsilon_0}{\hbar}\frac{E_p^2}{\gamma}. \tag{124}$$

If there are more than one carrier species, the DC conductivity is defined as [41]

$$\sigma_{DC,total} = \sum_{i=1}^{n} \sigma_{DC,i}. \tag{125}$$

Figure (5.4) shows the contribution of s- and d-electrons to the total DC conductivity of Ni(100) by using Eq. (124) and Eq. (125). The s-electron contribution demonstrates the typical metallic behavior as the temperature increases. The d-electrons, on the other hand, do not contribute significantly to the total DC conductivity. This behavior can also be seen in the temperature dependence of the scattering rates of the two Drude terms in Eq. (123) shown in Fig. 5.5. This figure shows that the scattering rate of the first Drude term does not change significantly with temperature, whereas the scattering of the second Drude term increases by a factor of about 9 as temperature rises, thus attributing these terms to d- and s-electrons, respectively. Comparison of DC conductivity taken from ellipsometry measurements to electrical measurements shows that IR spectroscopic ellipsometry underestimates the DC conductivity. This is due to the fact that our ellipsometer measures down to 0.1 eV

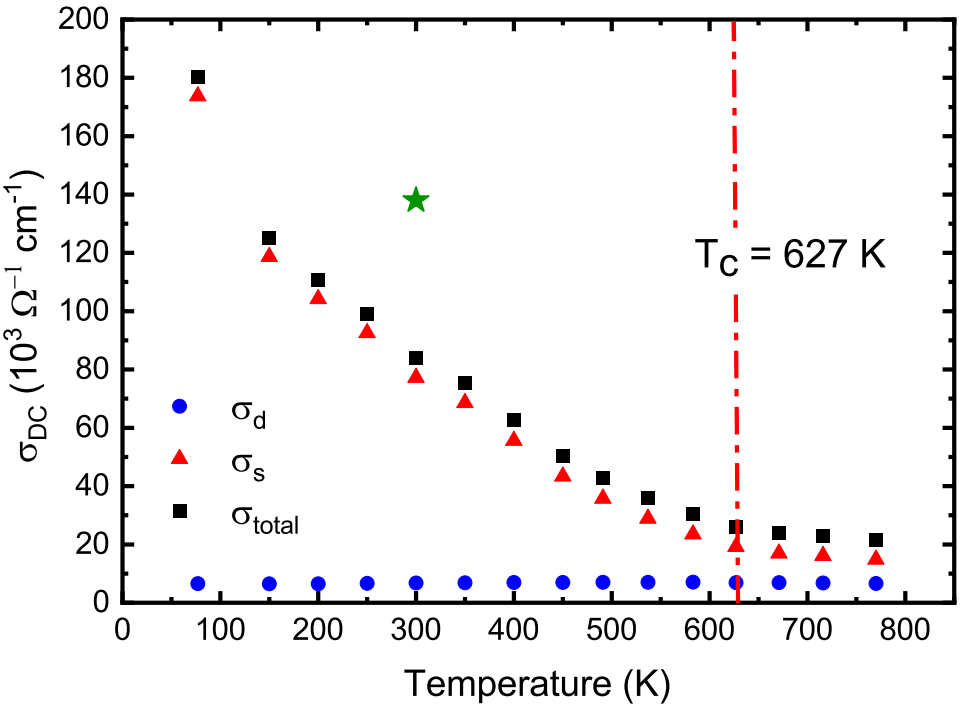

Figure 5.4: DC conductivity of Ni obtained from ellipsometry measurements. Total DC conductivity (■), DC conductivity of s-electrons (▲), DC conductivity of d-electrons (●), DC conductivity from electrical measurements (⋆). Most of the conductivity of Ni below T_c is due to s-electrons. IR spectroscopic ellipsometry underestimates σ_{DC}.

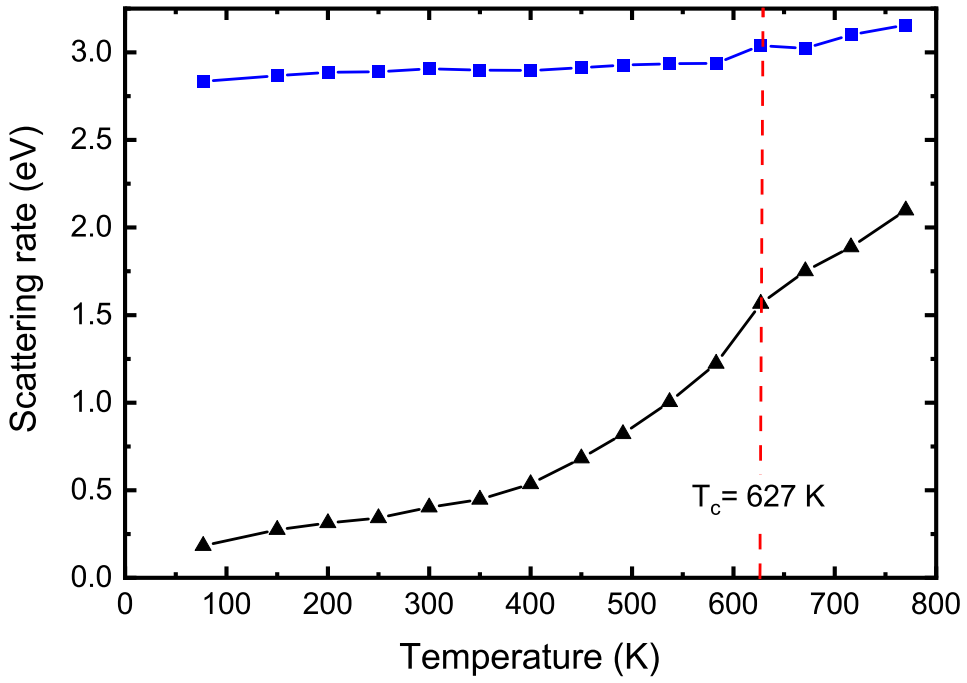

Figure 5.5: Scattering rates of the first (■) and second (▲) Drude term in Eq. (123) as a function of temperature. For clarity the broadening of the second Drude term (s-electrons) is multiplied by 10.

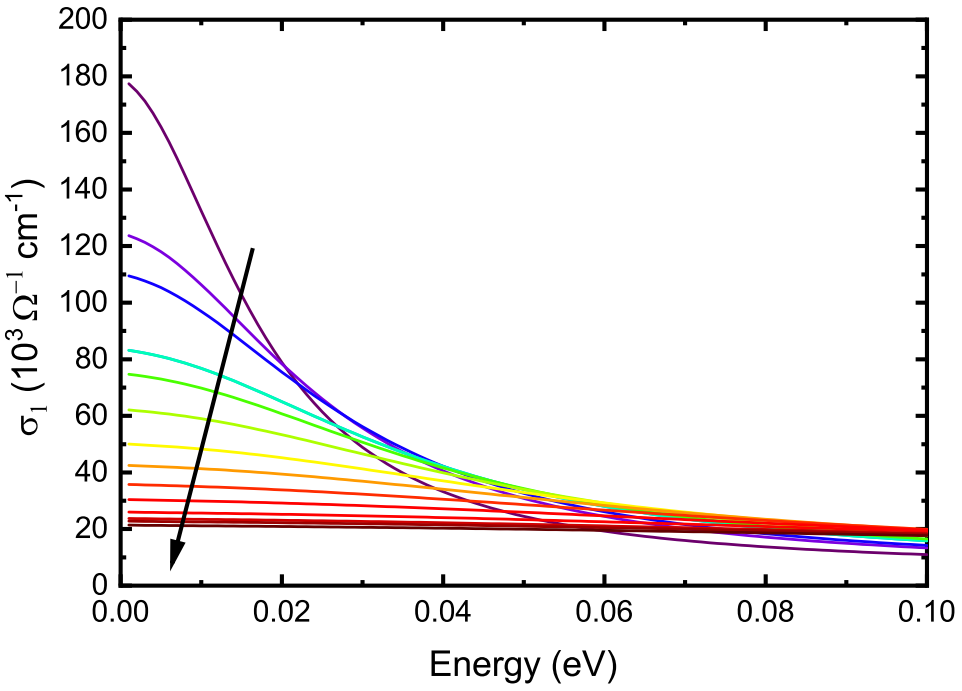

Figure 5.6: Extrapolated optical conductivity of single-crystalline Ni (100) between 77 K and 770 K. The arrow shows the direction of rising temperature.

for measurements on our sample inside the cryostat without too much noise. Below this energy one has to extrapolate the model to obtain DC conductivity. Figure 5.6 shows the optical conductivity extrapolated down to zero. As the figure shows, the difference in the optical conductivity at various temperatures becomes more important at the energies below 0.06 eV, which is lower than our spectral range.

One can calculate the number N of electrons per unit cell that contribute to the conductivity of Ni in an energy range between zero and 6.0 eV, which is defined as [92]

$$N = \frac{2m_0 V}{\pi \hbar e^2} \int_{E=0}^{E=6} \sigma(E) dE, \tag{126}$$

where V is the volume of the unit cell and m_0 is the free electron mass. As Ni has an fcc crystal structure, it has four atoms in its conventional cubic unit cell with 0.6 free

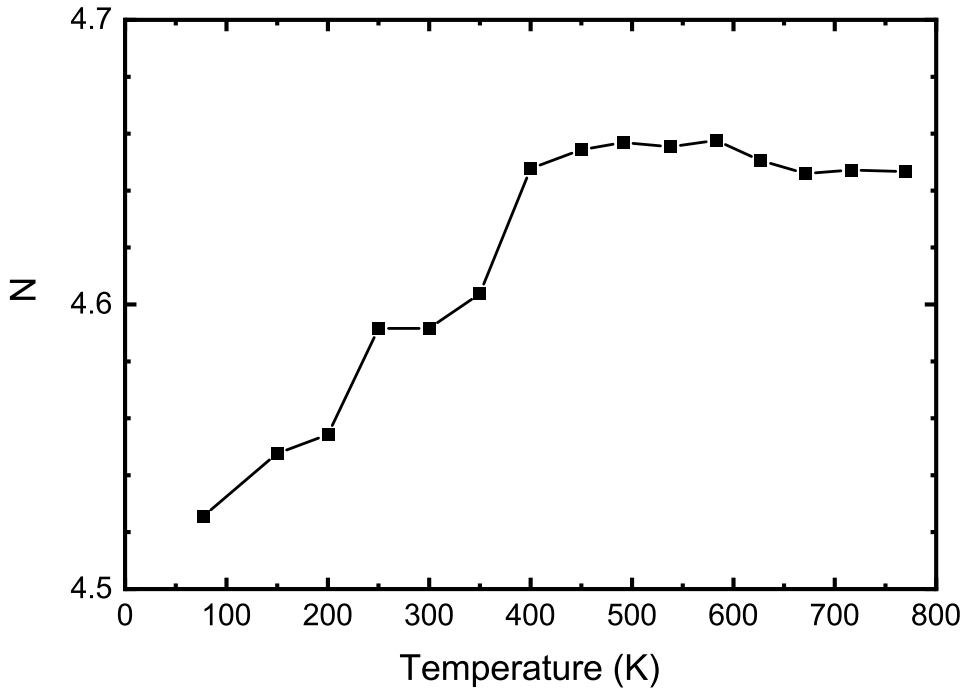

Figure 5.7: Number of electrons per cubic unit cell of single-crystalline Ni in the energy range of zero to 6.0 eV from 77 K to 770 K.

electron and 0.6 free hole per atom [6]. Figure 5.7 depicts Eq. (126) calculated at various temperatures, which shows that N increases by 3% as the temperature rises from 77 K to 770 K. This increase is in great agreement with 3% volume expansion calculated from the linear expansion coefficient taken from Wang *et al.* [95] in the same temperature interval. Therefore, N is essentially constant as the temperature rises.

The Drude term for a single carrier type can be written as [41]

$$\epsilon^D(E) = -\frac{E_p^2}{E^2 + i\gamma E} = -\frac{E_p^2}{E^2 + \gamma^2} + i\frac{E_p^2\gamma}{E(E^2 + \gamma^2)}, \tag{127}$$

which yields

$$\epsilon_1^D(E) = -\frac{1}{\gamma}(E\epsilon_2^D). \tag{128}$$

This relation is applicable well below the onset of interband absorption edge, where only

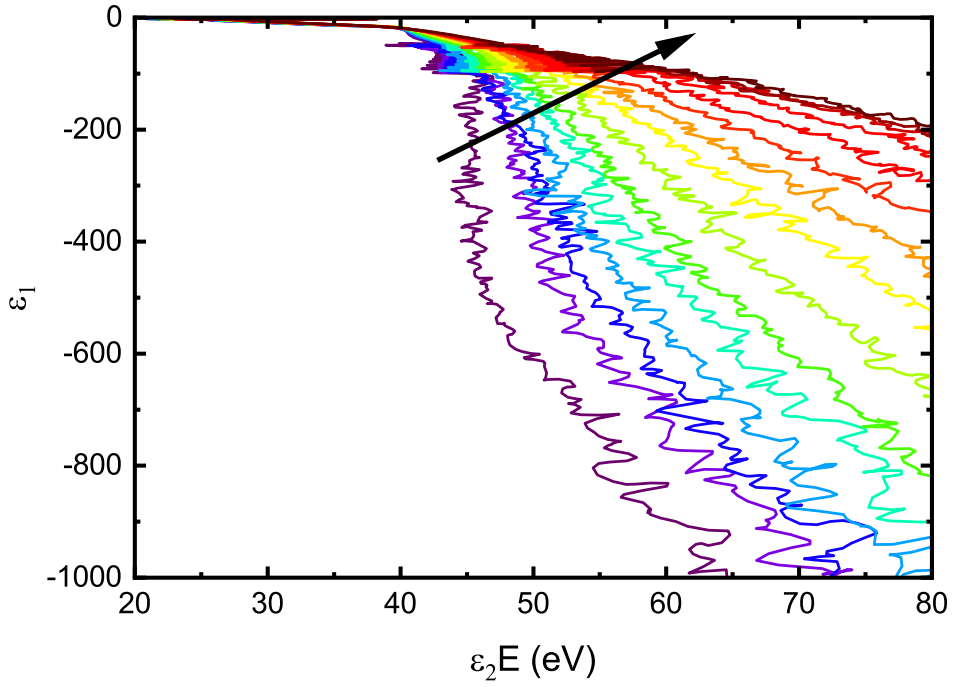

Figure 5.8: ϵ_1 vs. $E\epsilon_2$ for single-crystalline Ni(100).

free carrier absorption is present. According to Eq. (128), plotting ϵ_1 against $E\epsilon_2$ should be linear and the slope be equal to $-1/\gamma$. Figure 5.8 shows ϵ_1 vs. $E\epsilon_2$ of Ni at various temperatures. Fitting a line in the linear region of Fig. 5.8, we calculated the scattering rate in Eq. (128). We find good agreement between this scattering rate and the scattering rate of s-electrons in Eq. (123) as demonstrated in Fig. 5.9.

It has been suggested [96] that the deviation from linearity in Fig. 5.8 indicates the onset of interband absorption. The linear region in Fig. 5.8 is between $\epsilon_2 E = 50$ eV and $\epsilon_2 E = 80$ eV. From this figure, it is found that deviation from linearity occurs at $E \approx 0.5$ eV and varies with temperature. However, it has been shown [97, 98] that the onset of an interband absorption in Ni occurs at about 0.15 eV and is independent of temperature. The

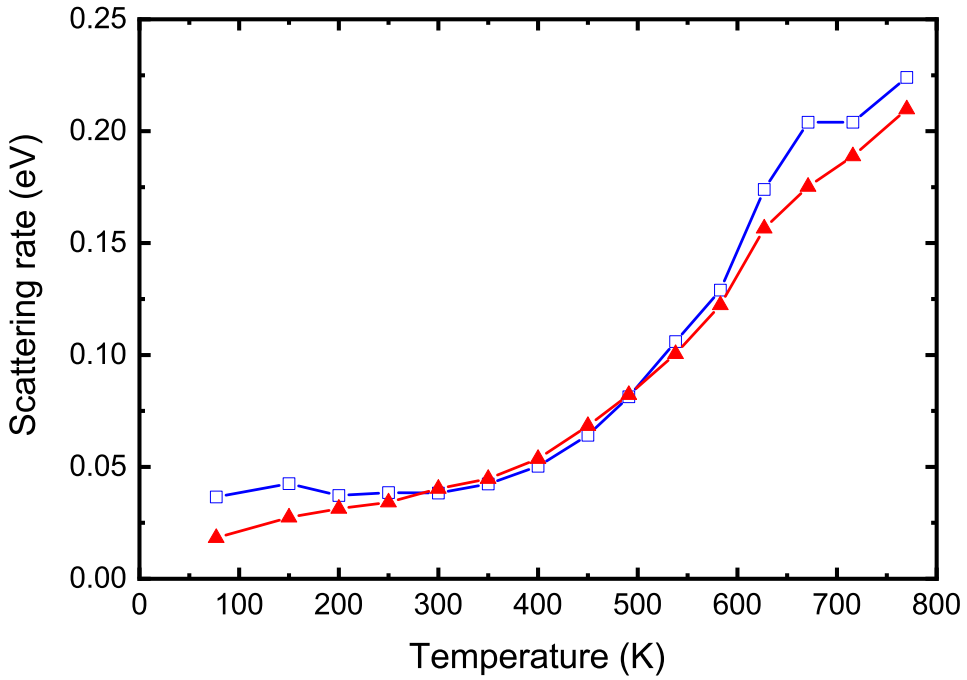

Figure 5.9: Scattering rate obtained from Eq. (128) (□), and the scattering rate of the second Drude term (s-electrons) in Eq. (123) (▲) at various temperature.

reason for this discrepancy might be the fact that there are two Drude terms in the dielectric function of Ni. Assuming two Drude terms, Eq. (127) becomes

$$\epsilon^D(E) = -\frac{E_{p1}^2}{E^2 + i\gamma_1 E} - \frac{E_{p2}^2}{E^2 + i\gamma_2 E}, \tag{129}$$

which yields

$$\epsilon_1^D(E) = \frac{E_{p1}^2(E^2+\gamma_2^2) + E_{p2}^2(E^2+\gamma_1^2)}{E_{p1}^2\gamma_1(E^2+\gamma_2^2) + E_{p2}^2\gamma_2(E^2+\gamma_1^2)}(E\epsilon_2^D). \tag{130}$$

Due to the large value of the scattering rate of the first Drude term from Table I at 300 K($\gamma_{D1} = 2.91$ eV), Eq. (130) is linear only well above the onset of interband absorption, where $(\gamma_1/E)^2$ becomes negligible. Therefore, it appears that this method cannot be used to find the onset of interband transitions of transition metals. The failure of this method also justifies the use of two Drude terms in the optical properties of Ni.

5.5 Resistivity

The resistivity of Ni is governed by scattering of free electrons by impurities (ρ_{imp}), lattice vibrations (ρ_{e-ph}), other electrons (ρ_{e-e}), and magnons (ρ_{e-mag}). According to Matthiessen's rule, the total DC resistivity of Ni may be written as a sum of these terms [99]

$$\rho_{total} = \rho_{imp} + \rho_{e-e} + \rho_{e-ph} + \rho_{e-mag}. \tag{131}$$

The first term in Eq. (131) is the residual resistivity and can be neglected only for highly pure metals [7]. However, there are two more contributions in the residual resistivity of ferromagnets, namely magnetostriction and magnetocrystal residual resistance [7], that cannot be ignored even for highly pure samples.

The electron-electron scattering term is called Baber interaction [87] and takes into account the electron-electron and electron-hole scattering

$$\rho_{e-e} = \frac{2m}{ne^2}\left(\frac{e^2}{2m}\right)^2 \frac{m^3}{h^3}\left(\frac{kT}{\zeta_1}\right)^2 \frac{e^{\Delta}(\pi^2+\Delta^2)}{2(e^{\Delta}+1)^2} H(\beta, q), \tag{132}$$

where m is the effective mass of the light carrier, ζ_1 is Fermi energy of the group of light carriers, $\Delta = \frac{m}{2kT}(u^2 - V_1^2)$ with the velocity u of the electron and the velocity $V_1$of the electron at the Fermi surface, $\beta = m_2/m_1$ and q is the screening factor that screens the field of a positive hole by a factor of e^{-qr}. Reference 87 provides numerical values of the function $H(\beta, q)$ for different effective mass ratios and screening factors. For sufficiently low temperatures where lattice vibrations can be neglected, Eq. (132) can be written as [7]

$$\rho_{e-e} = \frac{\pi^2 e^2 m^2}{16nh^3}\left(\frac{kT}{\zeta_1}\right)^2 H(\beta, q) = aT^2, \tag{133}$$

which shows that at low temperatures, the electron-electron interaction contributes to the temperature dependence of the resistivity as T^2. This term is negligible when β is unity as

in the case of Cu [87] and is appreciable for Ni, where $m_d/m_s = 22$ [99]. If there is only one type of carriers, electron-electron interaction contributes to the conductivity only when there is an electron-electron umklapp scattering process, whereas normal scattering does not contribute to the conductivity [7]. For more than one type of carriers, as in the case of Ni, the electron-electron scattering contributes to the conductivity according to Eq.(133) even if there is no umklapp process [7].

Scattering of electrons by phonons may be written as [100]

$$\rho_{e-ph} = 4A \left(\frac{T}{\theta_D}\right)^5 \int_0^{\theta_D/T} \frac{x^5}{(e^x - 1)(1 - e^{-x})} dx, \tag{134}$$

where A is a constant and θ_D is the Debye temperature. $\theta_D = 345\ K$ at $T = 293\ K$ [2] and $\theta_D = 477\ K$ at $T = 0\ K$ [3]. The resistivity $\rho_{e-ph} \propto T^5$ for T<< θ_D, and $\rho_{e-ph} \propto T$ for $T > \theta_D$. This temperature dependence is common in all metals. Another term that contributes to ρ_{e-ph} of transition metals is the shortening of the electron free path due to the scattering of s-electrons into d-electron bands upon collision with phonons, which was proposed by Mott [83] and calculated by Wilson [86]

$$\rho_{e-ph}^{sd} = d \left(\frac{T}{\theta_D}\right)^3 \int_{\theta_E/T}^{\theta_D/T} \frac{x^3}{(e^x - 1)(1 - e^{-x})} dx, \tag{135}$$

where d is a constant and $k\theta_E = h\nu_E$ with ν_E being the minimum frequency required to excite s-d transitions, and k is the Boltzman constant. Eq. (135) is proportional to T^3 and implies that s-d scattering is dominant at high temperatures. At sufficiently low temperatures, ρ is dominated by the normal s-s and d-d scattering events [86].

The last factor contributing to the resistivity of Ni is the scattering of electrons by magnons. This scattering mechanism results in a change in the direction of the spin of an electron [101] by annihilation or creation of magnons. The temperature dependence of the scattering between electrons and magnons in the range of $T_0 < T < 0.1T_c$, where spin wave approximation is applicable, is [7]

$$\rho_{e-mag}(T) \sim \exp\left(-\frac{T_0}{T}\right) \quad \text{at} \quad T \ll T_0, \tag{136}$$

$$\rho_{e-mag}(T) \sim T^2\phi\left(\frac{T_0}{T}\right) \quad \text{at} \quad T \approx T_0, \tag{137}$$

$$\rho_{e-mag}(T) \sim T^2 \quad \text{at} \quad T \gg T_0, \tag{138}$$

where

$$\phi(t) = \frac{3}{2\pi^2}\int_t^\infty \frac{xe^x}{(e^x-1)(x-1)}dx; \quad t = \frac{T_0}{T}. \tag{139}$$

Goodings [102] calculated that below 10-20 K the magnon assisted s-d scattering is negligible and ρ_{e-mag} is dominated by s-s scatterings. He also found that at room temperature ρ_{e-mag} due to s-d scattering is significantly greater than that of s-s scattering (about 130 times) and s-d scattering by two magnons, where the spin of the electron is unchanged, is two orders of magnitude smaller than s-d scattering by one magnon. Following Goodings' work, Raquet *et al.* [99, 103] showed that 30% of the resistivity of Ni at room temperature is due to the spin-flip scattering via magnons and an extremely large external magnetic field is needed to reduce the magnetic resistivity to zero. They found the frozen temperature T_0, below which the electron magnon scattering is non-effective, to be $T_0 \approx 15$ K for $s^{\pm}$-$d^{\mp}$ scattering and $T_0 \approx 40$ K for $d^{\pm}$-$d^{\mp}$ scattering. By increasing T above T_c the concentration of spin waves increases [6] and reaches its maximum, thus a constant contribution to the

resistivity is equal to [104]

$$\rho_{e-mag} = \frac{k_F (m\Gamma)^2}{4\pi e^2 z \hbar^3} J(J+1). \tag{140}$$

Here, J is the effective local spin, Γ is a coupling parameter and z is the atomic number. Therefore, above T_c the temperature dependence of the resistivity of Ni is proportional to T due to the temperature dependence of phonons [105]. However, the resistivity of Ni in the paramagnetic region is not entirely due to the electron-phonon scattering. Other scattering mechanisms, such as electron-electron scattering, also contribute to the resistivity [106].

Figure 5.10 displays the resistivity of a single-crystalline Ni(100) (this work) and resistivity of poly-crystalline Ni by other authors [100,101,106]. The overall temperature dependence of the resistivity is in only qualitative agreement with Laubitz et al. [106]. This is probably due to the different methods of the measurement of the resistivity and also the fact that the resistivity from ellipsometry measurements is derived from an extrapolation, not from a direct and contact measurements on the sample. Another discrepancy that can be observed is the Curie temperature in our measurement which appears to be slightly higher than the accepted Curie temperature of Ni, $T_c = 627$ K. This is probably due to temperature gradient between the thermocouple and the sample. Figure 5.11 shows $\log(\rho)$ vs. $\log(T)$ and the fitted lines in selected regions. The resistivity shows a temperature dependence of T^2 between θ_D and T_c. In this temperature interval both electron-phonon and electron-magnon interactions contribute to the resistivity of Ni. Although $\rho_{e-mag} \propto T^2$ at low temperatures, its temperature dependence is not a simple function of T at higher temperatures [107]. The stiffness of the spin waves decreases as temperature rises and its value at T_c decrease to

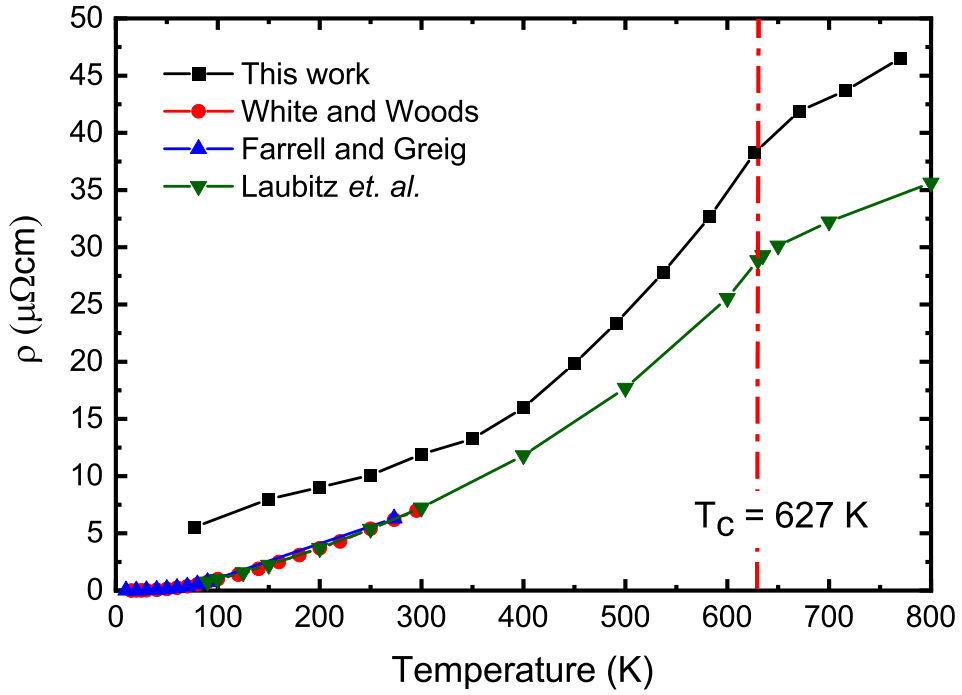

Figure 5.10: Comparison of the optical resistivity ($\omega = 0$) of Ni from this work on (100) single-crystalline Ni (■) and electrical measurements on poly-crystalline Ni by White and Woods [100] (●), Ni rods from Farrell and Greig [101](▲), and poly-crystalline rod by Laubitz *et. al* [106](▼).

the order of a quarter of the room temperature value [108]. Therefore, it is not possible to separate the temperature dependence of ρ_{e-mag} and ρ_{e-ph} in this region. Figure 5.11 also shows that between 77 K and 250 K, the temperature dependence is proportional to $\sqrt{T}$, which is not consistent with the temperature dependence of any individual contributions to the total resistivity. We do not have any explanation for this behavior at the present. One important point is that since the sample is kept at low temperature for a considerably long time, formation of a very thin layer of ice on the surface of the sample is inevitable. This surface condition of the sample can alter the results taken from ellipsometry measurements, whereas the potentiometric techniques that were employed by Farrell and Greig [101] are more likely to be insensitive to the surface conditions.

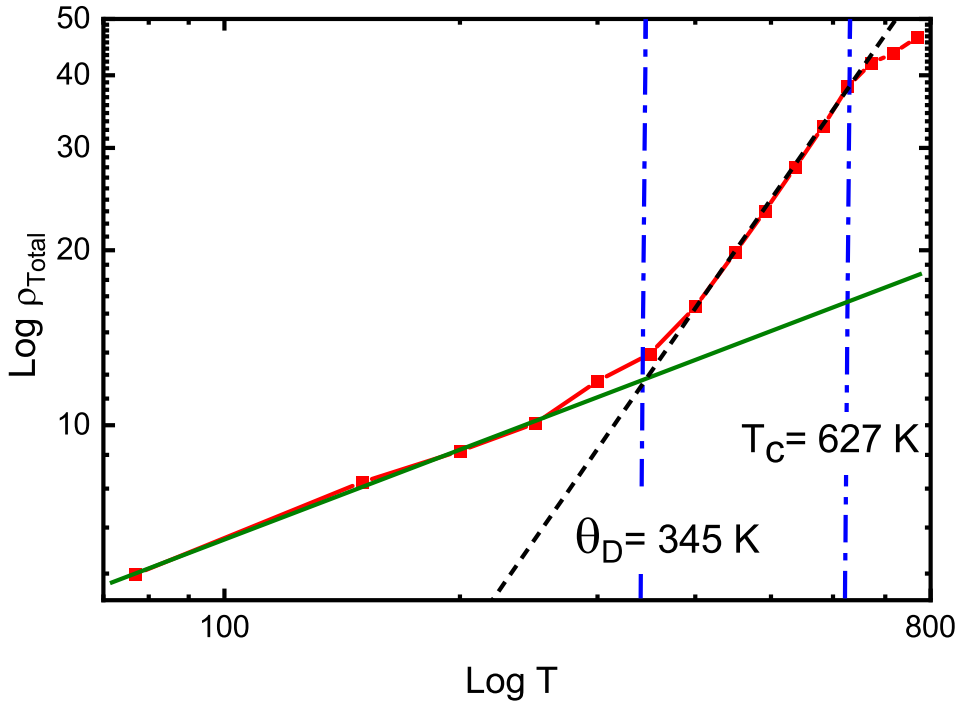

Figure 5.11: Log-log plot of the optical resistivity of Ni at various temperatures. The solid line shows a linear fit to the data below room temperature with a slope of 0.51 ± 0.02. The black dashed line shows a linear fit to the data between Debye temperature θ_D and Curie temperature T_c with a slope of 1.97 ± 0.03.

5.6 Main Peak at 4.8 eV

The main peak in the optical conductivity of Ni has been assigned to ($L_2 \rightarrow L_{1u}$) based on the symmetric shape of the peak and its similarities to the main peak of gold and copper [49]. Stoll and Jung [94], however, have assigned this peak to conduction band to conduction band transitions. Gadenne and Lafait [96] on the other hand, suggested that this peak can be attributed to transitions from the bottom of the d-band in different points of the Brillouin zone as it is more realistic than transitions to states well above E_F that was suggested by Stoll and Jung [94], because the density of states of Ni has a peak slightly above E_F and drops drastically with energy.

Our optical conductivity alone does not provide more information about the origin of the transition resulting in the main peak. However, the temperature dependence of the energy of this peak might shine light on this issue. Figure 5.12 demonstrates the red shift of the energy of this peak as the temperature rises. Shiga and Pells [49] as well as Kirillova *et. al.* [90] report that the energy of this peak decreases linearly with temperature. However, we fitted the red shift of the transition energy to the Bose-Einstein function [91]

$$E(T) = E_a - E_b \left(1 + \frac{2}{\exp(\theta/T) - 1}\right), \tag{141}$$

where $E_a = (4.99 \pm 0.03)$ eV is the unrenormalized transition energy, $E_b = (0.20 \pm 0.04)$ eV is a coupling strength and $k_b\theta$ is an effective energy. We found $\theta = (900 \pm 98)$ K, which is about 77 meV. This value is too large for an optical phonon energy which is about 30 meV [109] but comparable to the magnon energy of about 100 meV at the L-symmetry point [110], indicating that the main peak might be due to transitions at the L-point broad-

ened by magnons. Considering the discussion in the previous part, scattering by magnons results in a change in the direction of the electron (spin-flip). Furthermore, magnon assisted s-d scattering has a substantially higher probability than s-s and d-d scattering. Therefore, one can conclude that the main absorption peak of Ni is due to the transitions from the bottom of the L-point and the peak shifts and broadens as a result of the scattering by magnons.

The discrepancy between Fig. 5.12 and Refs.49 and 90 appears to be due to the smaller temperature step in our experiment. As can be seen in Fig. 5.12, the shift in energy for temperatures above room temperature looks linear. Both Refs.49 and 90 conducted measurements above room temperature and Ref. 49 has only one data point below room temperature which was neglected in their linear fit.

Neutron scattering experiments [111] show the existence of spin waves above T_c. Shiga and Pells [49] measured a poly-crystalline Ni sample and assumed that the main absorption peak consists of two identical peaks in the vicinity of 4.7 eV, representing the transitions of minority and majority electrons from L_2'. Their energy difference is equal to the exchange energy of the d-band ΔE_{ex}^d. They reported this value to be equal to 0.46 eV which was consistent with some theoretical calculations [112]. However, later experimental band structures [113, 114] showed that the exchange energy ΔE_{ex} is of the order of 300 meV and its magnitude and temperature dependence depend on the wave vector [115, 116]. Kirillova *et. al.* [90] conducted ellipsometry measurements on Ni(110). Their data are in good agreement with the data from the poly-crystalline Ni of Shiga and Pells [49]. They further reported that the main absorption peak consists of three small peaks at room temperature and two peaks

at 773 K. They concluded $\Delta E_{ex}^{d} = 0.25$ eV. Different values have been found for the exchange splitting of the d-band. [113, 115, 117, 118] Stoll [77] has reported the exchange energy of the d-band of about (0.55 ± 0.07) eV from optical studies on Ni(110) sample. However, he found this value to be equal to 0.35 eV for poly-crystalline Ni [76]. Stoll and Jung [119] estimated 0.4 eV for the exchange splitting of L_{31}. It has even been shown that the exchange splitting of the d-band has different values at different symmetry points [118]. Our data demonstrates a symmetric peak and does not indicate the existence of the two peaks of Shiga and Pells [49], nor the three peaks of Kirillova *et al.* [90]. Therefore, we modeled the data with only one Lorentzian oscillator at about 4.8 eV. Using two oscillators instead of one results in a high correlation between the oscillators and erroneous energies and broadenings. It also requires one oscillator with a very small amplitude compared to the other one, which is inconsistent with the model proposed by Shiga and Pells [49].

Figure 5.13 shows the broadening of the main absorption peak vs. temperature. This broadening starts from 2.12 eV at 77 K and reduces to 1.81 eV at 770 K. Therefore, it decreases by 0.31 eV. This reduction in broadening resembles the decrease in the reduced spontaneous magnetization (Fig. 5.13). As we could not fit the optical constants with two oscillators at 4.7 eV unambiguously, we believe that the reduction of the broadening of this oscillator, as opposed to the energy difference of two peaks proposed by Shiga and Pells [49], corresponds to ΔE_{ex} at the L-point, which is in a great agreement with Refs. 113 and 117.

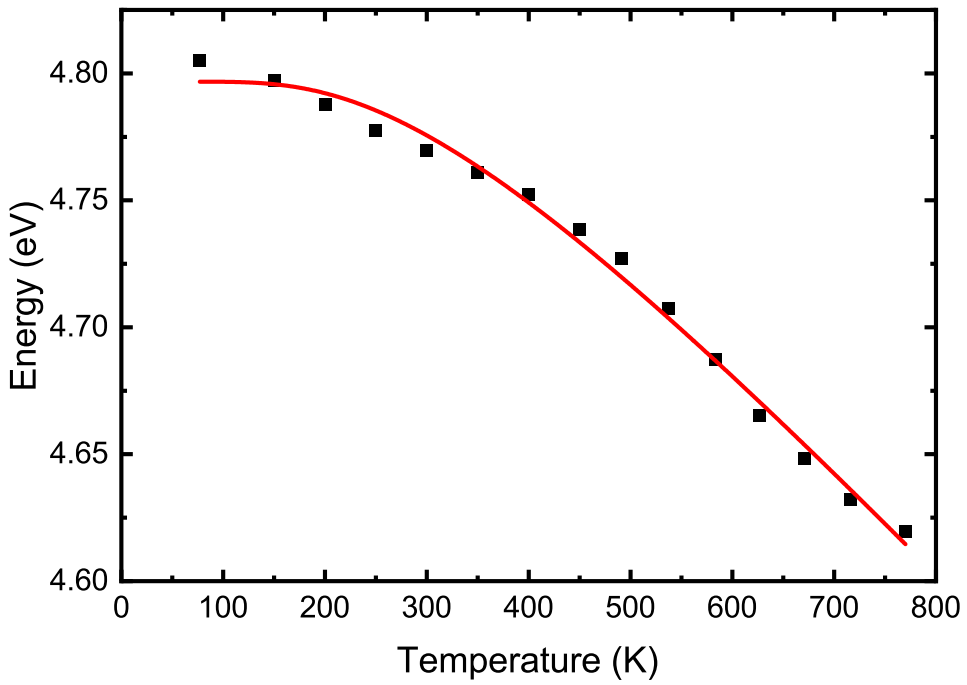

Figure 5.12: Energy of the main absorption peak vs. temperature. Squares: experimental data, solid line: Bose-Einstein fit.

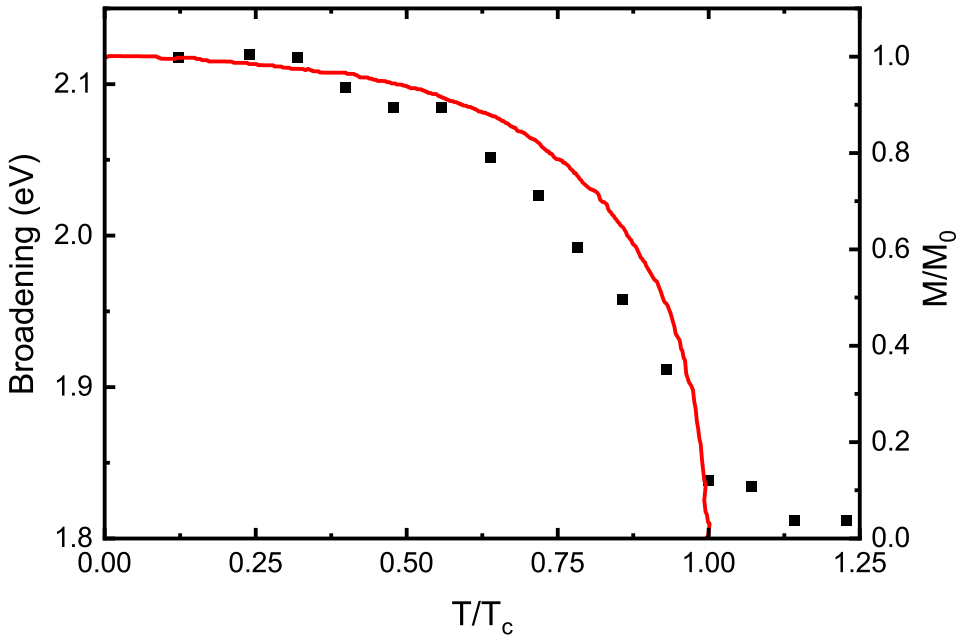

Figure 5.13: Broadening of the main peak at 4.8 eV (■) and reduced spontaneous magnetization from Ref. 49(solid line). The broadening of the main peak decreases with rising temperature and stays constant above T_c. The reduced magnetization is drawn to scale.

5.7 Small Peak at 1.5 eV

Figure 5.3 displays a small structure in the optical conductivity of Ni at about 1.5 eV. It has already been noticed that the separation of the contribution of the interband and intraband absorption to the conductivity of transition metals is not straightforward because a single band model cannot explain the absorption [98]. While this peak has been traditionally assigned to interband transitions at the W-point in the Brillouin zone [49], Stoll and Jung [119] suggest assigning this peak to transitions $L_{31\uparrow} \rightarrow E_{f\uparrow}$, thus estimating an exchange splitting of $\Delta E = 0.4$ eV for L_{31}. They further conclude that the persistence of this peak at higher temperatures indicates that the exchange splitting does not reduce to zero above T_c. They previously assigned this peak to different transitions [94]. The fact that the absorption decreases upon rising temperature and stays constant above T_c suggests assigning this peak to $L_{3\downarrow} \rightarrow L_{3\downarrow}$ transitions. References 118 and 120 show that as the temperature increases, minority (majority) bands go down (up) and they coincide at T_c. Therefore, we believe that as the temperature rises, the minority bands $L_{3\downarrow}$ and $L_{3\downarrow}$ move downward simultaneously as demonstrated in Fig. 5.14, that is why the energy of the peak remains constant. This movement continues until $L_{3\downarrow}$ touches the Fermi level and stays constant at $T > T_c$ as it is described in Refs. 118 and 120. As the bands move downwards, the number of unoccupied states decrease to their minimum at T_c, which explains why the magnitude of the absorption peak decreases with rising temperature and stays constant above T_c. The energy of this peak is also consistent with band calculation by Wang and Callaway [71]. Although our sample is single-crystalline Ni, studies on thin film Ni on Si have pointed out that the peak becomes weaker as the crystal size becomes smaller [96]. This indicates that there are more

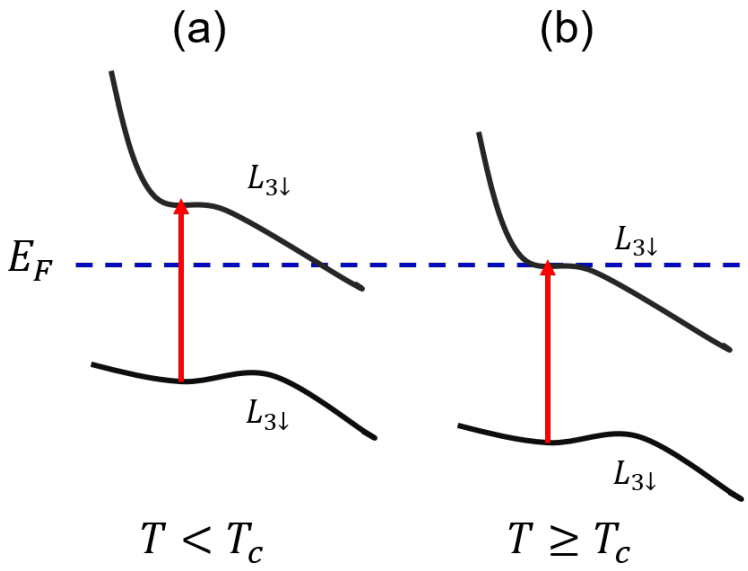

Figure 5.14: Evolution of spin down bands with rising temperature. (a) below T_c, and (b) above T_c.

contributions to the origin of this peak than merely interband transitions.

5.8 Summary

We modeled the optical constants of single-crystalline Ni(100) from 77 K to 770 K. Qualitative agreement is found in the general shape of the resistivity from ellipsometry and electrical measurements. The temperature dependence of the resistivity is proportional to T^2 between θ_D and T_c, and is proportional to $\sqrt{T}$ below room temperature. The energy of the main absorption peak displays a red shift upon rising temperature, which is modeled by a Bose-Einstein function. The fit gives an effective energy of about 77 meV for the transitions at about 4.8 eV, which we interpret as an interband transition scattered by magnons. The broadening of the main peak reduces by 0.31 eV and stays constant above T_c. Therefore, the reduction of the broadening of the peak is interpreted as ΔE_{ex} at the L-point. The temperature dependence of the absorption peak at 1.5 eV is explained by assigning the peak to

$L_{3\downarrow} \rightarrow L_{3\downarrow}$ transition, which explains the decrease in magnitude of the peak and its constant energy.

6 CONCLUSION AND OUTLOOK

6.1 Conclusion

In this work we studied the optical properties of poly-crystalline and single-crystalline Ni at various temperatures from 77 K to 770 K. The dielectric function of Ni was modeled with two Drude and four Lorentz oscillators representing s- and d-electrons and interband transitions, respectively. The temperature dependence of the optical constants shows a typical behavior of metals for s-electrons and a red shift in the main absorption peak of Ni at 4.8 eV. The latter is fitted by a Bose-Einstein factor, which indicates that the interband transitions at 4.8 eV are broadened by scattering with magnons of an energy of 77 meV. The change in the conductivity of Ni at an energy of 1.5 eV reveals that the amplitude of this peak decreases with rising temperature and stays constant above T_c, while its energy stays constant at all temperatures. We assign this peak to $L_{3\downarrow} \rightarrow L_{3\downarrow}$ transitions and explain the constant energy by the simultaneous descent of both $L_{3\downarrow}$ and $L_{3\downarrow}$ bands when the temperature increases.

6.2 Outlook

Ferromagnetic properties of Ni make this element suitable in research and application aspects. The temperature dependent optical properties of thin films of Ni as a function of thickness and the anomalous skin effect can be the next step in the optical characterization of Ni. Research on NiPt alloys or other alloys of Ni would provide a deeper insight into the optical properties of this element and its alloys because the Curie temperature can be tuned by the composition. Furthermore, studying optical properties of single-crystalline Ni with different surface orientation in a magnetic field and using the MM formalism is expected to

reveal many collective excitations in the off-diagonal blocks of the MM. In particular, single-crystalline Ni (111) is expected to show special structures due to the fact that the preferred magnetic orientation of single-crystalline Ni is along its body diagonal. A comprehensive dielectric function to describe both diagonal and off-diagonal elements of the dielectric tensor is yet to be proposed. Comparison of other ferromagnetic metals like Fe, Gd, and Co as well as non-magnetic metals like Al, Ag, and Au can provide a broader understanding about the optical constants of metals.

APPENDIX A

Merging the FTIR-VASE and the VASE data

A.1 Introduction

Well-calibrated spectroscopic ellipsometers based on rotating elements (polarizer, analyzer, compensator) or phase modulators provide very accurate measurements of the ellipsometric angles ψ and Δ, which can be analyzed to determine the thickness and properties of thin layers or to study the vibrational and electronic properties of materials [12, 16–18]. An instrument calibration [19–23] determines the azimuthal angles of the optical elements with respect to the plane of incidence, the modulation amplitude or phase retardance of the modulator or compensator as a function of photon energy, and the optical activity [19] of various components. Measurement configurations for calibration include straight-through measurements without a sample [24] ($\psi = 45°$, $\Delta = 0$), oblique reflection ellipsometry of a calibration sample [21] (usually Si with a thin oxide layer of about 30 nm thickness, where precise knowledge of the thickness is not required), or normal-incidence reflection from an isotropic sample. In a straight-through measurement, a typical accuracy of $\delta\psi = 0.01°$ and $\delta\Delta = 0.1°$ can be achieved over most of the spectral range [24].

Broadband ellipsometry measurements over a wide spectral range, for example from the mid-infrared to the deep ultraviolet, require the use of two or more ellipsometers. Data need

to be merged, resulting in overlapping spectral regions, where data from two instruments exist. If the ellipsometers are well calibrated and measurements are performed in air, nearly perfect overlap can be achieved. See Fig. A.1(a) as an example of a measurement in air from 190 nm to 25 μm on a bulk Ni (100) single crystal covered with a thin surface layer (probably water [46] or a similar volatile liquid), using FTIR-VASE and VASE ellipsometers from the J.A. Woollam Company.

Even well-calibrated ellipsometers suffer from systematic errors [25–29] due to the misalignment and optical activity of the optical components and the strain-induced birefrigence of windows [30] (if the sample is located in a vacuum or environmental chamber during the measurement). Some of these systematic errors need to be considered during instrument calibration [19, 21]. A good summary of various sources of ellipsometry errors and their influence on the ellipsometric angles was given by de Nijs and van Silfhout [28]. To first order, most errors are odd functions of the polarizer angle P. Therefore, two-zone measurements (with positive and negative P) can eliminate most first-order errors [29].

It is well known [28] that errors due to birefringent windows can not even be eliminated to first order with a two-zone measurement. Therefore, the effects of window birefringence need to be determined from measurements of a calibration sample, which are stored as instrument parameters with the system configuration and other calibration parameters. This technique works quite well for measurements on a single instrument, but we found that issues arise in the region of overlap, when data from two instruments are merged, see Fig. A.1(b). The mismatch is especially large, if the measured sample (here a bulk Ni crystal with a high conductivity) is very different from the calibration sample (usually Si with a thin thermal oxide) used to determine the window parameters. The goal of this work is to describe a

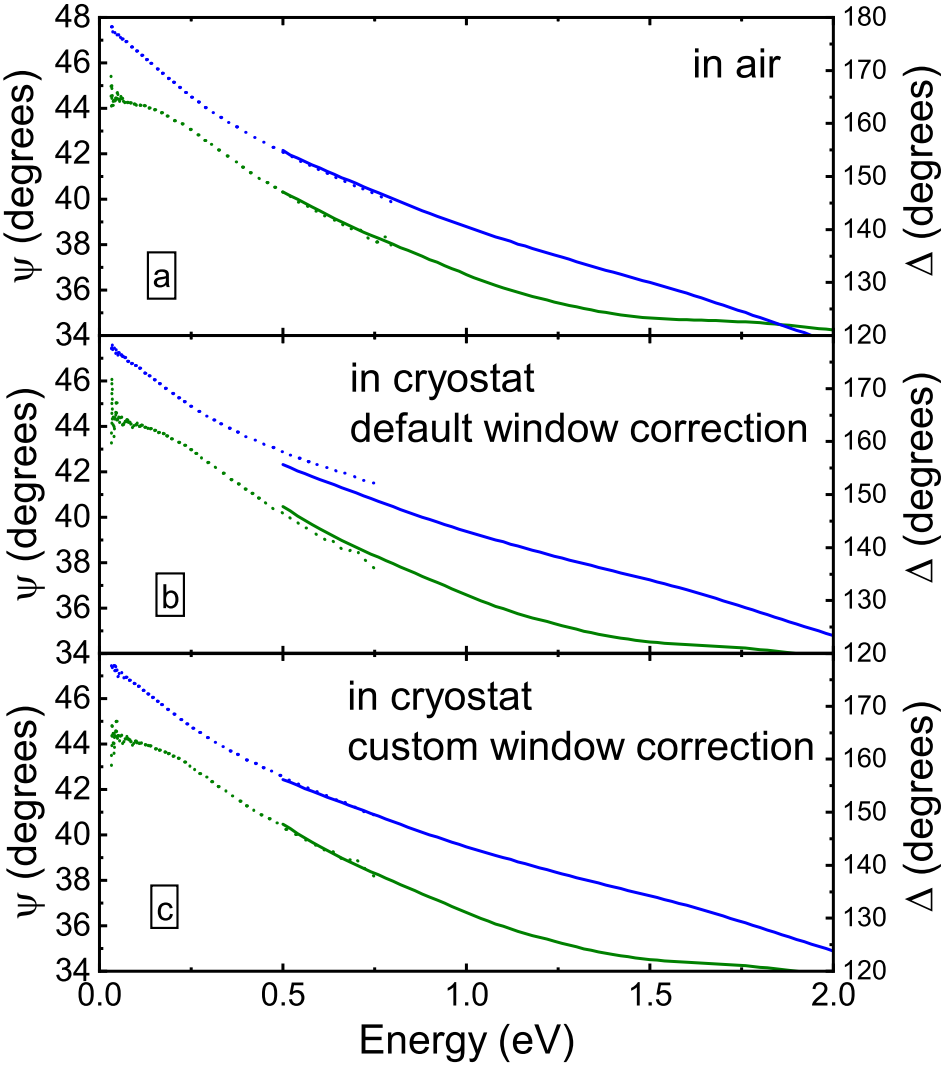

Figure A.1: (a) Ellipsometric angles ψ (green) and Δ (blue) of a Ni (100) single crystal in air at 300 K, measured at 70° angle of incidence over a broad spectral region with two ellipsometers, a J. A. Woollam FTIR-VASE (dotted) and a VASE (solid). (b) Same Ni sample, but measured in two cryostats with diamond and quartz windows for the infrared and VIS/UV spectral regions, using the default window corrections obtained from a Si calibration sample. (c) Same data, but with custom window corrections for this specific sample, as described in the text.

secondary "custom" sample-dependent correction technique, which results in a good overlap of the data taken on two different ellipsometers.

A.2 Window Effects in Ellipsometry

A.2.1 Small-Retardance Approximation

Window effects in ellipsometry measurements have been studied by many investigators. While it is possible to reduce window errors by special mounting procedures to lower the strain [30, 31], windows usually disturb the polarization in measurable ways. Windows have historically [25] been considered as ideal linear wave-plate retarders and described by two parameters, the azimuth θ_w of the fast axis and the retardance δ_w. The Mueller matrix for such windows to first order in δ_w is [25, 32, 33]

$$M_w = \begin{pmatrix} 1 & 0 & 0 & 0 \\ 0 & 1 & 0 & -S_w \\ 0 & 0 & 1 & C_w \\ 0 & S_w & -C_w & 1 \end{pmatrix}, \tag{A1}$$

where $S_w{=}\delta_w \sin(2\theta_w)$ and $C_w{=}\delta_w \cos(2\theta_w)$. The corresponding Jones matrix is [12]

$$J_w = \exp\left(-\tfrac{i}{2}\delta_w\right) \begin{pmatrix} 1+\frac{i}{2}C_w & \frac{i}{2}S_w \\ \frac{i}{2}S_w & 1-\frac{i}{2}C_w \end{pmatrix}. \tag{A2}$$

The resulting errors of the ellipsometric angles from the entrance window within the small retardance approximation for a rotating analyzer ellipsometer without compensator are [21, 28]

$$\delta\psi = S_w \frac{\sin 2\psi}{2\sin 2P} \quad \text{and} \quad \delta\Delta = C_w - S_w \cot 2P. \tag{A3}$$

The corresponding errors from the exit window are [28]

$$\delta\psi = S_w \frac{\sin\Delta}{2\sin 2P}\left(1 - \cos 2P\cos 2\psi\right) \quad \text{and} \tag{A4}$$

$$\delta\Delta = C_w + S_w \frac{\cos\Delta\left(\cos 2\psi - \cos 2P\right)}{\sin 2\psi \sin 2P}. \tag{A5}$$

If the fast retarder axis of the window is in the plane of incidence ($\theta_w = S_w$=0), then the error $\delta\psi$ vanishes and $\delta\Delta = C_w$. Similarly, if the fast retarder axis is oriented at 45° relative to the plane of incidence, then $C_w = 0$.

If an instrument has both an entrance window (with parameters S_w and C_w) and an exit window (with parameters S'_w and C'_w), then the combined effect of both windows [22] will depend on three parameters S_w, S'_w, and $C_w + C'_w$. These parameters are typically on the order of 3×10^{-3} rad (0.2°) for low-strain BOMCO windows [30] or fused silica lenses [32] and an order of magnitude larger for regular quartz vacuum windows. [30, 34] A rotating analyzer ellipsometer without compensator measures only two Fourier coefficients, which is not sufficient to determine these three window parameters plus the unknown ellipsometric angles of the sample [32]. The problem can be solved by adding a compensator, which provides access to the fourth column or row of the Mueller matrix.

It is apparent from Eqs. (A3-A5) that the window errors from a two-zone measurement are $\delta\psi \approx 0$ (because $\delta\psi$ is an odd function of P) and $\delta\Delta \approx C_w$. Within the small retardance approximation, the main effect of windows is to cause a Δ-offset, which depends on the photon energy E through a modified Cauchy dispersion [22, 32, 34]

$$C_w = E\left(C_{w0} + C_{w2}E^2 + C_{w4}E^4\right). \tag{A6}$$

Our results in Fig. A.1(b) show errors in both ψ and Δ and therefore this framework cannot be adequate.

A.2.2 Large-Retardance Approaches

Several options have been proposed to extend this formalism and relax the small-retardance requirement: Jin and Kondoh [35] employ the precise Mueller matrix for an ideal retarder [12, 36] (for arbitary θ_w) and measure the complete Mueller matrix for an isotropic non-depolarizing sample (Si substrate) in a chamber with windows on a dual rotating-compensator ellipsometer. They then deduce the azimuth and retardance parameters of both windows from the first row and column of the Mueller matrix. Once the window parameters have been determined, measurements of more complex (anisotropic) samples can be corrected for window effects [37]. They also discuss how to average errors caused by inhomogeneous windows, where only infinitesimal regions of the windows can be treated as ideal retarders [37].

Azzam and Bashara [26] take a different approach altogether. They start with the general form of the normalized Jones matrix, which has three complex transmittance parameters. These parameters and their influence on the ellipsometric angles were determined with a four-zone measurement on a nulling ellipsometer. The off-diagonal Jones matrix elements are usually small and may even vanish for some window materials [38].

Johs and Herzinger [34] realized that the complete Mueller matrix M_{WSW} for a sample with entrance and exit windows [35] for arbitrary retardation (which is given, for example, by Jin and Kondoh [35]) can be simplified greatly if the fast retarder axes of the windows are located in the plane of incidence (which they call "in-the-plane") or at 45° relative to the plane of incidence (which they call "out-of-the-plane"). The corresponding Mueller matrices

for a single window in these two special cases are [12]

$$M_{\parallel} = \begin{pmatrix} 1 & 0 & 0 & 0 \\ 0 & 1 & 0 & 0 \\ 0 & 0 & \cos\delta_{\parallel} & \sin\delta_{\parallel} \\ 0 & 0 & -\sin\delta_{\parallel} & \cos\delta_{\parallel} \end{pmatrix} \tag{A7}$$

and

$$M_{\perp} = \begin{pmatrix} 1 & 0 & 0 & 0 \\ 0 & \cos\delta_{\perp} & 0 & \sin\delta_{\perp} \\ 0 & 0 & 1 & 0 \\ 0 & -\sin\delta_{\perp} & 0 & \cos\delta_{\perp} \end{pmatrix}, \tag{A8}$$

where the $\parallel$ and $\perp$ subscripts indicate the "in-the-plane" and "out-of-the-plane" cases, respectively. Instead of using the usual two parameters θ and δ for an ideal retarder, Johs and Herzinger [34] describe windows with in-plane and out-of-plane parameters $\delta_{\parallel}$ and $\delta_{\perp}$. These parameters $\delta_{\parallel}$ and $\delta_{\perp}$ are used to parameterize window effects in the WVASE software of the J. A. Woollam Company. The functional relationship between $\delta_{\parallel}$ and $\delta_{\perp}$ on the one hand and azimuth θ and retardance δ on the other hand was not described. The dispersion of the in-plane and out-of-plane retardance parameters is given by a Cauchy-like expression similar to Eq. (A6).

A.3 Experimental Procedure and Results

A bulk Ni single crystal with (100) surface orientation was obtained commercially (MTI Corporation, Richmond, CA). The ellipsometric angles were measured from 190 nm to 25 μm (0.03 to 6.6 eV) at 70° angle of incidence in air on two different instruments, an FTIR-VASE and a VASE from the J. A. Woollam Company (Lincoln, NE). Detailed experimental methods were described previously [82]. Both instruments were calibrated for measurements in air using the manufacturer's proprietary method to achieve optimal performance. The ellipsometric angles ψ and Δ for this sample are shown from 0.03 to 2.0 eV in Fig. A.1(a).

Good agrement was achieved in the area of overlap of both instruments (between 0.5 and 0.7 eV).

Measurements in vacuum were performed in Janis ST-400 cryostats (Woburn, MA) equipped with standard fused silica UHV viewports for VASE measurements and with diamond windows (Diamond Materials, Freiburg, Germany) for FTIR-VASE measurements. The diamond windows were 0.5 mm thick and had a diameter of 24 mm (with a clear aperture of 20 mm diameter). They were mounted on a Conflat CF40 UHV flange and achieved a good vacuum seal with a base pressure of 10^{-8} Torr. To avoid multiple reflections of the light beam during ellipsometry measurements, the windows made a 3° angle relative to the incident beam. This causes different transmission coefficients for the s- and p-polarized incident beams.

For both types of windows (fused silica and diamond), the in-plane and out-of-plane retardance values and their dispersion were determined using a windows correction procedure developed by the J. A. Woollam Company using a Si calibration sample with a thin thermal oxide. Compare Eqs. (A7), (A8), and (A6). These window parameters were then stored with the instrument configuration on the data acquisition computer. Measurements of other samples were then automatically corrected with these stored window parameters. Especially on the VASE instrument in the near-IR to deep UV region, we usually find good agreement between the results of a measurement in air and in the cryostat with fused quartz windows. We call this window calibration the "default window correction", because it uses the same window correction parameters for all subsequent measurements.

The results for our Ni sample in UHV using this "default window correction" are shown in Fig. A.1(b). The agreement from both instruments, the FTIR-VASE with diamond windows

and the VASE with fused silica windows, is not very good. The differences of ψ and Δ for both datasets in the region of overlap between 0.5 and 0.7 eV are on the order of 0.3° and 2.2°, respectively, much larger than typical systematic errors for measurements in air, compare Fig. A.1(a). Most likely, the window effects on one or both of the instruments depend not only on the window parameters, but also on the ellipsometric angles of the sample. Our Ni sample has a large value of Δ (typically near 180° for a metal) and a value of ψ near 45°. Especially the ellipsometric angle ψ is very different for a Si calibration sample with a thin native oxide, where $\psi \approx 8°$ and $\Delta \approx 145°$ near 0.6 eV.

A.4 Sample-Dependent Window Correction

The following figures explains how the costume window correction for merging the data taken from the FTIR-VASE and the VASE is performed.

Problem statement: Merge correction

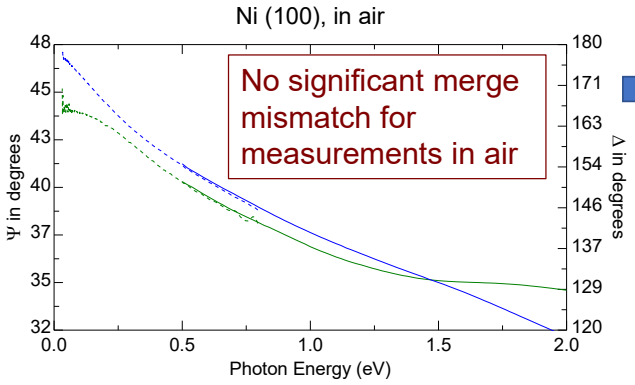

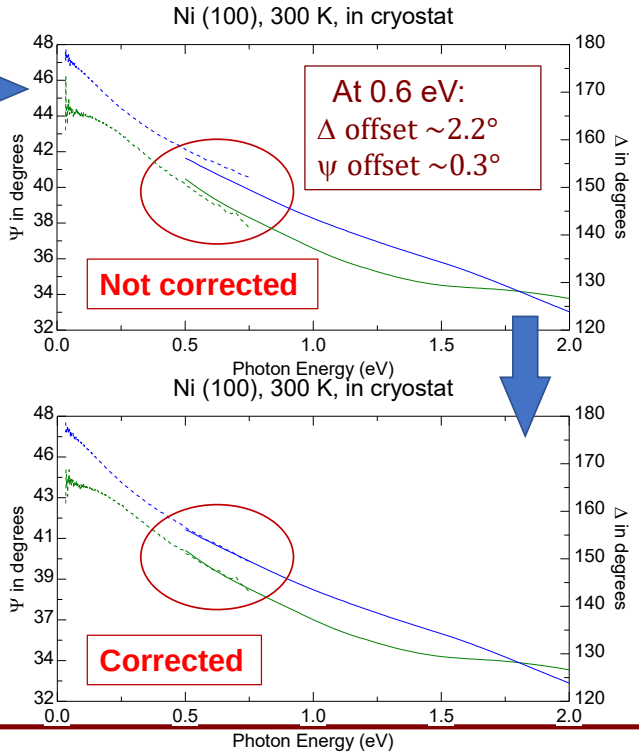

As the sample is mounted in the cryostat, there is a mismatch when merging psi and Delta taken from VASE and FTIR-VASE instruments. This mismatch can be eliminated by a window effects correction described here.

Assumptions

There are some assumptions in the merge correction procedure:

1. We need to decide whether the VASE data should be corrected with respect to the FTIR data or the other way around. In what follows, I assumed that the VASE data are correct, and the merging problem comes from FTIR range. Therefore, I correct the FTIR-VASE data so that it merges with VASE data.
2. The window correction for the VASE is much more established and therefore more likely to be correct than the FTIR-VASE window correction.
3. Depolarization in the FTIR-VASE data is neglected because it exists in measurements in air as well as in the cryostat.
4. Neither VASE nor FTIR-VASE data need to be cut (spectral range).

Procedure

1. Open a VASE experimental file (dat file).
2. Click Alt+2 to open another window (window 2). Open the FTIR-VASE experimental data (same temperature).

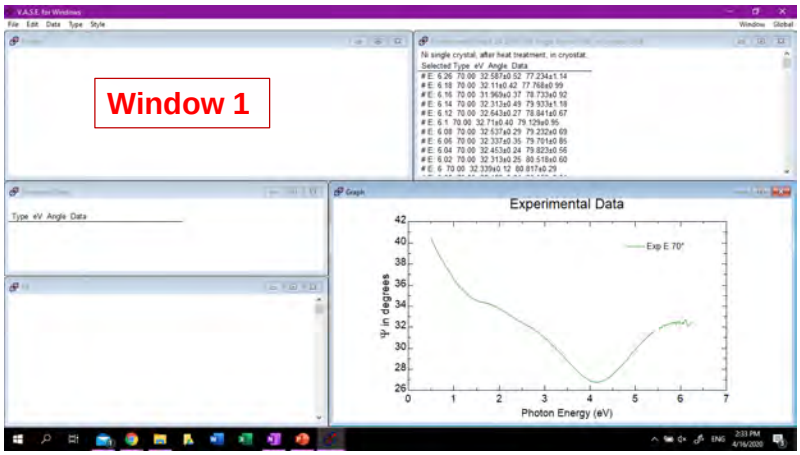

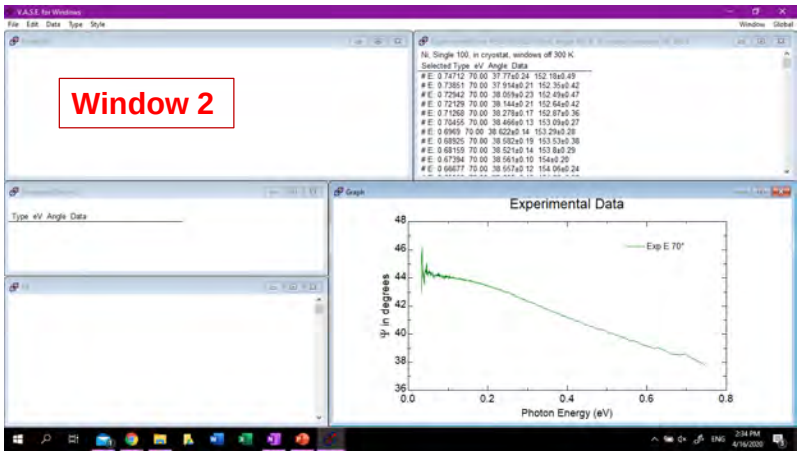

3. Add a model layer in window 1. We use a model previously established for Ni at room temperature (Abadizaman, JVST B **37**, 062920, 2019).

4. Add the same model layer in window 2 and couple with the model in window 1 (click ‘yes’ when it asks if you would like to couple with existing layer).

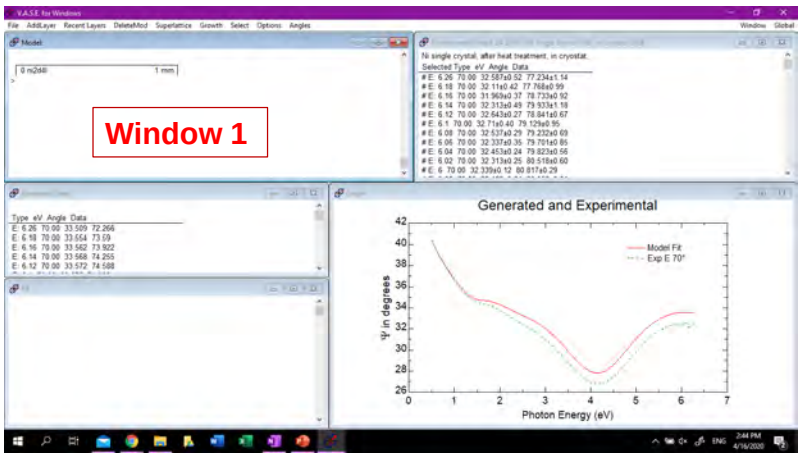

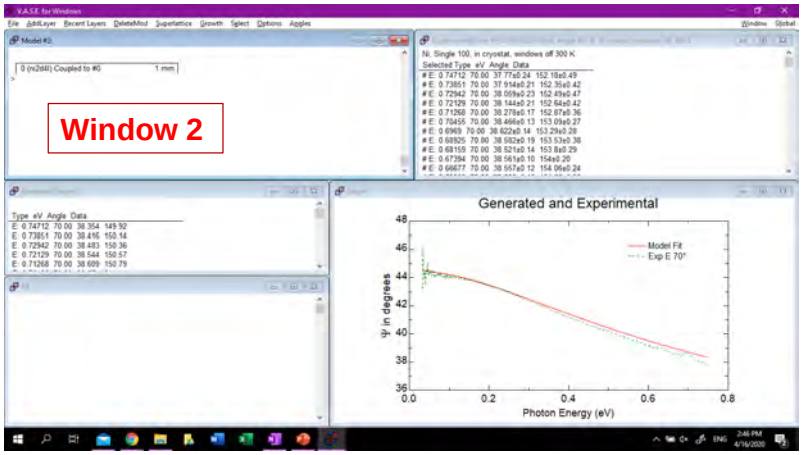

5. Click on the model window, then click on ‘Select’. Then check both models #1 and #2 in “Active in fit”, then click ‘Ok’.

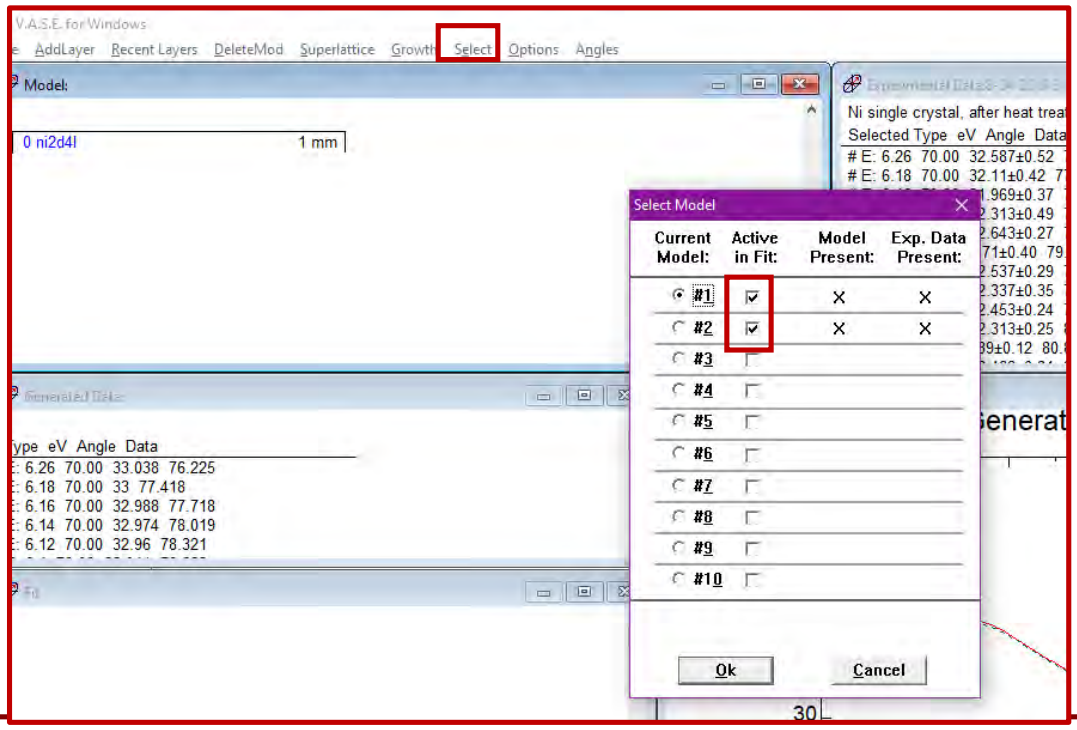

6. Go to window 1 and click on the model. Check all oscillators to fit. This will fit the model parameters to the data in both regions (with existing window parameters).

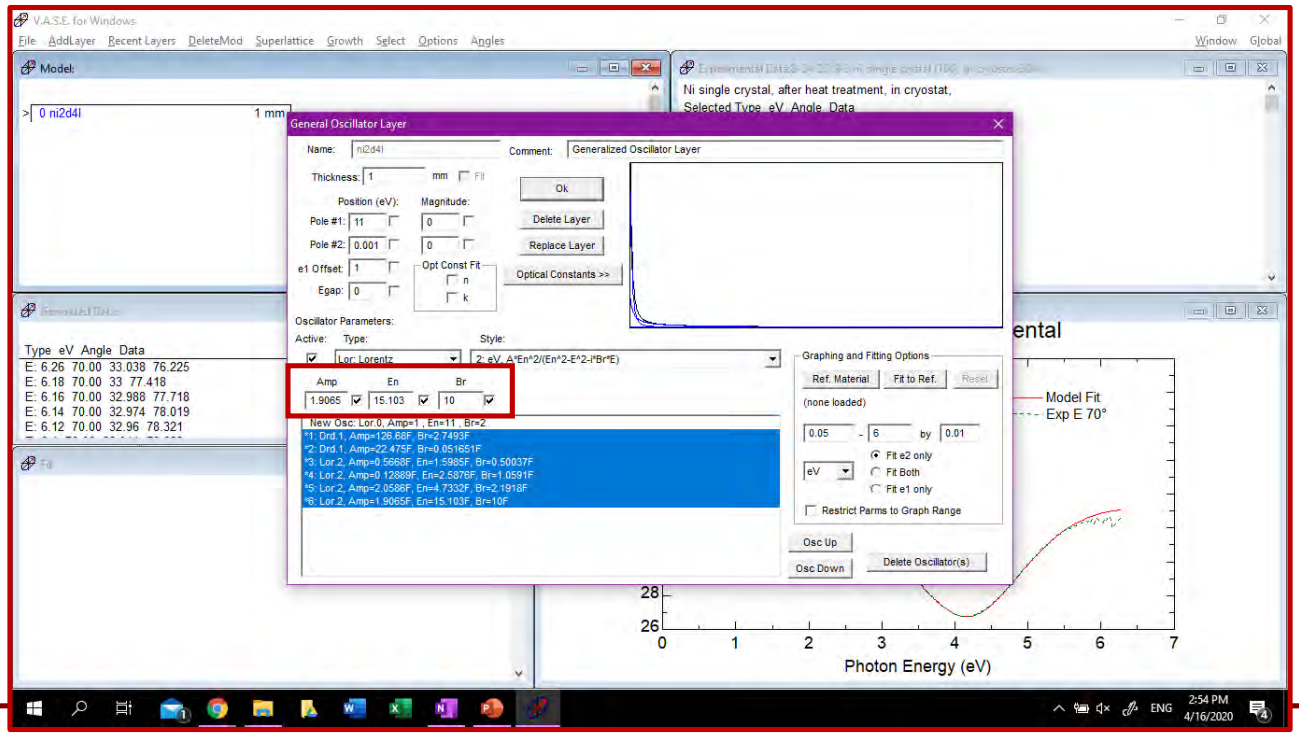

7. Go to window 2. Then click on the model window and choose ‘Options’.

8. Click on ‘Window Effects’. This will adjust the window parameters in the IR region to give a good fit to the data in both regions with the oscillator parameters defined in step 6.

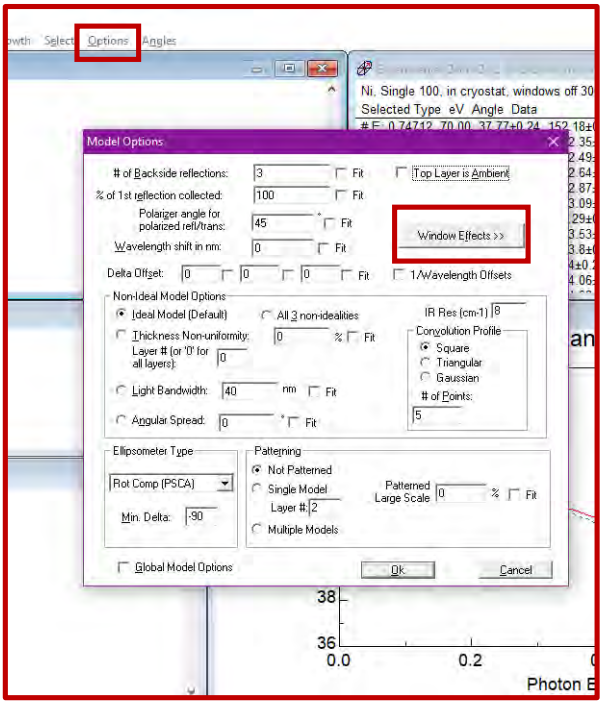

9. Check the boxes as shown in the picture. In some situations (for example as the temperature rises), one might need to fit the retardance or Delta offset dispersion. See the appendix slides.
Then click ok. Click ok in the next window as well. 'Ctrl+F' to fit all parameters (oscillator model and window effects).

- The out-of-plane exit window retardance mostly affects psi and corrects the mismatch of psi.
- The entrance window out-of-plane retardance does not need to be fitted because the IR measurement is performed with the source side polarizer fixed at 45 degrees. This ensures that the out-of-plane component does not affect psi and Delta as light passes through the entrance window.
- Only the exit window out-of-plane retardance is fitted (a constant and a term proportional to the square of the photon energy). We will show later that a constant is often sufficient to give a good fit.
- The in-plane window retardance is the Delta mismatch problem. The first parameter is a constant, the next two parameters depend on photon energy.

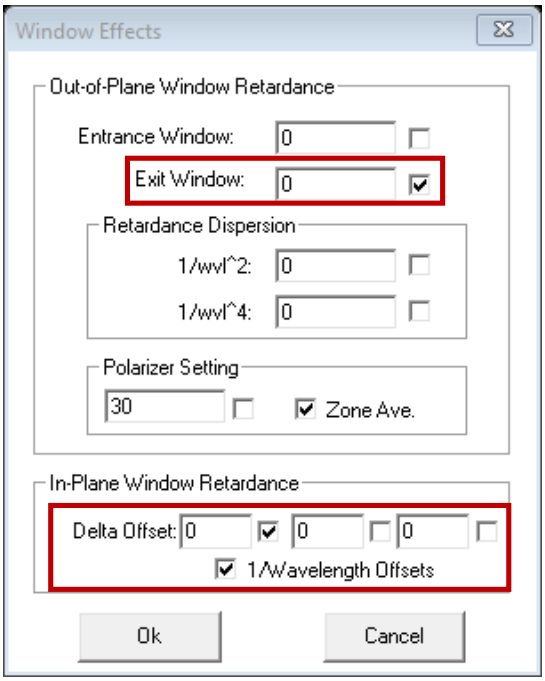

Now one gets a very good fit in both windows.

Parameters: Oscillator parameters in the model and IR window parameters.

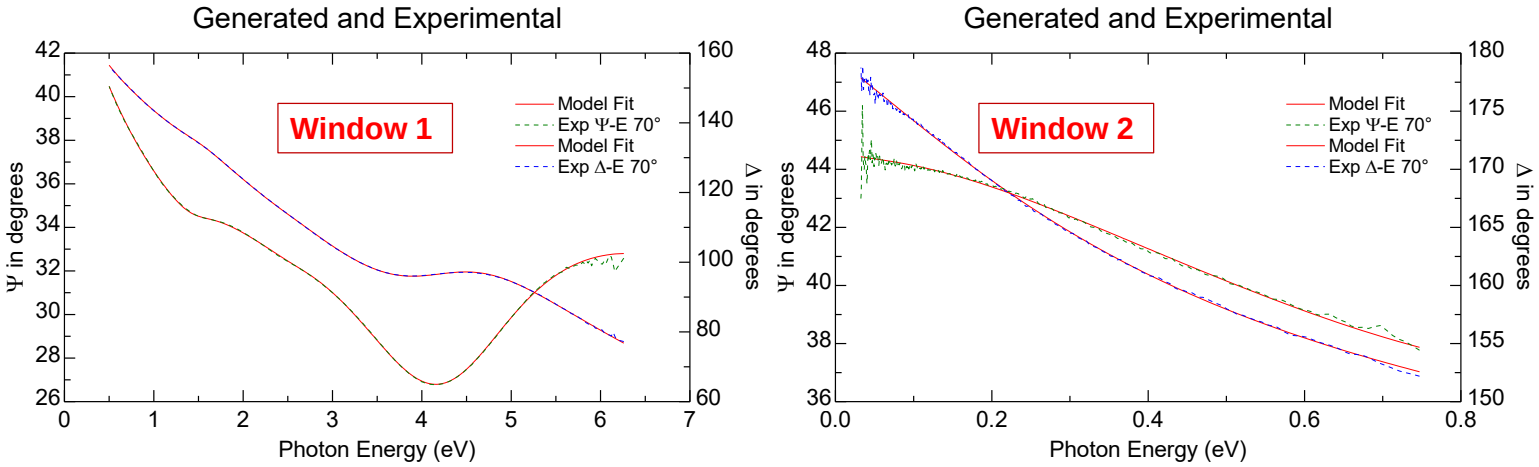

This is a trick and **we are not done yet**.

What is happening here is that the model parameters are fitted to the VASE and FTIR-VASE data, while window effects are fitted only to the FTIR-VASE data. However, without IR window parameter fitting one gets a poor fit in both windows. Slide 16 shows a model without IR window effects fitting.

10. Now that we found the IR window effects parameters, go to window 2 and click on options. Then uncheck all the window effects parameters that were fitted, so that they are now fixed. Then click ok. Click ok in the next window as well.

Do NOT uncheck this one. Otherwise it does not apply the window effects as 1/wavelength.

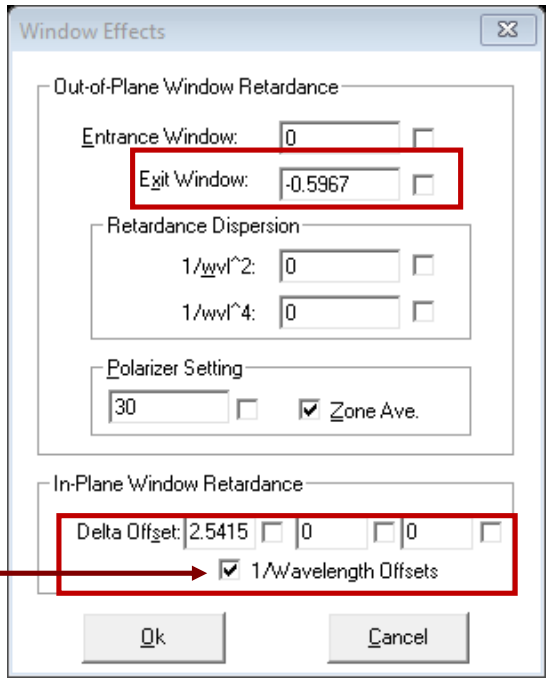

At this point, we are going to do a point by point fit.

11. Go to window 1 and uncheck all fit parameters in your model. Then check n and k to perform a point by point fit. Click ok.

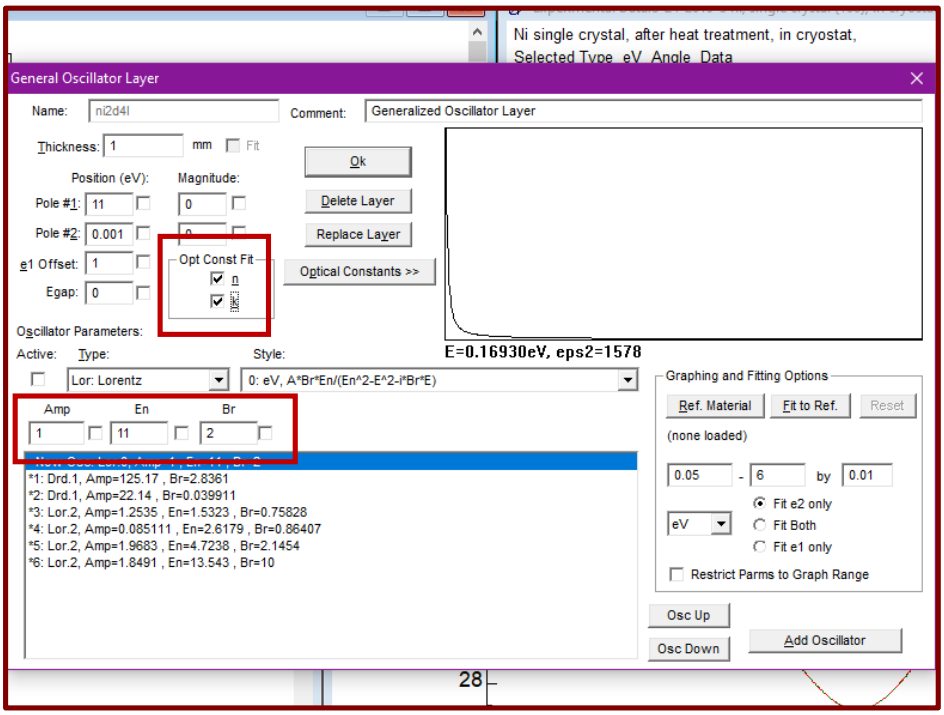

12. Go to window 2 and perform a point by point fit.

It is important to know that at this stage, the point by point fit is done while the IR window corrections determined in step 9 are applied to the model.

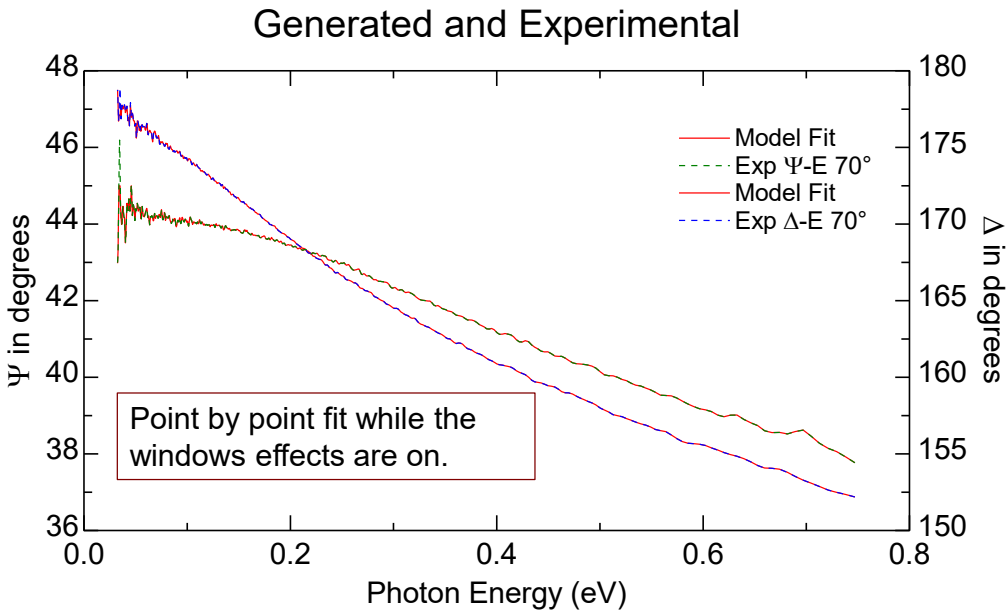

12. While in window 2, click on the model window and go to options. Then set all window effects parameters to zero and uncheck 1/wavelength so that the window effects are turned off.

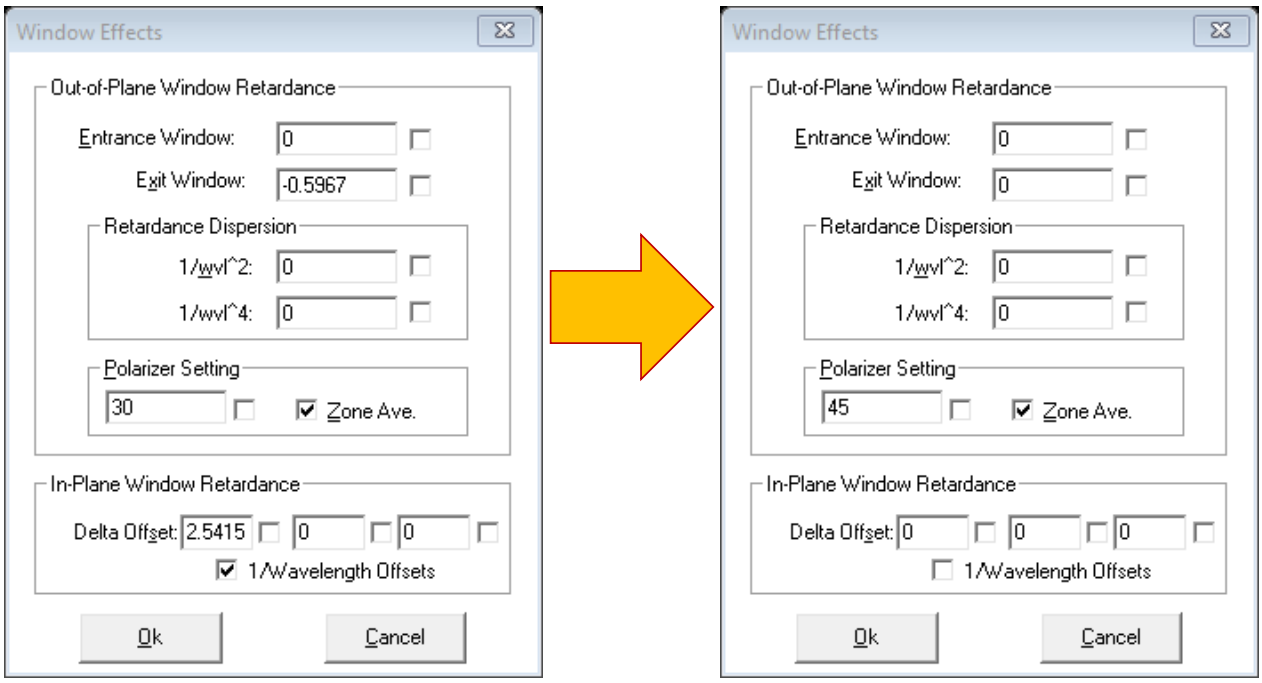

13. Click ok and click ok in the next window as well.

While in window 2, generate data (ctrl+G). Then click on the generated data window and save the generated data (right click > file > save Gen.file). Only save the FTIR-VASE generated data.

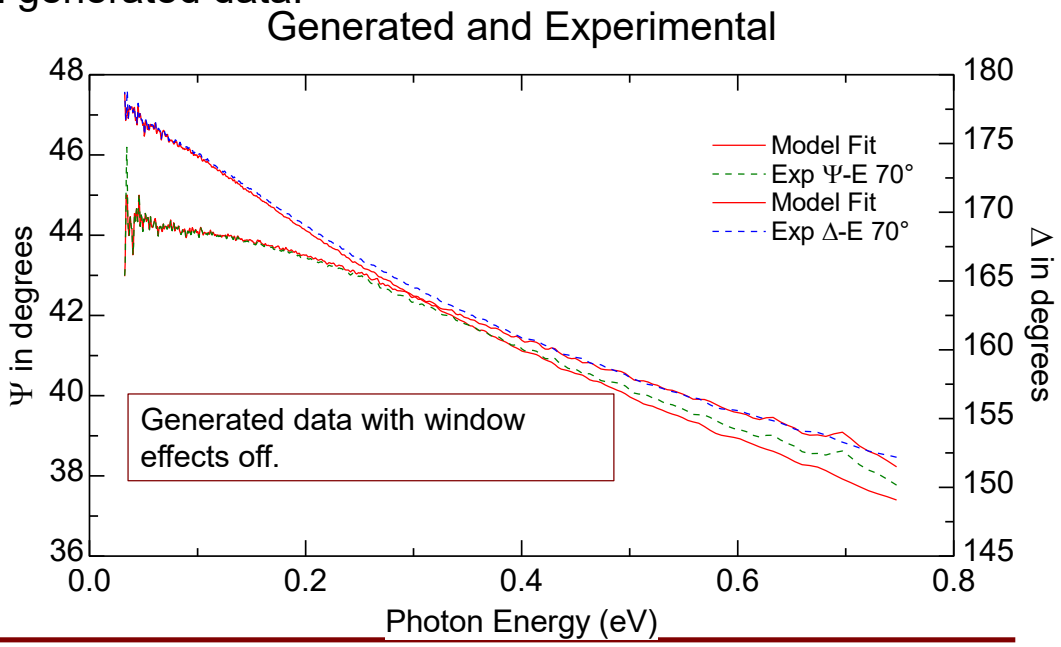

We are done with merge correction. Now we can use the saved generated FTIR-VASE data as the corrected experimental FTIR-VASE data and merge/append them to the VASE data.
The dashed lines in the left graph below show the corrected data.

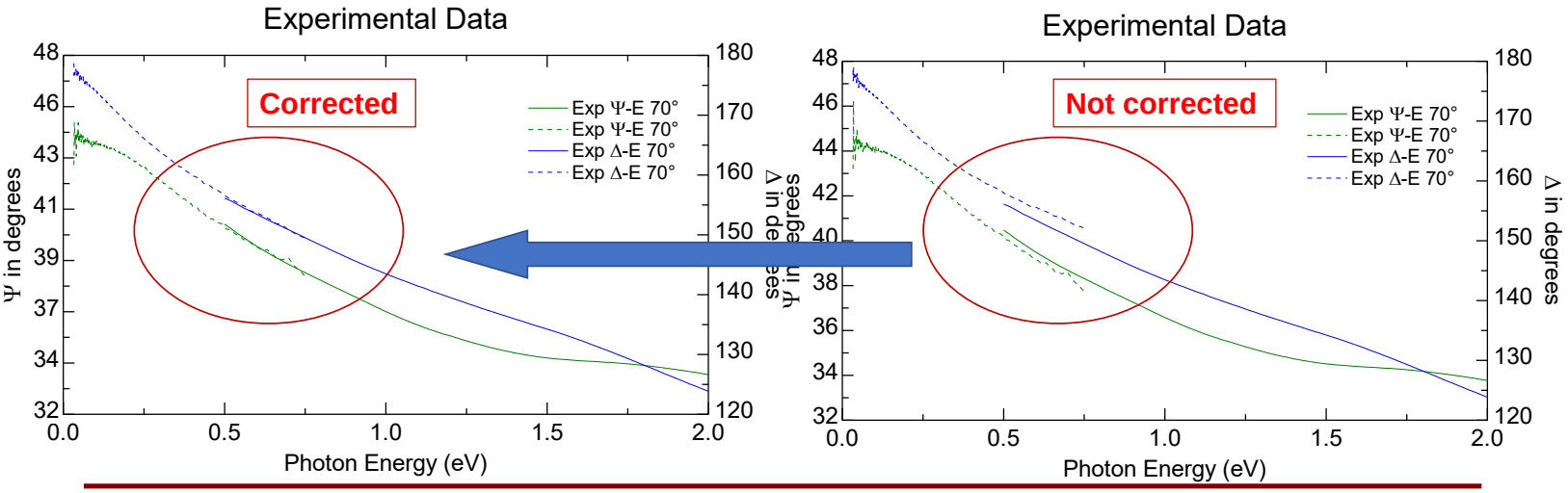

Without window effects fitting.
Only oscillator parameters are fitted.
The fit is poor in both spectral regions.

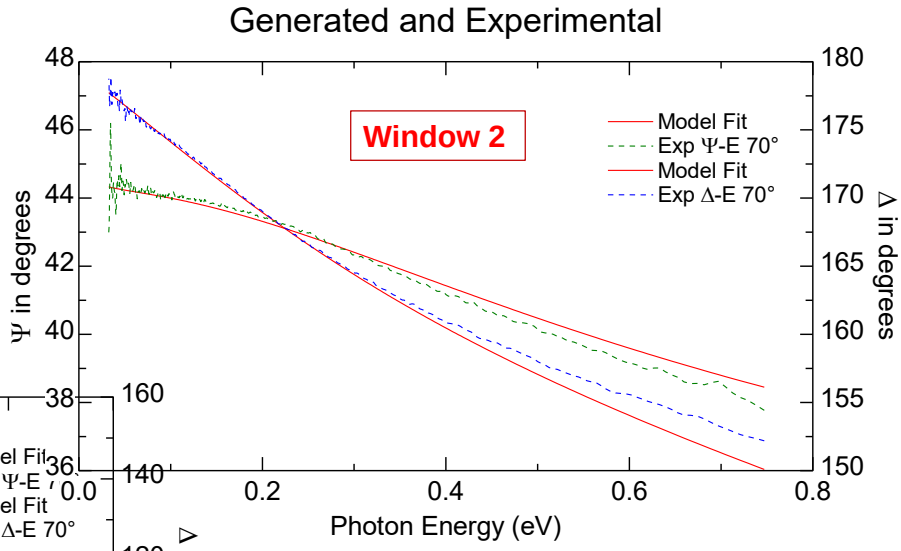

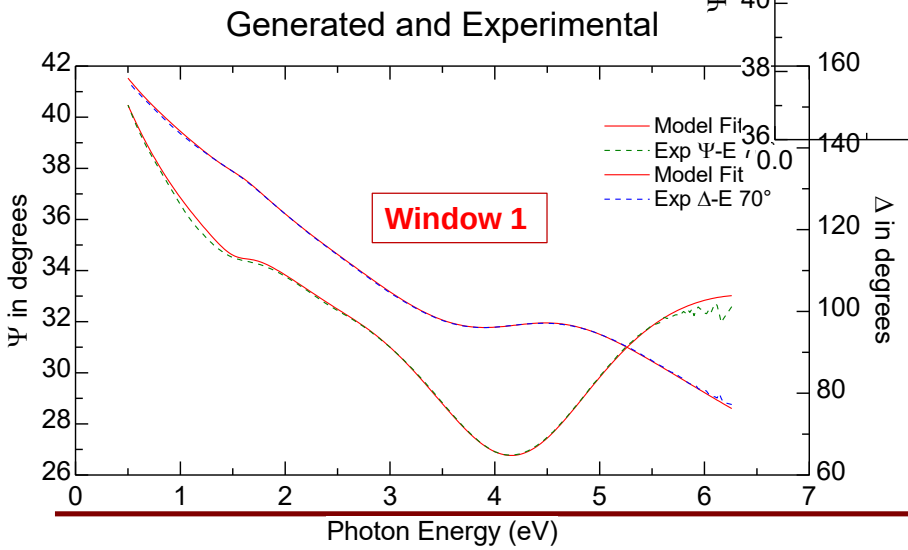

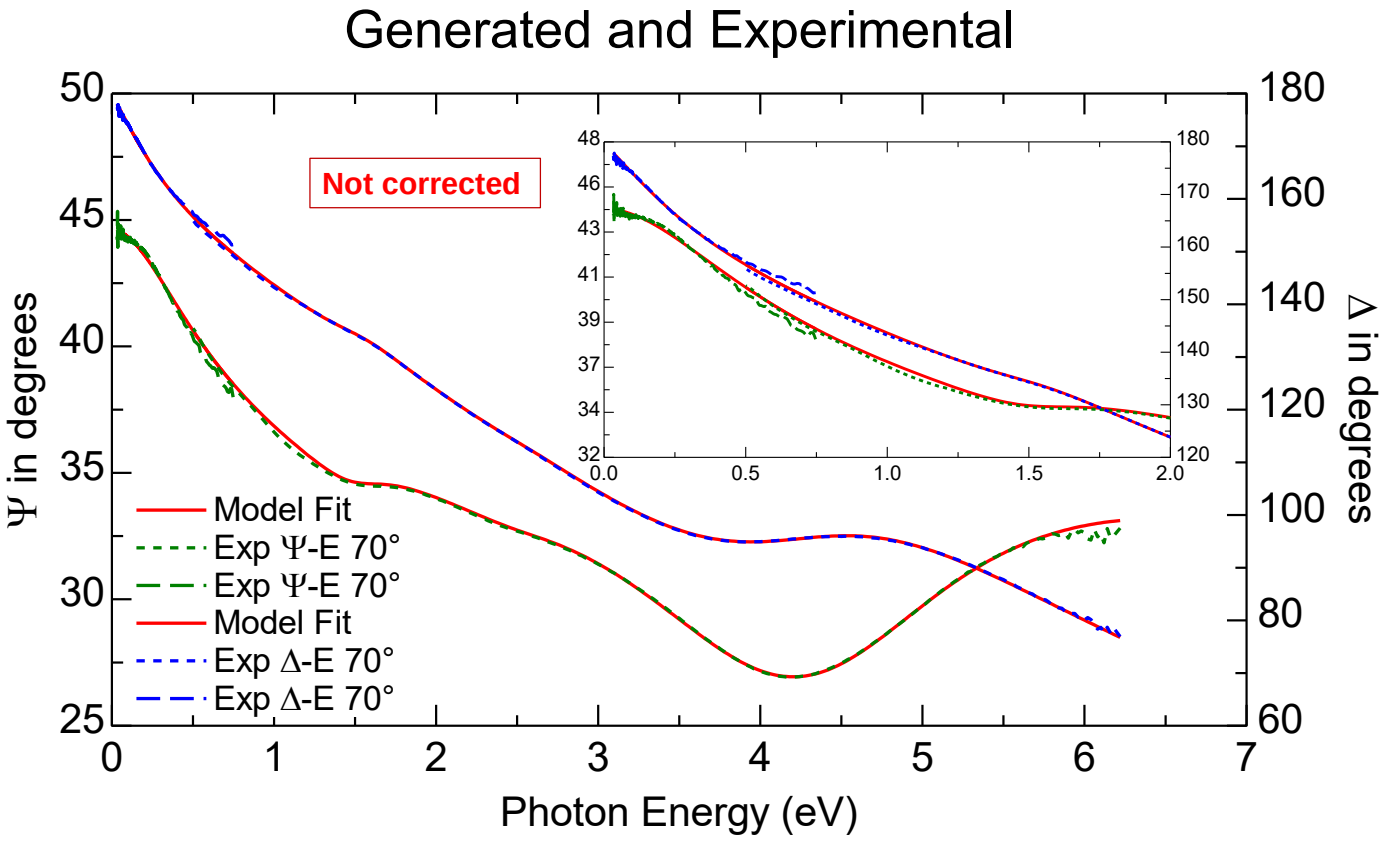
Generated and Experimental
Not corrected
Ψ in degrees
Δ in degrees
Photon Energy (eV)
Model Fit
Exp Ψ-E 70°
Exp Ψ-E 70°
Model Fit
Exp Δ-E 70°
Exp Δ-E 70°

Generated and Experimental

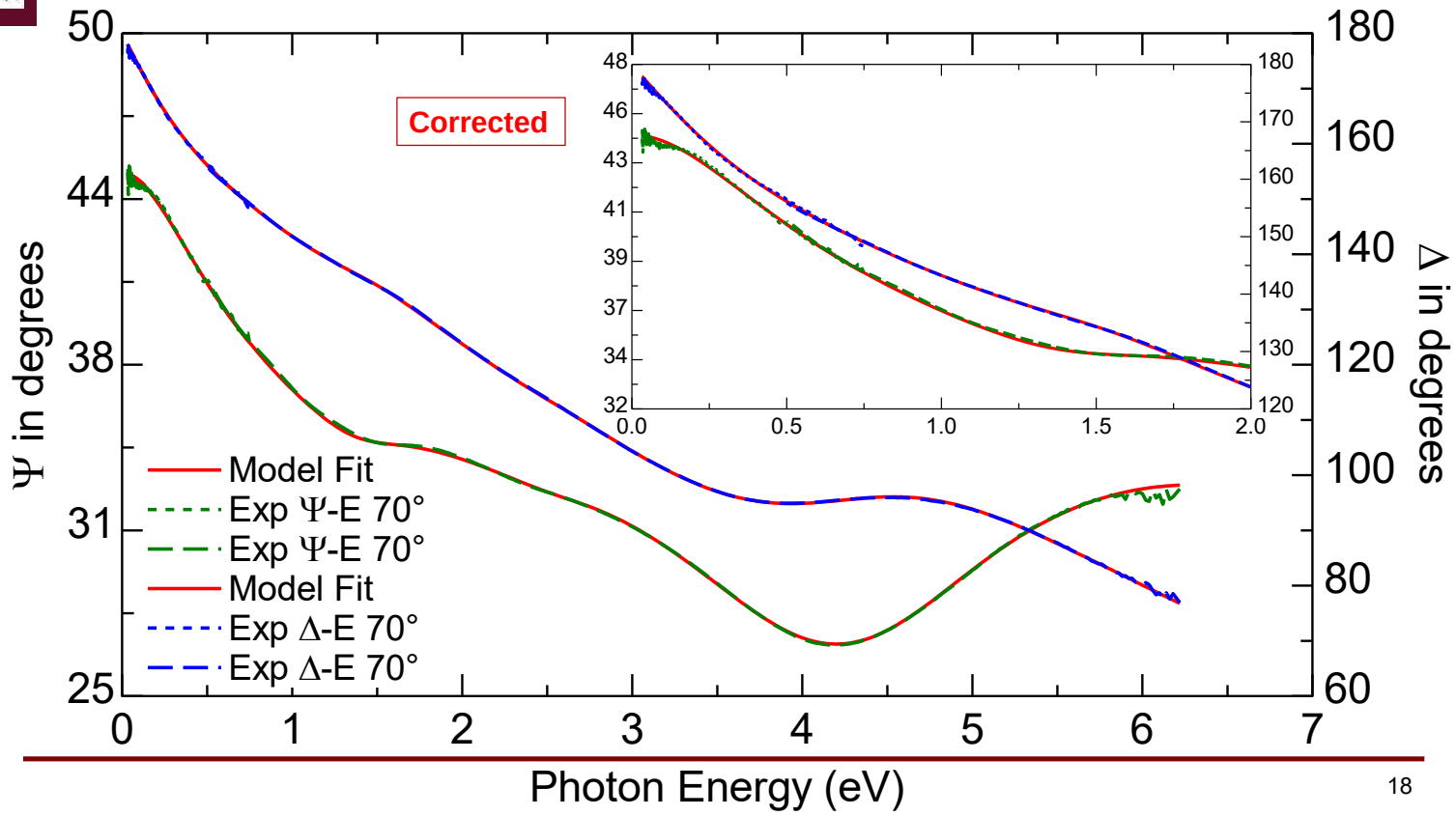

Change in the parameters of the model after the merge correction

MSE=1.309	Not corrected
Amp1.0	123.1±2.6
Amp2.0	22.682±0.0853
Amp3.0	0.98678±0.14
Amp4.0	0.14742±0.0917
Amp5.0	1.9925±0.0823
Amp6.0	1.8383±0.103
Br1.0	2.7201±0.0629
Br2.0	0.026659±0.000851
En3.0	1.5702±0.0166
En4.0	2.5683±0.0432
En5.0	4.7695±0.0062
En6.0	14.831±1.92
Br3.0	0.60284±0.0687
Br4.0	0.89705±0.306
Br5.0	2.2035±0.0428
Br6.0	10±4.45

MSE=0.8099	Corrected
Amp1.0	120.42±1.87
Amp2.0	22.064±0.0494
Amp3.0	1.7574±0.142
Amp4.0	0.14335±0.0578
Amp5.0	2.033±0.0532
Amp6.0	1.6434±0.0528
Br1.0	2.7545±0.045
Br2.0	0.017927±0.000506
En3.0	1.5206±0.0108
En4.0	2.6063±0.0271
En5.0	4.7697±0.00388
En6.0	11.964±0.524
Br3.0	0.82799±0.0491
Br4.0	0.89766±0.194
Br5.0	2.2206±0.0273
Br6.0	5.8563±1.14

Summary

- Using window effects parameters, FTIR-VASE experimental data are corrected so that they merge with VASE experimental data in the region of overlap.
- Two window effects parameters are sufficient to obtain a good window correction:
    1. constant out-of-plane retardance
    2. constant in-plane retardance,
- We do not fit the out-of-plane retardance of the entrance window, because this parameter does not influence the ellipsometric angles if the polarizer angle is 45 degrees (the usual choice for FTIR-VASE measurements).
- The model is finally fitted to the merged data.
- The model parameters change somewhat after the window correction, especially near the region of overlap between VASE and FTIR-VASE data.

REFERENCES

[1] K. H. J. Buschow and F. R. De Boer, *Physics of magnetism and magnetic materials* (Kluwer Academic/Pendulum Publishers, New York, 2003).

[2] C. Y. Ho, W. Powell, and P. E. Liley, J. Phys. Chem. Ref. Data, Supplement 3, **1**, 1 (1974).

[3] G. R. Stewart, J. Opt. Soc. Am. Rev. Sci. **54**, 1 (1983).

[4] A. P. Cracknell, *Magnetism in crystalline materials: applications of the theory of groups of cambiant symmetry*, (Elsevier, 2016).

[5] N. F. Mott, Proc. Phys. Soc. A **153**, 699 (1936).

[6] R. C. O'Handley, *Modern Magnetic Materials: principles and applications*, (Wiley, New York, 2000)

[7] N. V. Volkenshtein, V. P. Dyakona, and V. E. Startsev, Phys. Stat. Sol. (b) **57**, 9 (1973).

[8] S. Zollner, R. B. Gregory, M. Kottke, V. Vartanian, X. -D. Wang, D. Theodore, P. Fejes, J. Conner, M. Raymond, X. Zhu, et al. AIP **931** 337 (2007).

[9] V. Kamineni, M. Raymond, E. Bersch, B. Doris, and A. Diebold, J. Appl. Phys. **107** 093525 (2010).

[10] J. D. Jackson, *Classical electrodynamics* (John Wiley & Sons, New York, 2007).

[11] R. C. Jones, J. Opt. Sco. Am. **31** 488 (1941).

[12] H. G. Tompkins and E. A. Irene, *Handbook of Ellipsometry*, (William Andrew, Norwich, NY, 2005).

[13] J. A. Woollam Co., Inc., *Guide to Using WVASE32* (J. A. Woollam Co., Inc., Lincoln, NE, 2009).

[14] H. Fujiwara, *Spectroscopic ellipsometry: principles and applications* (John Wiley & Sons,West Sussex, England, 2007).

[15] R. M. A. Azzam and N. M. Bashara, *Ellipsometry on polarized light* (North Holand Publ. Co., Amsterdam, 1984).

[16] D. E. Aspnes, J. Vac. Sci. Technol. A **31**, 058502 (2013).

[17] E. Garcia-Caurel, A. De Martino, J.-P. Gaston, and L. Yan, Appl. Spectrosc. 67, 1 (2013).

[18] H. G. Tompkins and J. N. Hilfiker, *Spectroscopic Ellipsometry: Practical Application to Thin Film Characterization* (Momentum, New York, 2016).

[19] D. E. Aspnes, J. Opt. Soc. Am. **64**, 812 (1974).

[20] J. M. M. de Nijs, A. H. M. Holtslag, A. Hoeksta, and A. van Silfhout, J. Opt. Soc. Am. A **5**, 1466 (1988).

[21] R. W. Collins, Rev. Sci. Instrum. **61**, 2029 (1990).

[22] G. E. Jellison, F. A. Modine, and C. Chen, Proc. SPIE **3754**, Polarization: Measurement, Analysis, and Remote Sensing II, p. 150 (1999).

[23] B. Johs, Thin Solid Films **234**, 395 (1993).

[24] B. Johs, J. A. Woollam, C. M. Herzinger, J. Hilfiker, R. Synowicki, and C. L. Bungay, Proc. SPIE **10294**, Optical Metrology: A Critical Review, p. 10294-04 (1999).

[25] F. L. McCrackin, J. Opt. Soc. Am. **60**, 57 (1970).

[26] R. M. A. Azzam and N. M. Bashara, J. Opt. Soc. Am. **61**, 773 (1971).

[27] D. E. Aspnes, J. Opt. Soc. Am. **61**, 1077 (1971).

[28] J. M. M. de Nijs and A. van Silfhout, J. Opt. Soc. Am. A **5**, 773 (1988).

[29] R. M. A. Azzam and N. M. Bashara, J. Opt. Soc. Am. **64**, 1459 (1974).

[30] A. A. Studna, D. E. Aspnes, L. T. Flores, B. J. Wilkens, J. P. Harbison, and R. E. Ryan, J. Vac. Sci. Technol. A **7**, 3291 (1989).

[31] N. Solmeyer, K. Zhu, and D. S. Weiss, Rev. Sci. Instrum. **82**, 066105 (2011).

[32] G. E. Jellison, Jr., Appl. Opt. **38**, 4784 (1999).

[33] B. J. Stagg and T. T. Charalampopoulos, J. Phys. D: Appl. Phys. **26**, 2028 (1993).

[34] B. D. Johs and C. M. Herzinger, U. S. Patent No. 6,034,777 (7 March 2000).

[35] L. Jin and E. Kondoh, Opt. Lett. **39**, 1549 (2014).

[36] N. Nissim, S. Eliezer, L. Bakshi, D. Moreno, and L. Perelmutter, Opt. Commun. **282** , 3414 (2009).

[37] L. Jin, S. Kasuga, and E. Kondoh, Opt. Express **17**, 27811 (2014).

[38] T. Sasaki, Y. Tamegai, T. Ueno, M. Watanabe, L. Jin, and E. Kondoh, Jpn. J. Appl. Phys. **51**, 05EA02 (2012).

[39] M. Fox, Optical properties of solids (American Associations of Physics Teachers, 2002).

[40] M. Schubert, *Infrared ellipsometry on semiconductor layer structures: phonons, plasmons, and polaritons*, vol. 209 (Springer, Berelin, 2004).

[41] S. Zollner, P. P. Paradis, F. Abadizaman, and N. S. Samarasingha, J. Vac. Sci. Technol. B **37**, 012904 (2019).

[42] M. Cardona and P. Y. Yu, *Fundamentals of semiconductors* (Springer-Verlag, Berlin Heidelberg, 2005).

[43] D. W. Lynch and W. R. Hunter, in *Handbook of Optical Constants*, edited by E. D. Palik (Academic, San Diego, CA, 1985), vol. I, p. 313.

[44] M. A. Ordal, L. L. Long, R. J. Bell, S. E. Bell, R. R. Bell, R. W. Alexander, and C. A. Ward, Appl. Opt. **22**, 1099 (1983).

[45] S. Adachi, *The Handbook on Optical Constants of Metals* (World Scientific, Singapore, 2012), p. 334.

[46] L. Abdallah, T. M. Tawalbeh, I. V. Vasiliev, S. Zollner, C. Lavoie, A. Ozcan, and M. Raymond, AIP Advances **4**, 017101 (2014).

[47] L. S. Abdallah, Ph.D. thesis (New Mexico State University, Las Cruces, NM, USA, 2014).

[48] L. Jin, S. Kasuga, and E. Kondoh, Opt. Express **22**, 27811 (2014).

[49] M. Shiga and G. P. Pells, J. Phys. C. **2**, 1847 (1969).

[50] G. P. Pells, J. Sci. Instrum. **44**, 997 (1967).

[51] A, P. Lenham and D. M. Treherne, J. Opt. Soc. Am. **56**, 1076 (1966).

[52] A, P. Lenham and D. M. Treherne, J. Opt. Soc. Am. **57**, 476 (1967).

[53] D. W. Lynch, R. Rosei, and J. H. Weaver, Solid State Commun. **9**, 2195 (1971).

[54] P. B. Johnson and R. W. Christy, Phys. Rev. B **9**, 5056 (1974).

[55] MTI Corporation, 860 S. 19th Street, Richmond, CA, 94804, USA.

[56] S. Zollner, T. N. Nunley, D. P. Trujillo, L. G. Pineda, and L. S. Abdallah, Appl. Surf. Sci. **421**, 913 (2017).

[57] M. Losurdo, M. M. Giangregorio, O. Capezzuto, and G. Bruno, J. Phys. Chem. C **115**, 21804 (2011).

[58] D. H. Seib and W. E. Spicer, Phys. Rev. Lett. **20**, 1441 (1968).

[59] D. H. Seib and W. E. Spicer, Phys. Rev. B **2**, 1694 (1970).

[60] J. W. Allen and J. C. Mikkelsen, Phys. Rev. B **15**, 2952 (1977).

[61] A. J. Sievers, Phys. Rev. B **22**, 1600 (1980).

[62] P. E. Sulewski, A. J. Sievers, M. B. Maple, M. S. Torikachvili, J. L. Smith, and Z. Fisk, Phys. Rev. B **38**, 5338 (1988).

[63] B. C. Webb, A. J. Sievers, and T. Mihalisin, Phys. Rev. Lett. **57**, 1951 (1986).

[64] G. A. Thomas, J. Orenstein, D. H. Rapkine, M. Capizzi, A. J. Millis, R. N. Bhatt, L. F. Schneemeyer, and J. V. Waszczak, Phys. Rev. Lett. **61**, 1313 (1988).

[65] R. T. Collins, Z. Schlesinger, F. Holtzberg, P. Chaudhari, and C. Feild, Phys. Rev. B **39**, 6571 (1989).

[66] Z. Schlesinger, R. T. Collins, F. Holtzberg, C. Feild, S. H. Blanton, U. Welp, G. W. Crabtree, Y. Fang, and J. Z. Liu, Phys. Rev. Lett. **65**, 801 (1990).

[67] P. Kostic, Y. Okada, N. C. Collins, Z. Schlesinger, J. W. Reiner, L. Klein, A. Kapitulnik, T. H. Geballe, and M. R. Beasley, Phys. Rev. Lett. **81**, 2498 (1998).

[68] R. C. Vehse and E. T. Arakawa, Phys. Rev. **180**, 695 (1969).

[69] H. Ehrenreich, H. R. Philipp, and D. J. Olechna, Phys. Rev. **131**, 2469 (1963).

[70] C. S. Wang and J. Callaway, Phys. Rev. B **9**, 4897 (1974).

[71] C. S. Wang and J. Callaway, Phys. Rev. B **15**, 298 (1977).

[72] D. G. Laurent, J. Callaway, and C. S. Wang, Phys. Rev. B **20**, 1134 (1979).

[73] W. Hübner, Phys. Rev. B **42**, 11553 (1990).

[74] K. Doll, Surf. Sci. **544**, 103 (2003).

[75] E. Dietz, U. Gerhardt, and C. J. Maetz, Phys. Rev. Lett. **40**, 892 (1978).

[76] M.-P. Stoll, Solid State Commun. **8**, 1207 (1970).

[77] M.-P. Stoll, J. Appl. Phys. **42**, 1717 (1971).

[78] A. P. Lenham and D. M. Treherne, in *Optical Properties and Electronic Structure of Metals and Alloys*, edited by F. Abelés (North Holland, Amsterdam, 1966), pp. 196-201.

[79] R. E. Lindquist and A. W. Ewald, Phys. Rev. **135**, A191 (1964).

[80] P. B. Johnson and R. W. Christy, Phys. Rev. B **11**, 1315 (1975).

[81] I. I. Sasovskaya and M. M. Noskov, Fiz. Met. Metallov. **32**, 723 (1971).

[82] F. Abadizaman and S. Zollner, J. Vac. Sci. Technol. B **37**, 062920 (2019).

[83] N. F. Mott, Proc. R. Soc. Lond. A **167**, 580 (1938).

[84] J. C. Slater, Phys. Rev. **36**, 57 (1930).

[85] J. C. Slater, Phys. Rev. **49**, 537 (1936).

[86] A. H. Wilson, Proc. R. Soc. Lond. A **153**, 699 (1936).

[87] W. G. Baber, Proc. R. Soc. Lond. A **158**, 383 (1937).

[88] W. Nolting, W. Borgiel, V. Dose, and Th. Fauster, Phys. Rev. B **40**, 5015 (1989).

[89] W. Borgiel and W. Nolting, Z. Phys. B Condensed Matter **78**, 241 (1989).

[90] M. M. Kirillova, Yu. V. Knyavez, and Yu. I. Kuzmin, Thin Solid Films, 527 (1993)

[91] L. Viña, S. Logothetidis, and M. Cardona, Phys. Rev. B **30**, 1979 (1984).

[92] P. Friš, D. Munzar, O. Caha, and A. Dubroka, Phys. Rev. B **97**, 045137 (2018).

[93] S. Roberts, Phys. Rev. **114**, 104 (1959).

[94] M. -P. Stoll and C. Jung, J. Phys. Metal Phys., **9**, 2491 (1979).

[95] Y. Wang, Z. K. Liu, L. Q. Chen, Acta Mater. Metal Phys., **52**, (9) 2665 (2004).

[96] M. Gadenne and J. Lafait, J. Physique. **47**, 1405 (1986).

[97] H. Ibach and S. Lehwald, Solid State Commun. **45**, 633 (1983).

[98] H. M. Kirillova, Soviet Physics JEPT **34**, 178 (1972).

[99] B. Raquet, M. Viret, E. Sondergard, O. Cespedes, and R. Mamy Phys. Rev. B **66**, 024433 (2002).

[100] G. K. White and S. B. Woods, Phil. Trans. Roy. Soc. Lond A **251**, 273 (1959).

[101] T. Farrell and D. Greig, J. Phys. C (Proc. Phys. Soc.),ser. 2, **1**, 1359 (1968).

[102] D. A. Goodings, Phys. Rev. **132**, 542 (1963).

[103] B. Raquet, M. Viret, J. M. Broto, E. Sondergard, O. Cespedes, and R. Mamy J. Appl. Phys. **91**, 8129 (2002).

[104] I. A. Campbell, and A. Fert, Ferromagnetic Materials, Vol. 3., E. P. Wohlfarth, ed., North Holland, Amsterdam, 1982 p. 747

[105] T. Kasuya, Progr. Theor. Phys. (Kyoto) **16**, 58 (1956).

[106] M. J. Laubitz, T. Matsumura, and P. J. Kelly, Can. J. Phys. **54**, 92 (1976).

[107] S. V. Vonsovskii and Yu. A. Izyumov, Usp. Fiz. Nauk. **77**, 377 (1962).

[108] M. W. Stringfellow, J. Phys. C (PROC. PHYS. SOC.) ser. 2 **1**, 950 (1968).

[109] Q. Bian, S. K. Bose, and R. S. Shukla, J. Phys. Chem. Solids **69**, 168 (2008).

[110] E. D. Thompson and J. J. Myers, Phys. Rev. **153**, 574 (1967).

[111] G. Shirane, O. Steinsvoll, Y. J. Uemura, and J. Wicksted, J. Appl. Phys. **55**, 1887 (1984).

[112] S. Wakoh, J. Phys. Soc. Japan, **20**, 1894 (1965).

[113] D. E. Eastman, F. J. Himpsel, and J. A. Knapp, Phys. Rev. Lett. **40**, 1514 (1978).

[114] T. J. Kreutz, and T. Greber, Phys. Rev. B **58**, 1300 (1998).

[115] K. P. Kämper, W. Schmitt, and G. Güntherodt, Phys. Rev. B **42**, 10696 (1990).

[116] R. Raue and H. Hopster, Z. Phys. B - Condensed Matter **54**, 121 (1984).

[117] F. J. Himpsel, J. A. Knapp, and D. E. Eastman, Phys. Rev. B **19**, 2919 (1979).

[118] W. Borgiel, W. Nolting, and M. Donath, Solid State Commun. **72**, 825 (1989).

[119] M. -P. Stoll and C. Jung, J. Appl. Phys. **50**, 7477 (1979).

[120] T. Greber, T. J. Kreutz, and J. Osterwalder, Phys. Rev. Lett. **79**, 4465 (1997).